# Design and Realisation of InP and InAsP QDs Passively monolithic Mode-Locked Lasers

A thesis submitted in fulfilment of the partial requirement for the degree of Doctor of Philosophy

**by**

**Reem Alharbi**

School of Physics and Astronomy - Cardiff University

UK

January 2023

# Abstract

This thesis examines the feasibility of using Indium Phosphide and Indium Arsenide Phosphide Quantum Dots for passive mode-locking through modal gain and absorption under forward and reverse bias, a novel semi-empirical approach and experimental work on fabricated passively monolithic mode-locked lasers (MLLs).

There are two device configurations used in this work. The first device is a non-lasing segmented edge-emitting laser. The device's contact width is 50 μm, and its section length is 300 μm. This device is used to characterise the modal gain and modal absorption of two studied materials. The second set of devices are fabricated passively monolithic MLLs with a shallow ridge of 2 μm and total cavity length of 3 mm, gain-section length of 2400 μm and saturable absorber-section length of 600 μm. These second set of devices are used to measure and characterise the MLLs and to evaluate the reliability of the semi-empirical approach. Both devices are broad-area lasers with cleaved facets.

The characterisation of the reverse-biased saturable absorber-section using the segmented contact method demonstrated red-shift with the application of reverse bias between 0– 6 V with an absorption tuning wavelength range of 728 nm–735 nm and 773 nm–781.8 nm for Indium Phosphide and Indium Arsenide Phosphide Quantum Dots, respectively.

A novel semi-empirical approach has been established to simulate the conditions of mode-locking regimes; and accordingly, design the best-performing Indium Phosphide and Indium Arsenide Phosphide mode-locked lasers in terms of absorber-to-gain length ratio. The approach used the combination of modal gain under forward bias and modal absorption under reverse bias, with particular attention paid to absorber-to-gain length ratio. The ratios investigated are 1:4, 3:17, 1:9 and 1:19. This approach enabled the prediction that both materials with a total cavity length of 3 mm will not provide mode-locking regime or lasing when the ratio of the saturable absorber length exceeds 20%. However, InP QDs are predicted to produce ML regimes only for device designs

of 1:4, 3:17 and 1:9, while InAsP QDs are predicted to produce ML for device designs of 1:4, 3:17 ,1:9 and 1:19.

Mode-locking pulses were obtained from a fabricated Indium Phosphide Quantum Dot passively monolithic MLLs with absorber-to-gain length ratio of 1:4. Mode-locking pulse obtained with pulse width as short of 6 ps and repetition frequency of 12.5 GHz.

This work provides a valuable study of the performance of InP and InAsP self-assembled QDs passively monolithic MLLs operating in the 690 nm to 780 nm wavelength range, considering significant device performance parameters such as gain current density, saturable absorber reverse bias, absorber-to-gain length ratio and total cavity length.

# Acknowledgements

This has been a long journey with many ups and downs. However, I have been very grateful to have amazing support from the people around me.

First and foremost, I would like to express my sincere gratitude to my first supervisor, Prof Peter Smowton, for his patient guidance, encouragement, and invaluable advice. I also would like to thank my second supervisor, Dr Craig Allford, for his help and constructive discussions. Additionally, appreciation goes to my mentor, Prof Carole Tucker, for her kind words and support during the most challenging times.

I would like to thank all my colleagues at Cardiff University, especially the Cardiff CS Hub members, for their encouragement and support throughout my PhD. I extend my gratitude to Josie Travers-Nabialek and Richard Forrest for their kind assistance with the cleaving and bonding of monolithic mode-locked lasers in the cleanroom. Heartfelt thanks to all my colleagues.

I would like to acknowledge my sponsor in Saudi Arabia, King AbdulAziz University, for providing me with the opportunity to do this PhD. Special thanks go to the staff in the sponsorship administration and my physics department colleagues for providing me with the assistance I needed. Furthermore, I would like to thank the people in the Saudi Arabian Cultural Bureau in the UK for their help and guidance.

I also appreciate the support I received from my family and friends. I am indebted to my mom and dad for their prayers, unconditional support and care for my daughters. Thanks to my little princesses, Mariam and Ascia, for their patience and their never-ending love. I appreciate your encouragement to complete this journey; I am very proud of you. I am deeply grateful to my husband, Abdulaziz, for his patience and continued support. Finally, heartfelt thanks to all my sisters, brothers, friends.

# Publications and Conferences

## Papers

Z. Li, C. P. Allford, S. Shutts, A.F. Forrest, R. Alharbi, A. B. Krysa, M. Cataluna, P.M. Smowton (2020) ”*Monolithic InP Quantum Dot Mode-Locked Lasers Emitting at 730 nm” IEEE Photonics Technology Letters*, 32(17), 1073–1076. https://doi.org/10.1109/LPT.2020.3012568

## Conference proceedings

R. Alharbi, C. P. Allford, Z. Li, S. Shutts, A.B. Krysa, P.M. Smowton *“Performance Mapping of InP QDs Passively Monolithic Mode- Locked Laser “*, IEEE Xplore, **DOI:** 10.1109/IPC53466.2022.9975741, IPC, Canada, 2022.

## Conference presentations

Z. Li, S. Shutts, C. P. Allford, R. Alharbi, A.B. Krysa, P.M. Smowton “*InP Quantum Dot Mode-Locked Lasers emitting at 740 nm*”, SIOE, UK, 2018.

C.P. Allford, Z. Li, S. Shutts, A.F. Forrest, R. Alharbi, A. B. Krysa, M. Cataluna, P.M. Smowton “*InP Quantum Dot Monolithic Mode-Locked Lasers for Ultrashort Pulse Generation at 735 nm*”, ESLW, Ireland, 2019.

R. Alharbi, Z. Li, C. P. Allford, S. Shutts, A.B. Krysa, P.M. Smowton “*Design and realisation of InP Mode-locked Lasers Emitting in the 730nm Wavelength Range*”, Photonics West, USA, 2020.

**Table of Contents**

**ABSTRACT** ..... **II**

**ACKNOWLEDGEMENTS** ..... **IV**

**PUBLICATIONS AND CONFERENCES** ..... **V**

**LIST OF FIGURES** ..... **X**

**LIST OF TABLES** ..... **XVI**

**LIST OF ABBREVIATIONS** ..... **XVIII**

**CHAPTER 1 :** ..... **1**

**INTRODUCTION** ..... **1**

1.1 THESIS RATIONALE ..... 1

1.1.1 Quantum Dots (QDs) semiconductor materials in passive Mode-Locked Lasers (MLLs) ..... 1

1.1.2 Passively monolithic two-section QD Mode-Locked lasers (MLLs) ..... 5

1.1.3 Toward ultrashort pulses in the visible and near-infrared wavelength range ..... 6

1.2 THESIS STRUCTURE ..... 7

REFERENCES ..... 9

**CHAPTER 2 : BACKGROUND THEORY** ..... **13**

2.1 INTRODUCTION ..... 13

2.2 SEMICONDUCTOR LASER DIODES ..... 13

2.2.1 The laser structure ..... 13

2.2.2 The population inversion ..... 14

2.2.3 Fabry-Perot semiconductor laser ..... 15

2.2.3.3 Gain-current relation ..... 16

2.2.4 Quantum confinement: Density of states ..... 17

2.5 QUANTUM DOTS ..... 20

2.5. 1Advantages of QDs ..... 21

2.6 FUNDAMENTALS OF ML ..... 23

2.6.1 Longitudinal modes in a laser resonator ..... 23

2.6.2 Mode-locking ..... 25

2.6.3 Passive ML ..... 26

2.6.3 Time Bandwidth Product ..... 29

2.7 QUANTUM CONFINED STARK EFFECT ..... 29

2.8 DEVICE STRUCTURES ..... 31

2.8.1 Gain-guided geometry: Stripe lasers ..... 31
2.8.2 Index-guided geometry: Ridge lasers ..... 32
2.6 SUMMARY ..... 34
REFERENCES ..... 35

**CHAPTER 3: EPITAXIAL STRUCTURES, EXPERIMENTAL TECHNIQUES, AND EXPERIMENTAL SET-UP ..... 37**

3.1 INTRODUCTION ..... 37
3.2 EPITAXIAL STRUCTURES ..... 37
3.2 DEVICE FABRICATION AND SAMPLE PREPARATION MOUNTING ..... 39
3.3 EXPERIMENTAL TECHNIQUES AND EXPERIMENTAL SET-UP ..... 40
3.3.1 Overview of Segmented Contact Method ..... 40
3.3.2 Experimental-Setup of Segmented Contact Method ..... 44
3.3.2 Reverse Bias Measurement ..... 47
3.3.4 Near Field Measurement ..... 48
References ..... 51

**CHAPTER 4: ..... 52**

**MATERIALS CHARACTERISATION: INP AND INASP QD ..... 52**

4.1 INTRODUCTION ..... 52
4.2 MODAL ABSORPTION OF THE INP AND INASP MATERIALS ..... 53
4.3 INFLUENCES OF REVERSE BIAS ON MODAL ABSORPTION ..... 57
4.4 MODAL GAIN OF INP AND INASP QDS SEMICONDUCTOR MATERIALS ..... 62
4.5 GAIN- CURRENT RELATION ..... 70
4.5 CONCLUSION ..... 74
REFERENCES ..... 76

**CHAPTER 5: ..... 79**

**A NOVEL APPROACH FOR OPTIMISING INP QD MONOLITHIC PASSIVELY MONOLITHIC MLLS ..... 79**

5.1 INTRODUCTION ..... 79
5.2 BASIS OF SEMI-EMPIRICAL APPROACH ..... 80
5.3 CHARACTERISATION OF NET MLL MODAL GAIN ..... 81
5.4 GAIN-CURRENT DENSITY CHARACTERISTIC ..... 91
5.5 INFLUENCE OF REVERSE BIAS AND ABSORBER SECTION LENGTH ON THRESHOLD CURRENT DENSITY ..... 95
5.6 MAPPING OF THE OPERATIONAL BIAS CONDITIONS ..... 97

5.7 PEAK WAVELENGTH AND SPECTRAL FWHM OF PREDICTED ML PULSES ..... 100
5.8 MODE-LOCKING TRENDS ..... 105
5.8.1 Current density of gain-section ..... 105
5.8.2 Reverse bias of SA-section ..... 106
5.8.3 SA-section to gain-section length ratio ..... 107
5.9 CONCLUSION ..... 108
REFERENCES ..... 110

**CHAPTER 6: ..... 112**

**MAPPING THE PERFORMANCE OF INASP QD MONOLITHIC PASSIVELY MONOLITHIC MLLS ..... 112**

6.1 INTRODUCTION ..... 112
6.2 SEMI-EMPIRICAL APPROACH ..... 112
6.3 CHARACTERISATION OF NET MLL MODAL GAIN ..... 113
6.4 CHARACTERISTIC OF GAIN-CURRENT RELATION ..... 120
6.5 INFLUENCE OF REVERSE-BIAS AND SA-SECTION LENGTH ON THRESHOLD CURRENT DENSITY ..... 124
6.6 MAPPING OF THE OPERATIONAL BIAS CONDITIONS ..... 125
6.7 PEAK WAVELENGTH AND SPECTRAL FWHM OF PREDICTED ML PULSES ..... 128
6.8 MODE-LOCKING TRENDS ..... 132
6.8.1 Current density of the gain-section ..... 133
6.8.2 Reverse-bias voltage of SA-section ..... 134
6.8.3 SA to gain length ratios ..... 135
6.9 CONCLUSION ..... 136
REFERENCES ..... 138

**CHAPTER 7: ..... 140**

**INP QD PASSIVELY MONOLITHIC MLLS: EXPERIMENTAL RESULTS ..... 140**

7.1 INTRODUCTION ..... 140
7.2 EXPERIMENTAL RESULTS ..... 140
7.2.1 Light-Current (L-I) Performance ..... 140
7.2.2 Spectral and Temporal Performance ..... 142
7.2.3 Radio Frequency (RF) Measurements ..... 145
7.3 VALIDATION OF THE SEMI-EMPIRICAL APPROACH ..... 146
REFERENCES ..... 149

**CHAPTER 8: ..... 150**

**CONCLUSION AND FUTURE WORK ..... 150**

**8.1 SUMMARY ..... 150**

8.2 FUTURE WORK ..... 156

# List of Figures

Figure 1. 1:(Right) Ti-Sapphire Solid state lasers (image obtained online from Newport Corporation & Wikipedia websites), (left) semiconductor laser chip…….. ...2
Figure 1. 2:The normalised modal gain profile as a function of carrier density for bulk, QW and QD material systems (Mee et al., 2014)……..3
Figure 1. 3: In-vivo near-infrared (NIR) fluorescence imaging (image obtained from drugtargetview website)……6
Figure 2.1: Schematic diagram of separate confinement heterostructure (SCH)….. 14
Figure 2. 2: Fabry Perot laser…….....16
Figure 2. 3: the electrons and holes DOS for: (a) bulk materials and quantum well (QW); (b) Quantum wire; (c) Quantum dot (QD)(Smowton 2012)…….. 18
Figure 2. 4: The figure at the right represents the morphology of QDs, and at the left displays the DOS for carriers in (a) an ideal quantum-dot system; (b) an actual quantum-dot system illustrating the effects of inhomogeneous broadening on the DOS(Rafailov and Avrutin 2013)……. 21
Figure 2. 5: the profiles of (a) the gain spectrum; (b) the longitudinal modes; (c) the lasing output……...24
Figure 2. 6: Schematic diagram of the design of passive mode-locked laser…… 26
Figure 2. 7: Dynamics of loss and gain for the generation of short pulses……27
Figure 2. 8: The gain and absorption as a function of carrier density illustrating the differential gain, loss and the transparency point…….. 28
Figure 2. 9: Spectral pulse versus temporal pulse……. 29
Figure 2. 10: The influence of applied EF on the QW: (a) No EF is applied;……...30
Figure 2. 11: Schematic diagram of the cross-section of stripe laser illustrating the current spreading……32
Figure 2. 12: Schematic diagram of the cross-section of ridge laser……33
Figure 3. 1: Schematic of the structure layers of both QDs material InP and InAsP……. 38
Figure 3. 2: TEM images of the active region of InAsP dots (upper) and InP dots (lower). ..... 39

Figure 3. 3: Schematic of the ridge passively monolithic MLL and an optical microscope image of ridge laser with 2µm width. ..... 40
Figure 3. 4: The design of the segmented contact oxide Laser structure. ..... 41
Figure 3. 5: ASE of pumped Segments 1 and 2, individually and together. ..... 43
Figure 3. 6: The gain and absorption of InAsP QDs at current 152mA. ..... 44
Figure 3. 7: Schematic Diagram of Experimental setup for measuring ASE from segmented contact non-lasing edge emitting device. ..... 45
Figure 3. 8: The IV characteristics of InP QD material of Segments 1 and 2. ..... 47
Figure 3. 9: The Near Field of InAsP QD multi-section device. ..... 47
Figure 3. 10: An example of absorption of InP QD material under the influence various reverse bias and constant driven current of 100 mA. ..... 48
Figure 3. 11: the optical image of the Nearfield and the intensity profile of InAsP QD multi-section device at current pump rate 152 mA. ..... 49
Figure 4. 1: the positive modal absorption of InP QDs (red) and InAsP QDs (blue)…….. 53
Figure 4. 2: Gaussian fit of GS-small dot 1 and GS-small dot 2 of InAsP QDs positive modal absorption. ..... 55
Figure 4. 3: Gaussian fit of GS-large dot, GS-small dot and ES-large dot of InP QDs positive modal absorption. ..... 56
Figure 4. 4: Influence of applied reverse bias on the absorption spectrum of InP QDs when the gain section is pumped with fixed gain current. ..... 59
Figure 4. 5: Influence of applied reverse bias on the absorption spectrum of InAsP QDs when the gain section is pumped with fixed gain-section current. ..... 59
Figure 4. 6: the redshifts of peak absorption wavelength at different reverse bias conditions of InP QDs (top) and InAsP QDs (bottom). ..... 61
Figure 4. 7: the modal gain of InP QDs materials as a function of current density… 63
Figure 4. 8: The modal gain of InAsP QDs materials at different pumping rate. ..... 63
Figure 4. 9: the blue shift of InP (upper) InAsP (lower) QDs materials as a function of current density. ..... 65
Figure 4. 10: comparison of FWHM of InP QDs (blue) InAsP QDs (black) materials at the same injected current 100 mA. ..... 66
Figure 4. 11: the gain amplitude and FWHM of InP (upper) InAsP (lower) QDs materials as a function of current density. ..... 68

Figure 4. 12: gain-current relation of InAsP QDs. ..... 71
Figure 4. 13: gain-current relation of InP QDs. ..... 71
Figure 4. 14: gain current relation of InP and InAsP QDs indicates the differential gain and loss. ..... 73
Figure 5. 1 : Net MLL gain versus wavelengths for all investigated absorber to gain length ratios at fixed gain current density 1803 A.cm$^{-2}$ and fixed reverse bias of absorber section 1 V……...81
Figure 5. 2 : The net MLL modal gain of a device design (1:19) at various fixed reverse bias (1 V, top left –6 V, bottom right). ..... 85
Figure 5. 3 : The net MLL modal gain of a device design (1:9) at various fixed reverse bias (1 V, top left –6 V, bottom right). ..... 86
Figure 5. 4 : The net MLL modal gain of a device design (3:17) at various fixed reverse bias (1 V, top left –6 V, bottom right). ..... 87
Figure 5. 5 : The net MLL modal gain of a device design (1:4) at various fixed reverse bias (1 V, top left –6 V, bottom right). ..... 88
Figure 5. 6 : The net MLL modal gain of a device design (1:3) at various fixed reverse bias (1 V, top left –6 V, bottom right). ..... 89
Figure 5. 7 : The net MLL modal gain of a device design (1:9) at specific driving conditions when double pulse regime (GS and ES) is generated. ..... 91
Figure 5. 8 : the gain-current curve of device design (1:19) and for various reverse bias conditions (1 V–6 V). ..... 93
Figure 5. 9 : The gain-current curve of device design (1:9) and for various reverse bias conditions (1 V–6 V). ..... 93
Figure 5. 10 : the gain-current curve of device design (3:17) and for various reverse bias conditions (1 V–6 V). ..... 94
Figure 5. 11 : the gain-current curve of device design (1:4) and for various reverse bias conditions (1 V–6 V). ..... 94
Figure 5. 12 : The threshold current density as a function of SA length for various reverse bias conditions (1 V–6 V). ..... 96
Figure 5. 13 : The threshold current density as a function of reverse biases for all investigated device length ratios designs. ..... 97
Figure 5. 14 : The ML operational maps of biases conditions for all the device length ratio designs. ..... 99

Figure 5. 15 : The peak wavelength and spectral FWHM of the predicted ML regimes for device length ratio design (1:4) as a function of operating biases conditions (The white area denotes no ML regime region). ..... 101
Figure 5. 16 : The peak wavelength and spectral FWHM of the predicted ML regimes for device length ratio design (3:17) as a function of operating biases conditions (The white area denotes no ML regime region). ..... 102
Figure 5. 17 : The peak wavelength and spectral FWHM of the predicted ML regimes at GS operation for device length ratio design (1:9) as a function of operating biases conditions (The white area denotes no ML regime region). ..... 103
Figure 5. 18 : The peak wavelength and spectral FWHM of the predicted ML regimes at ES operation for device length ratio design (1:9) as a function of operating biases conditions (The white area denotes no ML regime region). ..... 104
Figure 5. 19 : The peak wavelength and the spectral FWHM versus the gain current density for device length ratio (1:4) and at fixed reverse bias 2 V. ..... 106
Figure 5. 20 : The peak wavelength and the spectral FWHM versus the reverse bias for device length ratio (1:4) and at fixed gain current density 1803 A.cm$^{-2}$..... 107
Figure 5. 21 : The peak wavelength and the FWHM versus the reverse bias for the highest gain current density produced ML pulse and at fixed gain reverse bias 4 V. ..... 108
Figure 6. 1: Net MLL gain as a function of wavelengths for all investigated SA to gain length ratios at fixed gain-section current density 1667 A.cm$^{-2}$ and fixed reverse bias of absorber section 3 V…….. ……...113
Figure 6. 2: The net MLL modal gain of a device design with SA to gain length ratio of (1:19) at various fixed reverse bias (1 V, top left–6 V, bottom right)..... 116
Figure 6. 3: The net MLL modal gain of a device design with SA to gain length ratio of (1: 9) at various fixed reverse bias (1 V, top left–6 V, bottom right)..... 117
Figure 6. 4: The net MLL modal gain of a device design with SA to gain length ratio of (3:17) at various fixed reverse bias (1 V, top left–6 V, bottom right)..... 118
Figure 6. 5: The net MLL modal gain of a device design with SA to gain length ratio of (1:4) at various fixed reverse bias (1 V, top left–6 V, bottom right)..... 119
Figure 6. 6: the gain-current curve of device design (1:19) and for various reverse bias conditions (1 V–6 V)..... 121

Figure 6. 7: the gain-current curve of device design (1:9) and for various reverse bias conditions (1 V–6 V)..... 121
Figure 6. 8: the gain-current curve of device design (3:17) and for various reverse bias conditions (1 V–6 V)..... 122
Figure 6. 9: the gain-current curve of device design (1:4) and for various reverse bias conditions (1 V–6 V)..... 122
Figure 6. 10: The threshold current density as a function of SA-section length for various reverse bias conditions (1 V– 6 V)..... 124
Figure 6. 11: The threshold current density as a function of reverse-biases for all investigated device length ratios designs..... 125
Figure 6. 12: The ML operational maps of biases conditions for all the device length ratio designs: 1:9 and 1:19 (upper), 3:17 (middle) and 1:4 (bottom)..... 127
Figure 6. 13: The peak wavelength and spectral FWHM of the predicted ML regimes for device length ratio design (1:19) as a function of operating biases conditions (The white area denotes no ML regime region)..... 129
Figure 6. 14: The peak wavelength and spectral FWHM of the predicted ML regimes for device length ratio design (1:9) as a function of operating biases conditions (The white area denotes no ML regime region)..... 130
Figure 6. 15: The peak wavelength and spectral FWHM of the predicted ML regimes for device length ratio design (3:17) as a function of operating biases conditions (The white area denotes no ML regime region)..... 131
Figure 6. 16: The peak wavelength and spectral FWHM of the predicted ML regimes for device length ratio design (1:4) as a function of operating biases conditions (The white area denotes no ML regime region)..... 132
Figure 6. 17: The peak wavelength and the spectral FWHM versus the gain-section current density for device length ratio 3:17 and at fixed reverse bias 6 V..... 133
Figure 6. 18: The peak wavelength and the spectral FWHM versus the reverse bias of SA-section for device length ratio 1:4 and at fixed gain-section current density 1190 $A.cm^{-2}$..... 134
Figure 6. 19: The peak wavelength and the FWHM versus the SA-section to gain-section length ratios of SA-section at gain-section current density of 857 $A.cm^{-2}$ and at fixed gain reverse bias 2 V..... 135

Figure 7. 1: The L-I characteristics of device design of absorber to gain length ratio (1:4) for different bias conditions: forward, floating, and reverse-bias (1 V-3 V). ……..141

Figure 7. 2: Pulse width and optical spectrum at a fixed reverse bias (1.85 V) measured at a gain current of 75 mA, 80 mA, and 85 mA. ..... 143

Figure 7. 3: The predicted net MLL gain of the device with length ratio (1:4) at gain current 75mA, 80mA, and 85mA and fixed reverse-bias 1.85V. ..... 144

Figure 7. 4: Comparison of the experimental and predicted performance..... 144

Figure 7. 5: RF spectra as a function of intensity in dBm demonstrate the repetition frequency of four MLLs with different total cavity length (a) 2 mm, (b) 2.5 mm, (c) 3mm and (d) 3.5 mm.. ..... 146

# List of Tables

Table 2. 1: Advantages and Disadvantages of stripe lasers. ..... 32
Table 2. 2: Advantages and Disadvantages of ridge lasers. ..... 33
Table 4. 1: A list of parameters that were used to fit the Gaussian distributions of InAsP QDs..……..…….57
Table 4. 2: a list of parameters that were used to fit the Gaussian distributions of InP QDs. ..... 57
Table 4. 3: Extracted threshold current density from the gain measurement for different cavity lengths of InP and InAsP QDs. ..... 72
Table 5. 1: Blue-shift and red-shift wavelength ranges for the studied absorber to gain length ratios of 3mm cavity length. The blue-shift resulted from increasing the gain carrier density at fixed reverse-bias of 1V whereas the red-shift resulted from increasing the revers-bias at fixed gain current density of 1803 A.cm$^{-2}$…….... 83
Table 5. 2: Threshold current density for all studied absorber to gain length ratios and at fixed reverse bias ranged between (1 V–6 V). ..... 95
Table 6. 1: Blueshift and redshift wavelength ranges for the studied absorber to gain length ratios at fixed 1 V (blue-shift) and fixed gain-section current density of 857A.cm-2 (red-shift)……...115
Table 6. 2: Threshold current density for all studied absorber to gain length ratios and at fixed reverse bias ranged between (1 V– 6 V) – all have 3mm total device length. ..... 123
Table 8. 1: The performance of all current QDs passively MLLs ……...……155

# List of Abbreviations

| | |
|---|---|
| **QDs** | **Quantum Dots** |
| **MLLs** | Mode-Locked Lasers |
| **ML** | Mode-locking |
| **TBP** | Time Bandwidth Product |
| **InP** | Indium Phosphide |
| **InAsP** | Indium arsenide Phosphide |
| **QWELL** | Quantum Dot in a Well system |
| **FWHM** | Full-Width at a Half Maximum |
| **SCH** | Separate Confinement Heterostructure |
| **SCM** | Segmented Contact Method |
| **NF** | Near-field |
| **QCSE** | Quantum Confined Stark Effect |
| **ASE** | Amplified Spontaneous Emission |

# Chapter 1 :

# Introduction

## 1.1 Thesis rationale

### 1.1.1 Quantum Dots (QDs) semiconductor materials in passive Mode-Locked Lasers (MLLs)

In the endeavour to generate ultrashort optical pulses, Ti:sapphire in the solid-state as a lasing medium has been the focus of research for ages, owing to its property of a broad spectral gain bandwidth. However, this laser is bulky, expensive, complex, and it requires a large amount of power to operate. Therefore, a compact and cheap alternative, such as semiconductor laser diode devices, have been the focus of significant research over the last three decades.

Fibre pulsed lasers are also a commonly used to generate ultrashort pulses in the range of femtosecond to nanosecond with ultimate high peak power. The gain medium of these pulsed lasers is doped optical fibre. The shortest pulse has been achieved from a passively mode-locked Fibre pulsed laser was 260 fs using Er-doped fibre laser (Nishizawa 2014).

The first demonstration of Mode-Locking (ML) in a semiconductor laser diode used a bulk active material system with ML pulses as short as 0.65 ps (van der Ziel et al. 1981). Shortly after, ML pulses of 1.6 ps were obtained from a semiconductor laser diode using the Quantum Well (QW) active material system (Silberberg et al. 1984), Recently, passively monolithic Mode-locked semiconductor lasers (MLLs) with cavity regions based on Quantum Dot (QD) structures are seen as potential ultrafast laser sources and a viable alternative to Ti-sapphire solid-state lasers for various applications. Pulse durations in the range of picoseconds and by improving the performance extended to the femtosecond range from 17 ps to 780 fs have been

achieved straight from the QD material (Huang et al., 2001; Nikitichev et al., 2011; Rosales et al., 2011; Thompson et al., 2009). This is due to outstanding properties, including spectrally broad optical gain and absorption due to the fluctuation of dots' sizes, ultrafast dynamics of both absorption and gain, high efficiency, low cost and compact size. These properties can be exploited in QD MLLs to generate ultrashort pulses in the picosecond or femtosecond range. In addition, QD materials can be operated at a low power consumption due to their low threshold current density, and as a consequence there is typically no requirement for water cooling. Moreover, these QD materials have high resilience to temperature variations, which is an excellent property for the stability of ML operation; they are promising as a temperature-insensitive pulsed source (Mee et al. 2012).

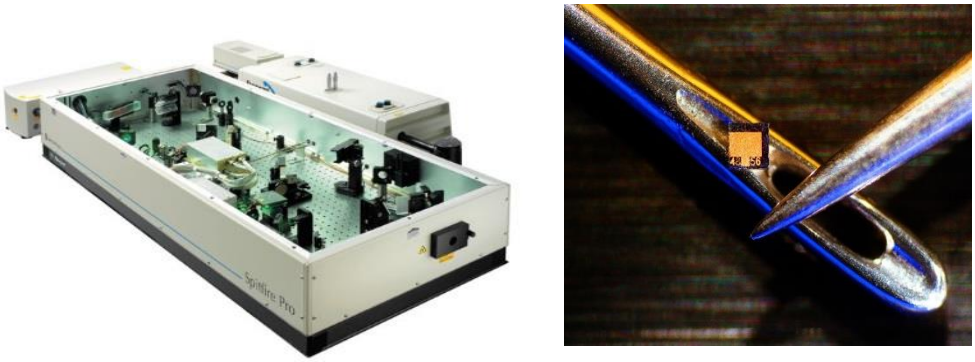

**Figure 1. 1: (left) Ti: Sapphire lasers (image obtained online from Newport Corporation & Wikipedia websites), (Right) semiconductor laser chip.**

The gain characteristics of QD materials are among their most advantageous physical properties for ultrafast applications. Figure 1.2 illustrates the normalised modal gain for different semiconductor media. The QW materials, compared to their bulk counterparts, exabit significant improvement to the mode-locking behaviour and this might be attributed to the step-like density of states (DOS) function (Derickson et al. 1992). In comparison to their QW and bulk counterparts, the modal gain in QD material systems tends to saturate abruptly with increasing carrier density(Mee et al., 2014; Thompson et al., 2009). This feature mostly originates from the delta-like DOS function of QDs and the decreased active region volume (Bimberg et al. 1997). This feature is essential to a stable ML behaviour due to its effect on several mode-locking performance parameters, such as pulse duration, chirp, and output power.

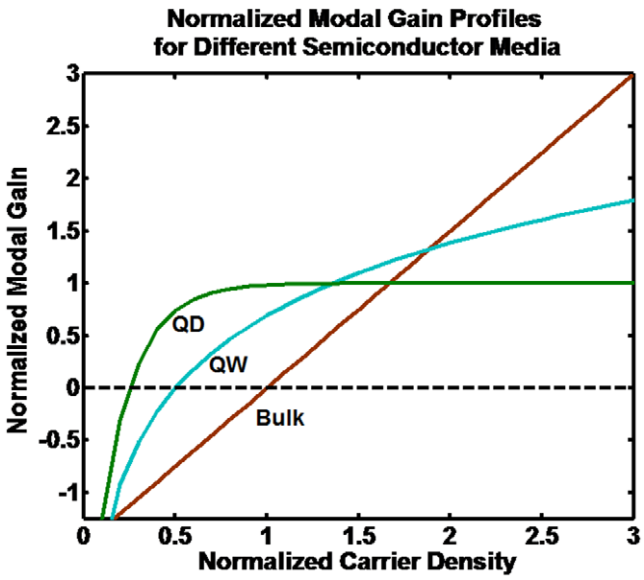


**Figure 1. 2:The normalised modal gain profile as a function of carrier density for bulk, QW and QD material systems (Mee et al., 2014).**

Stable passive mode-locking in two-section laser diodes is accomplished by maintaining a proper balance between the pulse-broadening and pulse-shortening processes inside the device. Pulse-shortening is caused by saturable absorption in the reverse-biased absorber-section, whereas pulse-broadening is mostly attributable to saturable gain in the forward-biased gain-section (Thompson et al. 2009). Equations 1.1 and 1.2 govern the extent of the pulse-broadening and the pulse-shortening, which represents the saturation energy of gain and absorption (Peter Vasil'ev 1995). The saturation energy indicates the quantity of energy needed to saturate the absorption or gain. In passively monolithic MLLs, the saturation energy of the absorber must be less than the saturation energy of the gain. In order to accomplish this, the loss must saturate faster than the gain and it must be greater than the gain everywhere except near to the pulses' peak.

$$E_{sat,G} = \frac{\hbar\omega A}{\Gamma\, dg/dn} \qquad (1.1)$$

$$E_{sat,A} = \frac{\hbar\omega A}{\Gamma\, da/dn} \qquad (1.2)$$

Where $\hbar\omega$ is the photon energy, A is the modal cross-sectional area, Γ is the confinement factor, (*dg/dn*) is the differential gain as a function of carrier density and (*da/dn*) is the differential loss as a function of carrier density.

A saturable absorber (SA) is an optical component, which can be integrated on the same wafer in case of passively monolithic MLLs. The absorption of a SA decreases as the incident optical intensity increases. When the incident intensity rises, the absorption saturates, loss reduces, and transmittance rises. This dynamic leads to the pulse shortening by the suppression of low-intensity signal and the generation of short intense optical pulses.

A device's mode-locking stability is determined by the S-factor, which plays a critical role in the pulse shaping performance. It can be defined as a ratio of the differential loss to the differential gain (Edik U. Rafailov 2011). Stable mode-locking requires that the S-factor to be greater than one (s>1), hence a high contrast in absorption saturation energy and gain saturation energy is desired (Mee et al., 2014). As can be seen from Figure 1.2, the (*da/dn*) for QD and QW material systems exhibits greater values below the threshold level (G = 0) than the (*dg/dn*) values above this threshold line ($da/dn > dg/dn$). This impact is more prominent in QWs than in bulk materials, owing to the step-like DOS function, and it is much more pronounced in QDs due to the discrete nature of DOS function. Due to the finite carrier density of available states, the rate of change in gain with carrier density (dg/dn) decreases as carrier density grows for semiconductors in general; hence, the differential gain in the absorption regime is greater than in the gain regime. Accordingly, it has resulted in low absorption saturation energy and high gain saturation energy. The modal gain profile of QDs has the highest contrast in absorption saturation energy to the gain saturation energy, compared to the QW and bulk as in Figure 1.2. Additionally, QDs material exhibit the lower threshold current density among their QW and the bulk counterparts (see Figure 1.2). This aids the QD materials to obtain a wider stability map than in the QW system.

### 1.1.2 Passively monolithic two-section QD Mode-Locked lasers

The first revealed passively monolithic QD MLLs consisted of InAs/ $In_{0.2}Ga_{0.8}As$ QDs grown on GaAs substrate. The wavelength of their ML pulses was in the range of 1.3μm with a pulse width of 17 ps (Huang et al. 2001). This wavelength range has been extended to 1.55μm when InAs/ $In_{0.2}Ga_{0.8}As$ QDs is grown on an InP substrate (Rosales et al. 2011). When these QD materials (InAs/ $In_{0.2}Ga_{0.8}As$) are grown on Si, ML pulses of wavelength in the O-band range (1260nm-1360nm) have been generated with pulse width of 1.3ps (Liu et al. 2018).

The second QD materials that were used in passive monolithic MLLs were InGaAs/InAs, which is grown on GaAs, which covers the wavelength range 1.1–1.3μm with the narrowest pulse width of 780 fs (Thompson et al. 2006). The same QD material, but grown on an InP substrate has provided longer wavelength range in the 1.4–1.9μm (Rafailov et al. 2004).

QD materials have provided better ML performance compared to their QW system. For instance, the shortest pulse width obtained from InGaAs QD was 780fs (Thompson et al. 2006a), whereas the shortest pulse width obtained from InGaAs QW was 1.1ps (Qiao et al. 2022). Additionally, QD structures demonstrate ultrafast absorption and gain recovery (Rafailov et al. 2007). For example, recovery durations for absorption varied from 62 ps to 700 fs has been demonstrated directly in a QD absorption modulator by applying a reverse bias from 0 V to 10 V (Malins et al. 2006).

There are different attempts in the literature to improve the performance of passive two-section MLLs by changing factors, including the device structures, the device contact geometry and absorber-to-gain length ratios. However, it has been found that the ML behaviours are the most sensitive to absorber-to-gain length ratios. So, this parameter was the scope of many studies in the last decade. Some studies were conducted by using fabricated practical MLL devices (Thompson et al. 2009), and some studies were concentrated in predicting the performance of MLL using analytical model(Radziunas et al. 2011; Mee et al. 2014).

### 1.1.3 Toward ultrashort pulses in the visible and near-infrared wavelength range

The previous work on passive monolithic QD MLLs has focused on wavelengths in the range of 1.1–1.9μm for telecommunication applications. However, the achievement of ML pulses from QD materials with shorter wavelength in the range of visible to near-infrared (680 nm- 1000 nm) and with power exceeding 1 W has the potential for in-vivo applications particularly, for two-photon fluorescence microscopy (Figure 1.3). Ti-Sapphire lasers at wavelength (750 nm) were used for two-photon fluorescence microscopy as a better alternative to the traditional confocal microscopy in term of spatial and temporal resolution (Soeller and Cannell 1996).

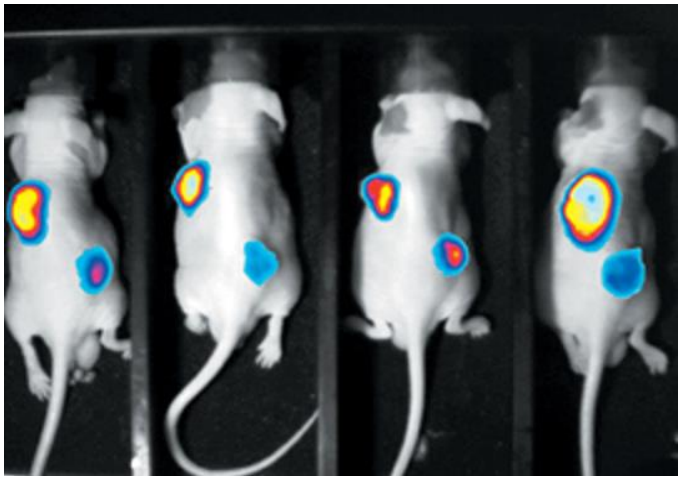

**Figure 1. 3: In-vivo near-infrared (NIR) fluorescence imaging (image obtained from drugtargetview website).**

InP QDs grown on GaAs with a wavelength range 690nm–730nm are useful materials and can be used as different laser sources, such as tuneable lasers or multi-wavelength sources (S. Shutts, 2012; Shutts et al., 2013; Smowton et al., 2005). This wavelength range was extended to a longer wavelength (690nm–780nm) by adding As to the InP QD layer to form a new QD material InAsP (I. Karomi 2015; Krysa et al. 2016). Additionally, the gain and absorption recovery dynamics for electrically pumped InP QDs has been investigated by (Langbein et al. 2010) using a pump-probe technique and showing fast recovery performance in the range of 200 fs.

InP and InAsP QD semiconductor lasers with a broad optical gain in this range of wavelengths from 690nm to 780nm are promising, and they aim to achieve ultrashort pulse generation with pulse durations in the picosecond and sub-picosecond range. Therefore, these QD semiconductor MLLs have the potential to replace the Ti-Sapphire solid-state and at this range of wavelengths (690nm–780nm) for two-photon fluorescence microscopy, particularly three-dimensional imaging of cells and tissues. This visible to infrared wavelengths provide high penetration into the tissue, and ultrashort pulses in the picosecond range could maximise the efficiency of imaging (Piston 1999). The compactness feature will ease to the use of these materials for lab-on-chip devices.

The main purpose of this PhD thesis is to evaluate the feasibility of using InP and InAsP QDs materials for mode-locking operation, particularly for passive monolithic MLLs. This can be accomplished by a comprehensive investigation of the modal gain and modal absorption under forward and reverse bias conditions by utilising the Segmented Contact Method (SCM) (Blood et al. 2003). Additionally, the performance of those QD materials as passive monolithic MLLs could be investigated by a novel semi-empirical approach based on modal gain and modal absorption measurements with particular attention paid to the design of the absorber-section and gain-section lengths. This approach aims for further understanding of the performance of InP and InAsP QD passive monolithic MLLs.

## 1.2 Thesis structure

The thesis is structured as follows:

**Chapter 1** provides a brief literature review about the passive monolithic two-section QD MLLs and the significance of the absorber-to-gain length ratios. Additionally, the chapter introduces the motivation of this work.

**Chapter 2** describes the background theories related to this work, including the basics of semiconductor laser diodes, the fundamental advantages of QD materials, the fundamentals of Mode-Locking (ML) with in-depth description of passive ML and the

theory of Quantum Confined Stark Effect (QCSE). In addition, brief comparison between gain-guided and index-guided device geometry is provided.

**Chapter 3** illustrates the epitaxial structures of both studied QD materials InP and InAsP. An overview of the main experimental technique used in this work, known as SCM, is provided. Additionally, an experimental setup of the measurements that are made in this thesis, such as SCM, near-field measurements and the light-current characteristic measurements (LI).

**Chapter 4** focuses on investigating the ML stability condition of the two studied QD materials (InP and InAsP). It shows the measurements of the modal gain under different pumping levels, the modal absorption for various reverse-bias voltage, gain-current characteristics, and detailed analysis of the gain and absorption, including the peak gain amplitude and wavelength. Regarding the condition of ML, we answered the question of the availability of achieving ML pulses from those studied two materials.

**Chapter 5** establishes a novel, semi-empirical approach to investigating the performance of InP passively monolithic MLLs and designing the best performing device. This includes the characterisation of net MLL modal gain, gain-current, the influence of the reverse bias on threshold current density, the impact of absorber-to-gain length ratio on the threshold current density, the operational map of InP MLL as a function of gain-current and absorber-voltage, in addition to the wavelength and the corresponding spectral width. The ML trends are also explored.

**Chapter 6** investigates the performance of InAsP passively monolithic MLLs using the same approach as the previous chapter, and it finds the best performing device in term of absorber-to-gain length ratios.

**Chapter 7** focuses on the measurements of practical designed InP QD passive monolithic MLL devices. Comparison between the predicted and measured performances is provided, in addition to the limitation of the shallow ridge MLLs.

**Chapter 8** summarises the findings obtained from this work and highlight future works.

## References

Bimberg, D., Kirstaedter, N., Ledentsov, N.N., Alferov, Z.I., Kop'ev, P.S. and Ustinov, V.M. 1997. *InGaAs-GaAs Quantum-Dot Lasers*.

Blood, P., Lewis, G.M., Smowton, P.M., Summers, H., Thomson, J. and Lutti, J. 2003. Characterization of Semiconductor Laser Gain Media by the Segmented Contact Method. In: *IEEE Journal on Selected Topics in Quantum Electronics*., pp. 1275–1282. doi: 10.1109/JSTQE.2003.819472.

Derickson, D.J., Helkey, R.J., Mar, A., Karin, J.R., Wasserbauer, J.G. and Bowers, J.E. 1992. Short Pulse Generation Using Multisegment Mode-Locked Semiconductor Lasers. *IEEE Journal of Quantum Electronics* 28(10), pp. 2186–2202. doi: 10.1109/3.159527.

Edik U. Rafailov, Maria Ana Cataluna and Eugene A. Avrutin 2011. *Ultrafast Lasers Based on Quantum dot Structure:Physics and Devices*. first edition. Rafailov. Edik, Cataluna. M. Avrutin. E. ed. Germany: WIELY-VCH.

Huang, X., Stintz, A., Li, H., Lester, L.F., Cheng, J. and Malloy, K.J. 2001. Passive mode-locking in 1.3 μm two-section InAs quantum dot lasers. *Applied Physics Letters* 78(19), pp. 2825–2827. doi: 10.1063/1.1371244.

Karomi, I., Smowton, P.M., Shutts, S., Krysa, A.B. and Beanland, R. 2015. InAsP quantum dot lasers grown by MOVPE. *Optics Express* 23(21), pp. 27282–27291.

Krysa, A.B., Roberts, J.S., Devenson, J., Beanland, R., Karomi, I., Shutts, S. and Smowton, P.M. 2016. Growth and characterisation of InAsP/AlGaInP QD laser structures. In: *2016 Compound Semiconductor Week, CSW 2016 - Includes 28th International Conference on Indium Phosphide and Related Materials, IPRM and 43rd International Symposium on Compound Semiconductors, ISCS 2016*. Institute of Electrical and Electronics Engineers Inc. doi: 10.1109/ICIPRM.2016.7528566.

Langbein, W., Cesari, V., Masia, F., Krysa, A.B., Borri, P. and Smowton, P.M. 2010. Ultrafast gain dynamics in InP quantum-dot optical amplifiers. *Applied Physics Letters* 97(21). doi: 10.1063/1.3518715.

Liu, S., Norman, J.C., Jung, D., Kennedy, M.J., Gossard, A.C. and Bowers, J.E. 2018. Monolithic 9 GHz passively mode locked quantum dot lasers directly grown on on-axis (001) Si. *Applied Physics Letters* 113(4). doi: 10.1063/1.5043200.

Malins, D.B., Gomez-Iglesias, A., White, S.J., Sibbett, W., Miller, A. and Rafailov, E.U. 2006. Ultrafast electroabsorption dynamics in an InAs quantum dot saturable absorber at 1.3 μm. *Applied Physics Letters* 89(17). doi: 10.1063/1.2369818.

Mee, J.K. et al. 2012. A passively mode-locked quantum-dot laser operating over a broad temperature range. *Applied Physics Letters* 101(7). doi: 10.1063/1.4746266.

Mee, J.K., Raghunathan, R., Wright, J.B. and Lester, L.F. 2014. Device geometry considerations for ridge waveguide quantum dot mode-locked lasers. *Journal of Physics D: Applied Physics* 47(23). doi: 10.1088/0022-3727/47/23/233001.

Nikitichev, D.I. et al. 2011. High-power passively mode-locked tapered InAs/GaAs quantum-dot lasers. *Applied Physics B: Lasers and Optics* 103(3), pp. 609–613. doi: 10.1007/s00340-010-4290-5.

Nishizawa, N. 2014. Ultrashort pulse fiber lasers and their applications. *Japanese Journal of Applied Physics* 53(9). doi: 10.7567/JJAP.53.090101.

Peter Vasil'ev 1995. *ultrafast diode lasers fundamentals and applications*. Vasil'ev, P. ed. Norwood: Artech House publishers.

Piston, D.W. 1999. Imaging living cells and tissues by two-photon excitation microscopy. *Trends in Cell Biology* 9(2), pp. 66-69, ISSN 0962-8924.

Qiao, Z. et al. 2022. Modal gain characteristics of a two-section InGaAs/GaAs double quantum well passively mode-locked laser with asymmetric waveguide. *Scientific Reports* 12(1). doi: 10.1038/s41598-022-09136-6.

Radziunas, M., Vladimirov, A.G., Viktorov, E.A., Fiol, G., Schmeckebier, H. and Bimberg, D. 2011. Pulse broadening in quantum-dot mode-locked semiconductor lasers: Simulation, analysis, and experiments. *IEEE Journal of Quantum Electronics* 47(7), pp. 935–943. doi: 10.1109/JQE.2011.2142294.

Rafailov, E.U. et al. 2004. *High-power ultrashort pulses output from a modelocked two-section quantum-dot laser*. Nature Photon (1), pp. 395–401. https://doi.org/10.1038/nphoton.2007.120

Rosales, R. et al. 2011. InAs/InP quantum-dot passively mode-locked lasers for 1.55-μm applications. *IEEE Journal on Selected Topics in Quantum Electronics* 17(5), pp. 1292–1301. doi: 10.1109/JSTQE.2011.2116772.

Shutts, S., Smowton, P.M. and Krysa, A.B. 2013. InP quantum dot lasers with temperature insensitive operating wavelength. *Applied Physics Letters* 103(6). doi: 10.1063/1.4817732.

Silberberg, Y., Miller, D.A.B., Gossard, A.C., Wiegmann, W., Smith, P.W. and Eilenberger, D.J. 1984. Passive mode locking of a semiconductor diode laser. *Optics Letters* 9(11), p. 507. Available at: https://opg.optica.org/abstract.cfm?URI=ol-9-11-507.

Smowton, P.M., Lutti, J., Lewis, G.M., Krysa, A.B., Roberts, J.S. and Houston, P.A. 2005. InP-GaInP quantum-dot lasers emitting between 690-750 nm. *IEEE Journal on Selected Topics in Quantum Electronics* 11(5), pp. 1035–1040. doi: 10.1109/JSTQE.2005.853838.

Soeller, C. and Cannell, M.B. 1996. Construction of a two-photon microscope and optimisation of illumination pulse duration. *Pflugers Archiv European Journal of Physiology* 432(3), pp. 555–561. doi: 10.1007/s004240050169.

Thompson, M.G. et al. 2006. Subpicosecond high-power mode locking using flared waveguide monolithic quantum-dot lasers. *Applied Physics Letters* 88(13). doi: 10.1063/1.2186110.

Thompson, M.G., Rae, A.R., Xia, M., Penty, R. v. and White, I.H. 2009. InGaAs quantum-dot mode-locked laser diodes. *IEEE Journal on Selected Topics in Quantum Electronics* 15(3), pp. 661–672. doi: 10.1109/JSTQE.2008.2012265.

van der Ziel, J.P., Tsang, W.T., Logan, R.A., Mikulyak, R.M. and Augustyniak, W.M. 1981. Subpicosecond pulses from passively mode-locked GaAs buried optical guide

semiconductor lasers. *Applied Physics Letters* 39(7), pp. 525–527. doi: 10.1063/1.92802.

# Chapter 2 :
# Background theory

## 2.1 Introduction

This chapter describes the background theories related to this work. The chapter discusses some principles of semiconductor laser diodes, the quantum dots and the theory of mode-locking (ML). It also provides a description of passive ML and the quantum-confined Stark effect (QCSE). This chapter ends with a brief comparison between gain-guided and index-guided lasers.

## 2.2 Semiconductor Laser diodes

In the context of ultrafast lasers, semiconductor lasers are the best option to reduce the footprint and complexity of various applications. They have many attractive features, such as compactness, lower cost and direct electrical pumping. This section provides a brief background on the basics of semiconductor lasers.

### 2.2.1 The laser structure

The laser structure is a simple separate confinement heterostructure (SCH) (Figure 2.1). The waveguide core of a laser diode consists of a thin undoped layer of active gain material. This layer is surrounded by a barrier material of different compound semiconductors with a large bandgap to confine the carriers in the active layer. The waveguide core is clad by p- and n-regions of a different compound semiconductor with a larger bandgap and lower refractive index to provide transverse optical confinement. The cladding layers, the undoped active region layer and the barrier layers form the p–i–n diode that enables direct current injection. The laser diode is

electrically pumped; the electrons are injected from the n-type region, and the holes are injected from the p-type region. The cladding layers are surrounded by thin, highly doped lower bandgap layers to facilitate the formation of ohmic contacts.

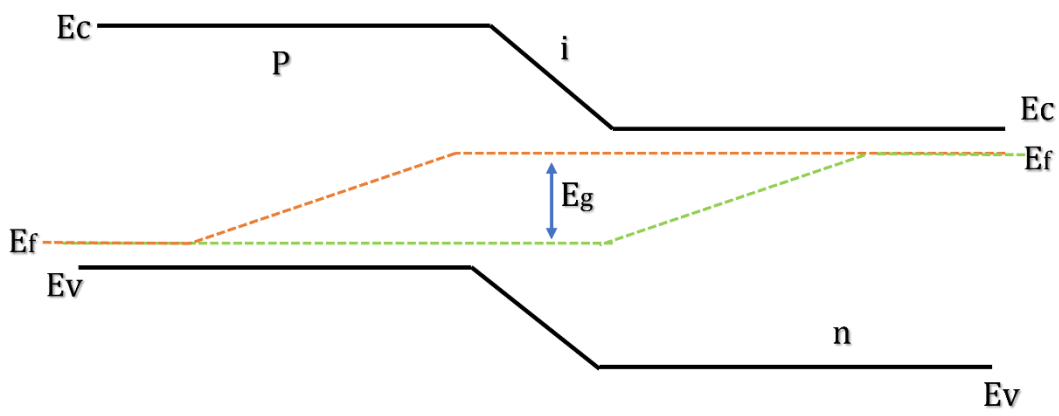


**Figure 2.1: Schematic diagram of pin energy-band.**

In the absence of an external bias, the Fermi level is constant at thermal equilibrium. With the application of the forward bias, the laser operates under a flat-band condition. In this case, electrons and holes are separately in equilibrium due to the population inversion (described in the next section), and the laser is in a quasi-equilibrium situation.

### 2.2.2 The population inversion

In a semiconductor, the energy states of electrons and holes are continually distributed over energy bands separated by forbidden bands, where bandgap energy (Eg) expresses the width of the forbidden band. The Fermi statistics formula that is used to describe the electron occupation probability of both the conduction band and the valence band at thermal equilibrium (at a temperature T) is as follows:

$$f(E) = \frac{1}{1 + \exp(\frac{E - E_F}{k_B T})} \qquad (2.1)$$

where $E_F$ is the Fermi energy. Since $E_g > k_B T$, the numbers of electrons in the valance band are much larger than in the conduction band. An inversion must occur to the conduction and valance bands populations to obtain an optical gain. Therefore, the

occupation probability of the conduction band must exceed that of the valence band. This may be interpreted in terms of Fermi functions by substituting into the condition $f_2 > f_1$ as follows:

$$E_{F2} - E_{F1} > E_2 - E_1 \quad \rightarrow \quad \Delta E_F > hv \qquad (2.2)$$

This population inversion for a semiconductor is described by the Bernard and Duraffourg condition (Bernard and Duraffourg 1961), which implies that the quasi-Fermi level separation must be greater than the photon energy. Carriers injected into the semiconductor material through p-n junctions allow the persistence of population inversion.

### 2.2.3 Fabry-Perot semiconductor laser

Two plane parallel mirrors, one at each end of the gain medium, define a diode laser as a Fabry-Perot resonator. Two parallel facets are created reflectively (R1, R2) for optical feedback by cleaving along crystal planes. As long as the excitation source operates, a laser continuously emits light. Only the light that is precisely perpendicular to the cavity's axis will propagate back and forth within the cavity. In the presence of optical feedback, the stimulated emission can overcome the losses and dominate over the spontaneous emission yielding net optical gain(Coldren et al. 2012).

#### 2.2.3.1 Threshold gain

Figure 2.2 illustrates a Fabry-Perot laser of a gain medium of length L with two parallel reflective facets, $R_1$ and $R_2$. The net modal gain is the increase in the photon density per unit length. The gain threshold is reached when the gain is equal to the losses. The losses within a round trip can be classified into two categories: the internal loss ($\alpha_i$), which results from the free carrier absorption or scattering and the mirror loss ($\alpha_m$). The round trip gain and loss per cm can be written as follows:

$$round\ trip\ gain = \exp(2GL) \qquad (2.3)$$

$$round\ trip\ loss = \mathrm{R}_1\mathrm{R}_2\exp(-2\alpha_i L) \qquad (2.4)$$

The gain threshold must be equal to the gain to reach the threshold (lasing) and can be written as $round\ trip\ gain \times round\ trip\ loss = 1$, by substituting equation 2.3 and equation 2.4 , the gain threshold will be

$$G_{th} = \alpha_i + \frac{1}{2L}\ln\left(\frac{1}{R_1R_2}\right) = \alpha_i + \alpha_m \qquad (2.5)$$

So $\alpha_m$ will be

$$\alpha_m = \frac{1}{2L}\ln\left(\frac{1}{R_1R_2}\right) \qquad (2.6)$$

The reflectivity for semiconductor material is approximately 30% produced from its refractive-index step (approximately 3.5); therefore, $R_1$=$R_2$=0.33. Equation (2.6) will be

$$\alpha_m = \frac{1}{L}\ln\left(\frac{1}{R}\right) \qquad (2.7)$$

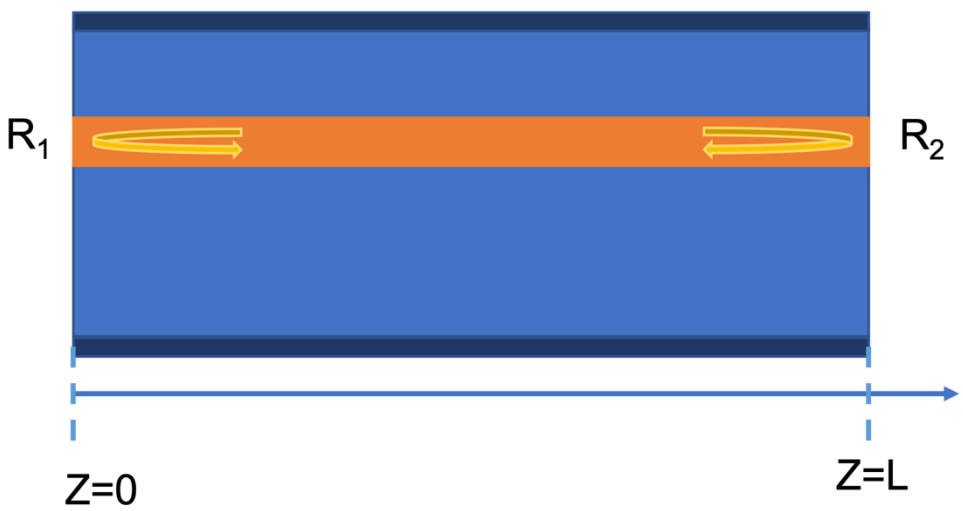


**Figure 2. 2: Fabry Perot laser.**

#### 2.2.3.3 Gain-current relation

The gain-current relation is a plot which shows the net gain peaks as a function of current density. This relation aids in estimating the transparency current, threshold current and the differential gain of the material. The transparency current is the

quantity needed of current for the absorption to go to zero (gain also zero) whereas threshold current is referred to the quantity needed of current for the gain to equal the loss. It can be found by fitting experimental data, for example, plotting the experimental net gain peaks, measured by the segmented contact method, as a current function. The curve fit used in this relation is as follows:

$$G_{Peak} = G_0 \ln\left(\frac{J}{J_{trans}}\right) \qquad (2.8)$$

Where $G_0$ and $J_{trans}$ are fitting parameters.

The net gain as a function of current density illustrating the gain threshold and the differential gain and loss is plotted in Chapter 4.

### 2.2.4 Quantum confinement: Density of states

The concept of the density of states (DOS) in semiconductor physics describes the closely spaced electronic states that result from the interaction of the electron wave functions that may be found in an extended piece of crystalline material. The following equation provides the DOS (ρ) for electrons in bulk or three-dimensional (3D) material with energies between E and E+dE per unit volume (Wartak et al. 2006).

$$\rho(E) = \frac{1}{2\pi^2}\left(\frac{2m^*}{\hbar^2}\right)^{3/2}(E - E_C)^{1/2} \qquad (2.9)$$

The unit of $\rho(E)$ is $(eV^{-1}m^{-3})$.

Where m* is the effective mass of the electrons in the material and Ec is the edge of the conduction band. Figure 2.3 Shows the DOS variations of electrons and holes with the reduction of dimensionality: bulk materials in terms of the solid parabolic curves, quantum well (QW) in step-function represented by dashed lines, quantum wire in shark-fin form and quantum dot (QD) in delta-function for a set of identical QD confined in the zero dimensions. Band edges have a small number of possible electronic states because of the dependence of DOS on the square root of energy.

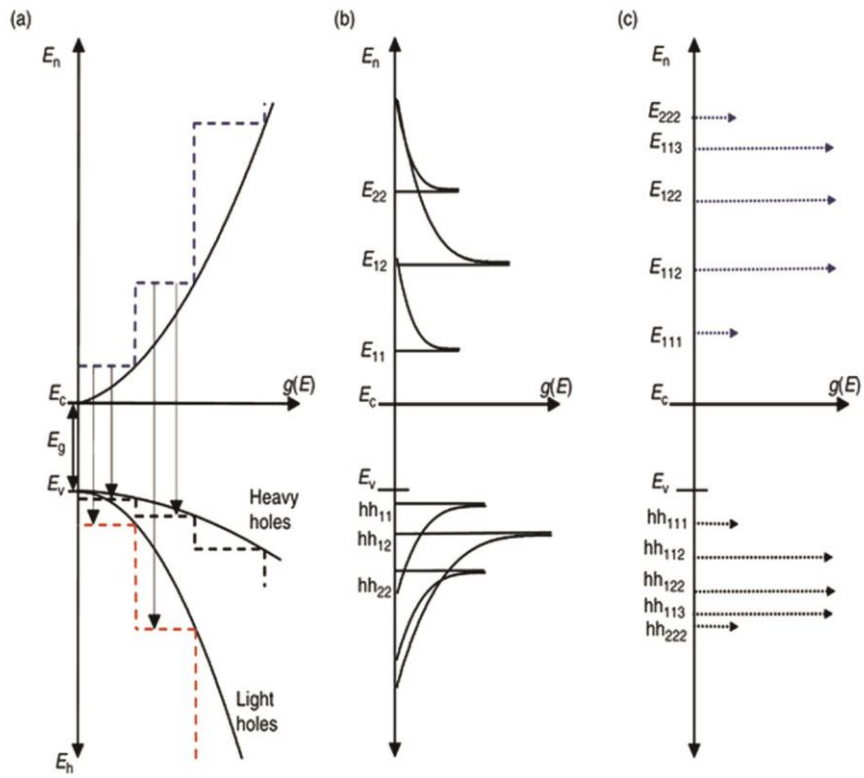


**Figure 2. 3: the electrons and holes DOS for: (a) bulk materials and quantum well (QW); (b) Quantum wire; (c) Quantum dot (QD)(Smowton 2012).**

Decreasing the width of the material active region into a thickness which is comparable to the electron's de Broglie wavelength within a potential well, so the electrons are confined in one dimension. Therefore, the previous equation for the 3D DOS is no longer relevant. Therefore, a two-dimensional DOS is given in the following equation for energies between E and E + dE per unit area:

$$\rho(E)(eV^{-1}m^{-2}) = \sum_n \frac{m^*}{\pi\hbar^2}\,\Theta(E - E_n) \qquad (2.10)$$

Where En is the sum of the confined energy level within the QW, and Θ (E-En) is the Heaviside step-function (if E > En, this Θ (E-En) will be zero or unity). This equation can be used to determine both electrons and holes step-function shaped DOS with the appropriate value of effective mass, and it is illustrated schematically in Figure 2.3 (a).

By using the solution of the time-independent Schrödinger equation in one dimension, the electron wave function and energetic position of the energy levels within the QW can be determined as follows:

$$E_n + V_b = \frac{\hbar^2 k^2}{2m^*} \qquad (2.11)$$

Where k is the wavevector propagating within the well, $V_b$ is the finite barrier height of a potential well and $E_n$ is the energy of the nth quantum level. The overlap between electron and hole wave functions limits the efficiency of radiative transitions from confined electron levels to confined hole levels. The maximum overlap is achieved for wave functions with the same symmetry. The vertical arrows in Figure 2.3 (a) display the allowed optical transitions for both electrons to heavy holes and electron to light holes (n=1 and n=2), where the lowest optical transition (n=1) or the optical transition of ground-state ($E_{opt}$) can be identified from the following equation:

$$E_{opt} = E_g^{QW} + E_{el} + E_{hh1} \qquad (2.12)$$

Where $E_g^{QW}$ is the QW bandgap, and $E_{el}$ and $E_{hh1}$ correspond to E in equation (2.10). These $E_{el}$ and $E_{hh1}$ values can be calculated if the effective mass and height of the potential barrier for electrons and heavy holes are known.

The change in the width of the QW affects the energetic position of the confined energy levels within the QWs. Decreasing the QW width will raise the energetic position of the confined states, whereas increasing the QW width will lower the energetic position.

Quantum wire is one-dimensional DOS illustrated schematically in Figure 2.3 (b). For energies between E and E + dE per unit length, the DOS is given as the following:

$$\rho_{n,m}(E)(eV^{-1}m^{-1}) = \sum_n \sum_m \sqrt{\frac{m^*}{2\pi^2\hbar^2}\, n_{QWr}\left(E - E_{n,m}\right)^{1/2}} \qquad (2.13)$$

where $n_{QWr}$ ($cm^{-1}$) is the density of the quantum wire's surface. In this case, the degeneracy is accounted for in the shown DOS of the quantum wire.

The formula of zero-dimensional surface DOS for QDs as a delta-function, which is illustrated schematically in Figure 2.4 (c), is given as the following:

$$\rho_{n,m,l}(E) = \sum_n \sum_m \sum_l 2n_{QD}\delta(E - E_{n,m,l}) \qquad (2.14)$$

Where δ ($E–E_{n,m,l}$) is the delta function and $n_{QD}$ ($cm^{-2}$) is the surface density of the QDs. The greater magnitude of the DOS indicates the degeneracy of some dot states. Tuning the transition energy is further enhanced by the inclusion of QDs. This allows the tuning of a laser's operating wavelength (Smowton 2012).

## 2.3 Quantum Dots

QDs are nano-scale-sized clusters of semiconductor material known as 'artificial atoms'. The rationale behind this name is that the energy distribution of charge carriers (electrons or holes) in these systems is similar to the electrons in an atom; the carriers can only occupy a certain range of energy levels. Self-assembled QDs are grown using the Stranski–Krastanow (SK) technique. The formation of dots in this technique, based on the lattice-mismatched heteroepitaxy, leads to the growth of self-organised QDs. In this process, when a certain critical thickness has been attained during the epitaxial growth of a film A over a substrate B, three-dimensional islands start to form. The condition of this spontaneous formation is that the lattice constant of the deposited material is larger than the one in the substrate. These 3D islands serve as a strain-relief mechanism that is an alternative to the formation of dislocations. The island's base must be strained to fit to the substrate, whereas the island's top surface can relax elastically to reach its bulk lattice parameter. These 3D islands are the QDs. Dots differ in size, height, and composition as a result of statistical fluctuations that occurred throughout growth (Woll et al. 2002). Therefore, the dot's sizes are not identical as in the approach of delta-function surface DOS described in Section 2.2.4 QDs have a Gaussian size distribution due to the self-organised QDs, thus, a Gaussian distribution of relative energy levels (see Figure 2.4). These QDs provide significant benefits for ultrafast lasers; therefore, this section focuses on the advantages of these QDs in ultrafast technology.

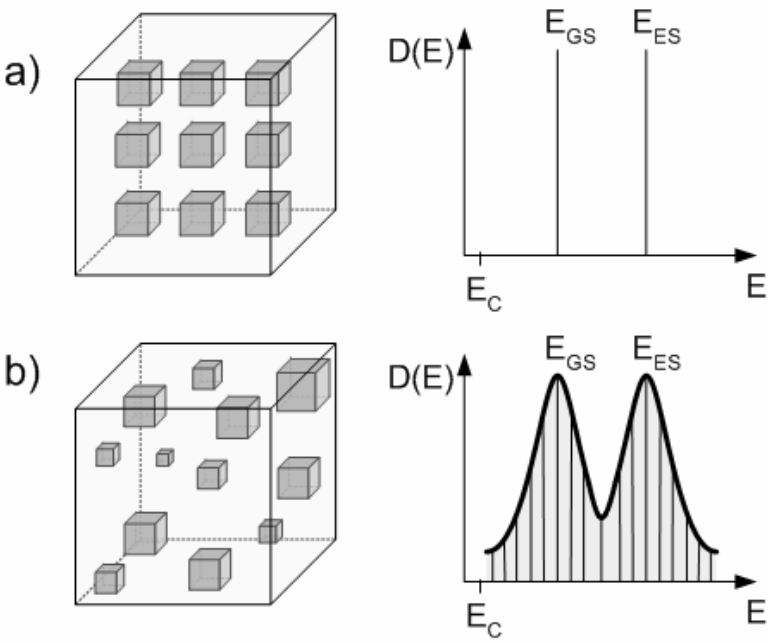


**Figure 2. 4: The figure at the left represents the morphology of QDs, and at the right displays the DOS for carriers in (a) an ideal quantum-dot system; (b) an actual quantum-dot system illustrating the effects of inhomogeneous broadening on the DOS(Rafailov and Avrutin 2013).**

### 2.3. 1 Advantages of QDs

**Inhomogeneous broadening of gain:** This is attributed to dot size distributions. The inhomogeneous broadening is not a negative aspect, as it had been thought before; this broadening results in access to a broader range of wavelengths (Smowton 2012). The wavelength range could be increased by modifying the dot growth environment. The broad gain spectrum can also benefit tuneable and ultrafast lasers to generate ultrashort pulses. However, the drawback associated with inhomogeneous broadening is the resulting low gain level.

**Low threshold current density and low level of amplified spontaneous emission**: QD diode lasers have the advantage of initiating lasing with a very low threshold current, providing an efficient and compact source for ultrafast lasers operating with low power. This is important in the operation of ML because the ML regime usually occurs at the threshold of the laser (Rafailov & Avrutin, 2013). In addition, a low threshold eliminates the requirement for higher carrier density while pumping the

laser, which reduces amplified spontaneous emission (ASE) and thus reduces the optical noise in the obtained train of pulses.

**Low-temperature sensitivity:** In contrast to other types of lasers, QD lasers are less sensitive to temperature variations because of the discrete nature of their DOS (Smowton et al., 2008). Therefore, there is no need for thermo-electric coolers; hence, cheap, compact and lower-power mode-locked lasers can be made using these materials.

**Ultrafast gain and absorption recovery dynamics:** QD structures provide ultrafast recovery under absorption and gain conditions because the carriers have many different options for recombining. The presence of these recombination pathways for the carriers and a reservoir of carriers at high carrier populations is due to the proximity of energy states of the wetting layer, barrier layer and the higher-energy excited states (Borri, 2006). Ultrafast recovery time is crucial for the saturable absorber used for a passively monolithic MLL to ensure fast recovery to provide stable pulses with a high repetition rate and low jitter (Edik U. Rafailov, 2011).

## 2.4 Fundamentals of ML

### 2.4.1 Longitudinal modes in a laser resonator

The existence of longitudinal modes of an optical resonator is the most significant property for the generation of ultrashort pulses. For laser oscillations to arise within the cavity, a wave must self-replicate after a few reflections, leading to constructive interference of their electric fields and a summation in phase. The back-and-forth propagation of waves between the laser facets forms a resonant cavity, resulting in standing waves. The condition for the existence of the standing waves is that the length of the laser resonator should be equal to a positive integer multiple of the half-wavelength of the light. Therefore, the discrete sets of frequencies created from the standing wave are known as the longitudinal modes.

In a laser resonator, the longitudinal modes $\lambda_m$ propagating along the laser's optical axis are given as the following:

$$\lambda_m = \frac{2L}{m} \rightarrow \nu = \frac{mc}{2L} \qquad (2.15)$$

Where m is the mode order. If Δm = 1, the frequency space between the adjacent longitudinal modes is given as the following:

$$\Delta\nu = \frac{c}{2L} \qquad (2.16)$$

The round-trip time of the travelling wave can be written as the following:

$$T = \frac{2L}{c} \qquad (2.17)$$

Only cavity modes, which lie within the gain bandwidth of the laser material, may initiate the laser. For a mode to start propagating in laser action, its optical gain must be higher than its optical loss. Few modes would experience net optical gain and initiate lasing under appropriate pumping. Figure 2.5 illustrates the profile of the laser gain spectrum, the cavity longitudinal modes and the laser output spectrum. The output

of a typical CW laser has a random intensity fluctuating over an average value because the modes lase in a random pattern.

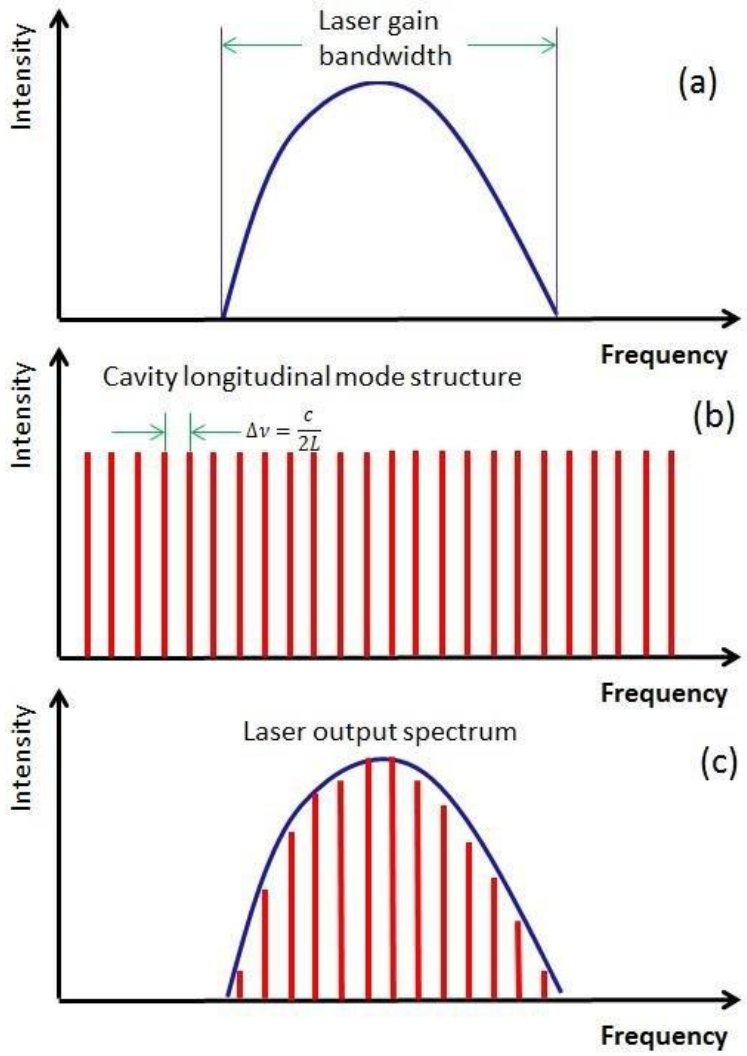


**Figure 2. 5: The profiles of (a) the gain spectrum; (b) the longitudinal modes; (c) the lasing output.**

### 2.4.2 Mode-locking

Mode-locking is a technique for generating a train of ultrashort pulses of extremely short duration in the picosecond or femtosecond range. These ultrashort pulses also have a very high peak optical power, even though the average output power is low. This is because the light is now squeezed into very short pulse durations rather than being generated continuously, as in CW operation. This can be achieved by locking the phases of constructive longitudinal modes of the laser cavity. These modes meet the resonance condition of the laser cavity; the generation of pulses with a repetition rate is equivalent to the cavity round-trip duration. In a standing-wave resonator, the pulse repetition frequency ($f_R$) is stated as follows:

$$f_R = \frac{c}{2nL} \qquad (2.18)$$

where C is the speed of light in a vacuum, n is the refractive index and L is the total laser cavity length.

There are three main forms of ML: active ML, hybrid ML and passive ML. The active ML method involves placing a modulator within the laser cavity. This modulator locks the laser into a particular mode when driven by an electric signal and produces amplitude modulation of the cavity, thus, ML the laser. Passive ML does not need external components; instead, the light inside the laser cavity is modulated by adjusting the intra-cavity elements. The hybrid ML method is a combination of the above two ML forms. This thesis focuses on passive ML; therefore, this form will be deeply described in the following section.

### 2.4.3 Passive ML

Passive mode-locked lasers are the best ML form among all the three forms described briefly above in terms of generating the shortest pulses. Additionally, the manufacture and operation of theses passive lasers are the simplest among all other ML forms (Rafailov & Avrutin, 2013). Furthermore, passive ML provides higher pulse repetition rates that are only controlled by the cavity length. These lasers are based on a saturable absorber monolithically integrated into the same structure by electrically isolating one section of the device. Therefore, the structure consists of two isolated sections: the gain section and the saturable absorber (SA) section (Figure 2.6). Applying a forward bias on the gain section will cause the formation of laser pulses. However, applying a reverse bias on the SA section will cause the formation of ultrashort pulses circulating in the laser cavity. This occurs because the photo-generated carriers can be swept out of the SA section more effectively, allowing the SA to recover to its initial state of high loss more quickly. Thus, the gain section is responsible for the broadening of the pulses, while the SA section is responsible for the shortening of the pulses. The increase in the reverse bias decreases the absorber recovery time, which shortens the pulses even more.

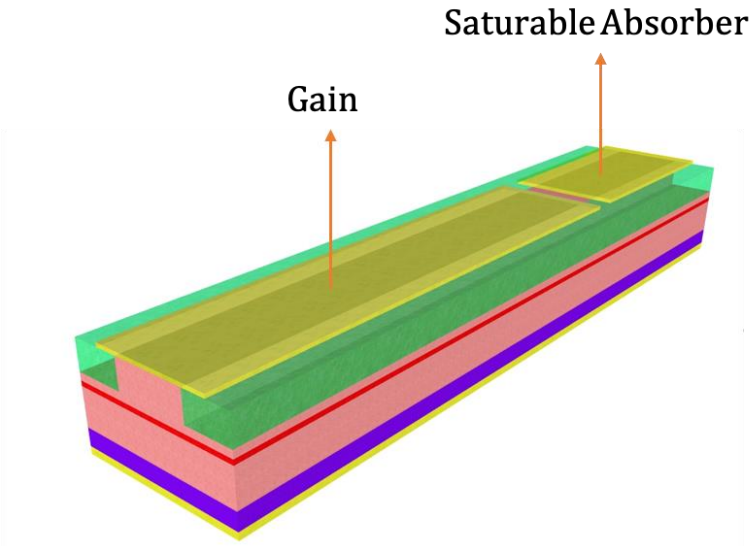


**Figure 2. 6: Schematic diagram of the design of passive mode-locked laser.**

The dynamic of gain and absorption with time will be described here to further understand this mechanism (Edik U. Rafailov, 2011). Those two factors (gain and

absorption) control the pulse shaping. At the onset of laser emission, the laser modes initially fluctuate with random relative phases, such that the radiation pattern consists of noise bursts. If one of these bursts is intense enough to provide a fluence close to the absorber's saturation fluence, it will bleach the absorption. This indicates that the loss will be less near the peak of the burst, where the intensity is highest, while the low-intensity wings will become more attenuated. Thus, this family of intensity spikes triggers the pulse generation process with lower losses during the absorber's carrier lifetime. Once the optical intensity is increased, the loss in a SA reduces. This property distinguishes between a continuous wave and a pulsed operation and may assist a self-starting mechanism for ML. After a period of time, the absorber saturates faster than the gain, allowing a high-intensity peak to be emitted. After that, the recovery of the absorber is more rapid than that of the gain (see Figure 2.7).

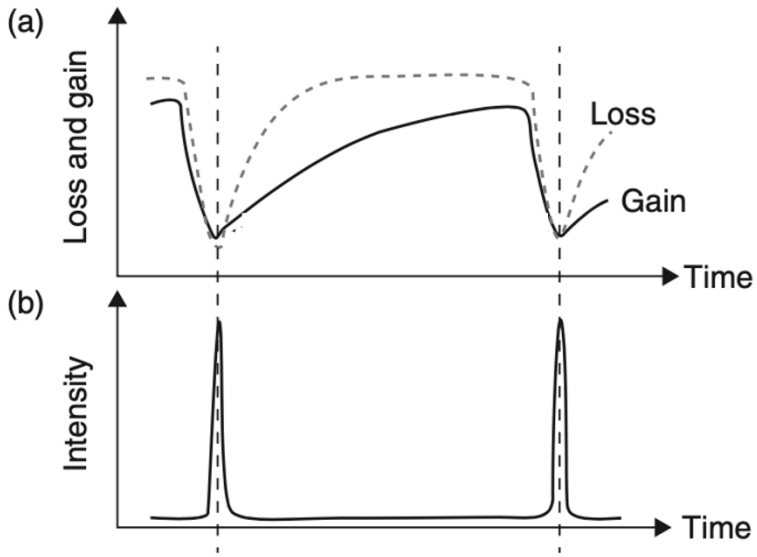


**Figure 2. 7: Dynamics of loss and gain for the generation of short pulses.**

#### 2.4.3.1 Passive ML: Stability condition

An increase in injected current density on the gain section will cause the broadening of pulses, and increasing the reverse bias will affect the shortening of pulses (Edik U. Rafailov, 2011). Thus, a balance between pulse broadening and pulse shortening ensures the stability of MLL. The loss must saturate faster than the gain to generate optical pulses from passive MLL. The stability condition of Passive MLL can be determined from the saturation energy; the saturation energy is the energy required to saturate the absorption or the gain, and the following equation represents this relation

$$E_g^{sat} = \frac{h\nu A}{dg/_{dn}} > E_a^{sat} = \frac{h\nu A}{da/_{dn}} \qquad (2.19)$$

Where $E_g^{sat}$ is the gain saturation, $E_a^{sat}$ is the absorption saturation, $h$ is Plank constant, $\nu$ is the frequency, A is the cross-section modal area, dg/dn and da/dn are the differential gain and differential loss, respectively (Figure 2.8).

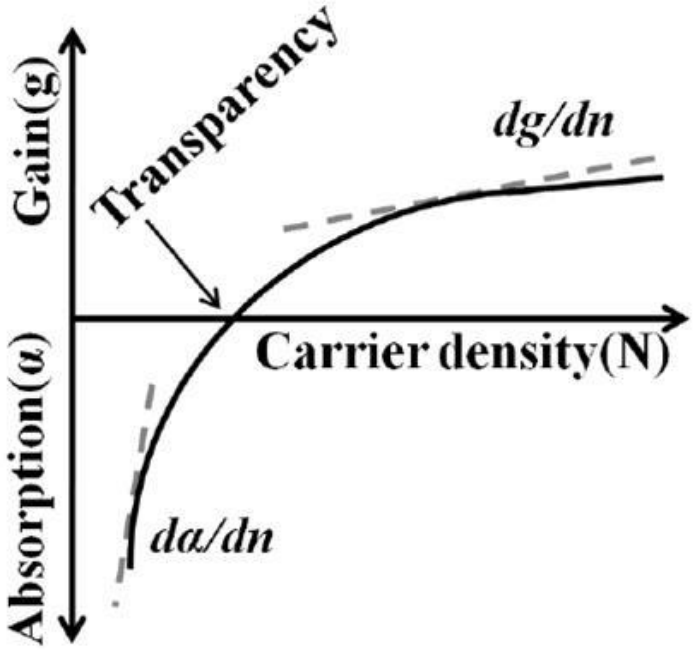


**Figure 2. 8: The gain and absorption as a function of carrier density illustrating the differential gain, loss and the transparency point (Edik U. Rafailov, 2011).**

### 2.4.4 Time bandwidth product

According to the Fourier transform, there is an inverse relationship between the temporal width of a mode-locked pulse and the gain bandwidth of its optical spectrum (Figure 2.9). The product of the temporal pulse width and the gain bandwidth is known as the time-bandwidth product (TBP). There is a minimum pulse duration that corresponds to a specific frequency bandwidth. If the optical spectrum of the pulse is at the minimum duration, the pulse is then considered transform-limited. The TBP of a pulse may be easily determined by measuring full-width at half maximum (FWHM) of the pulse's optical spectrum. The TBP is equal to a constant $k$ whose value depends on the pulse's shape, which may be Gaussian, hyperbolic secant squared or Lorentzian.

$$k = \Delta v . \Delta \tau \ \rightarrow k = \frac{c}{\lambda^2} \Delta \lambda . \Delta \tau \qquad (2.20)$$

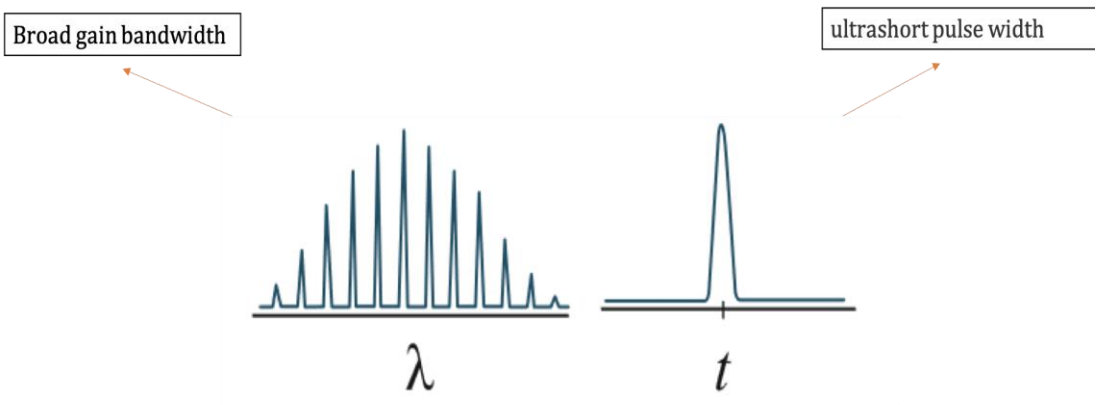


**Figure 2. 9: Spectral pulse versus temporal pulse.**

## 2.5 Quantum Confined Stark Effect

QCSE is a theory which describes the influence of applied DC electric field (EF) on the electron and hole wave function of a QW and, thus, on the absorption spectrum [4]. When the QW laser is at equilibrium, no EF is applied. The probability densities of the electron and hole wavefunction of the first quantised levels of a QW are symmetric in

the middle of the well, or the peak of the electrons and hole distribution is in the centre of the well (as shown in the Figure 2.10 (a)). When an external EF is applied on the same QW structure along the z-axis (growth direction), the well potential will get bent and thus destroy the symmetry of electron and hole wave functions (see Figure 2.10(b)). The EF will displace the electrons and holes in the opposite direction, but this will not ionise the excitons due to the high confinement. This EF reduces the overlap between the electron and hole functions, separating them with a space. This space between the electron and the hole wave function is known as space charge or polarisation of the carriers. This space increases with higher applied EF, and thus the reduction of the overlap increases with higher values of EF as well due to the reduction in the oscillator strength (oscillation intensity). In addition to the overlap reduction, the energy gap decreases with increasing external EF, which causes the quantised energy levels (confined states) of the excitons to shift to lower energy values, known as the redshift. This is called the QCSE (Mark Fox 2010).

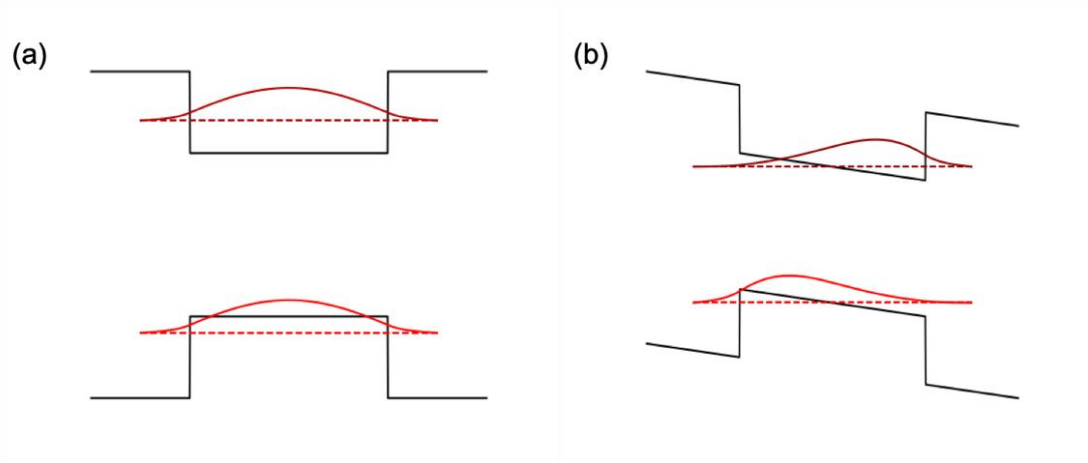


**Figure 2. 10: The influence of applied EF on the QW: (a) No EF is applied, (b) An external EF is applied.**

## 2.6 Device structures

A waveguide, with a refractive-index profile that varies spatially, is a common method to confine the light in the Z-direction (transverse confinement) to ensure that the optical mode propagates in the plane of the active region. However, the light can also be further confined by controlling the contact geometry. In the case of gain-guided device geometry, the light is confined in the active layer (top semiconductor layer) by means of varying the optical gain spatially. The index-guided device geometry is confined by a built-in refractive index profile created in either the top semiconductor layers or the adjacent cladding layers (Peter Blood 2015).

### 2.6.1 Gain-guided geometry: Stripe lasers

The oxide-isolated stripe usually has a width which varies from 10 μm to 60 μm for different devices. It is made by depositing a $SiO_2$ layer on the surface of the wafer. The width is created by photolithography. The final step to make the contact stripe is to deposit a metal layer over the whole surface. However, the current flow is not well restricted. The current flows toward the back contact in the x-direction, with spreading increasing and becoming larger at the back contact. The actual width of the stripe laser after electrical pumping is not the same as the width before pumping; it is usually wider (see Figure 2.11). Table 2.1 shows the advantages and disadvantages of stripe lasers. These lasers are simple to fabricate and were widely used to assess the design of the active region. However, the current spread from the stripe laser, due to the lack of lateral confinements, can cause the side lobes in the far-field patterns. These side lobes lead to the increase of the effective stripe width and thus filamentation happens at the junction plane.

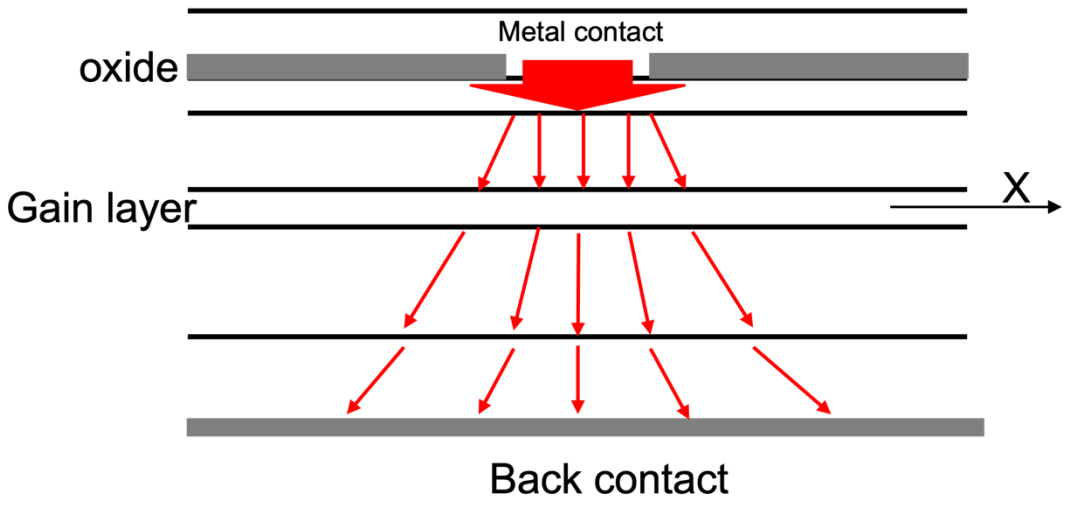


**Figure 2. 11: Schematic diagram of the cross-section of stripe laser illustrating the current spreading.**

**Table 2. 1: Advantages and Disadvantages of stripe lasers.**

| Advantages | Disadvantages |
|---|---|
| Simple to fabricate | Current spreading |
| Useful structure to assess the design of the active region | Lobs in the far-field pattern |
| | Filamentation happens at the junction plane |

### 2.6.2 Index-guided geometry: Ridge lasers

The ridge laser is made by etching the material away from the stripe's sides. The narrow ridge is formed by etching the upper layers into the cladding layers with dielectric deposition. This results in a narrow mesa that guides the light and the current. The etched regions outside the ridge exhibit a lower effective index than the region beneath the ridge. This leads to a lateral variation in the effective index, localising the mode in the region under the stripe. Table 2.2 shows the advantages and disadvantages

of ridge lasers. The most important advantage of ridge laser is the reduction of the current spread which can lead to strong lateral confinements. Therefore, these lasers can support only one lateral mode. However, these lasers exhibit high leakage current due to the exposed surface of the mesa. Additionally, the side-wall recombination causes the increase of non-radiative recombination. Those two disadvantages are the main reasons of the high threshold current in these lasers.

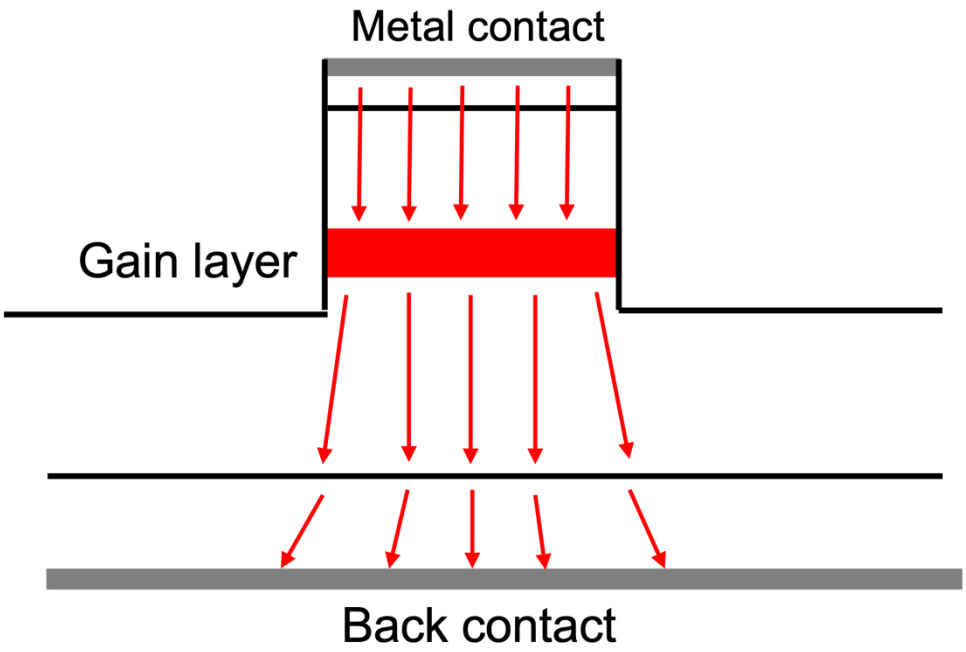


**Figure 2. 12: Schematic diagram of the cross-section of ridge laser.**

**Table 2. 2: Advantages and Disadvantages of ridge lasers.**

| Advantages | Disadvantages |
|---|---|
| Reduction in current spreading | Leakage of current due to the exposed surface of the mesa |
| Can support only one lateral mode | Non-radiative recombination due to the surface (side walls) recombination |

There are two main types of ridge lasers: the shallow ridge and the deep ridge. The difference between them is the etch depth. In case of shallow ridge, the etching stop at the cladding layer.

## 2.6 Summary

This chapter involves background theories and the most relevant basics of a semiconductor laser related to this work. Further, the quantum dots are also briefly described. Additionally, the fundamental of ML is discussed with an in-depth description of the passive ML technique. Moreover, the QCSE is included. The chapter ends with a brief comparison between the gain-guided and index-guided device contact geometry.

## References

Bernard, M.G.A. and Duraffourg, G. 1961. Laser Conditions in Semiconductors. *physica status solidi (b)* 1(7), pp. 699–703. doi: 10.1002/pssb.19610010703.

Coldren, L., Corzine, S. and Mashanovitch, M.L. 2012. *Diode Lasers and Photonic Integrated Circuits*. Second edition. WIELY.ISBN: 9781118148167.

Edik U. Rafailov, Maria Ana Cataluna and Eugene A. Avrutin 2011. *Ultrafast Lasers Based on Quantum dot Structure:Physics and Devices*. first edition. Rafailov. Edik, Cataluna. M. Avrutin. E. ed. Germany: WIELY-VCH.

Mark Fox 2010. *Optical Properties of Solids*. second edition. Fox. Mark ed. New York: Oxford University Press.

Peter Blood 2015. *quantum confined laser devices*. First edition. Blood, P. ed. New York: Oxford University press.

Rafailov, E.U. and Avrutin, E. 2013. Ultrafast pulse generation by semiconductor lasers. In: *Semiconductor Lasers: Fundamentals and Applications*. Elsevier Ltd, pp. 149–217. doi: 10.1533/9780857096401.1.149.

Smowton, P.M. 2012. Quantum-dot lasers: Physics and applications. In: *2012 Conference on Lasers and Electro-Optics, CLEO 2012*. doi: 10.1016/b978-0-12-803581-8.00836-5.

Smowton, P.M., George, A., Sandall, I.C., Hopkinson, M. and Liu, H.Y. 2008. Origin of temperature-dependent threshold current in p-doped and undoped In(Ga)As quantum dot lasers. *IEEE Journal on Selected Topics in Quantum Electronics* 14(4), pp. 1162–1170. doi: 10.1109/JSTQE.2008.920040.

Wartak, M.S., Weetman, P., Alajoki, T., Aikio, J., Heikkinen, V., Pikhtin, N.A. and Rusek, P. 2006. Optical modal gain in multiple quantum-well semiconductor lasers based on InP. *Canadian Journal of Physics* 84(1), pp. 53–66. doi: 10.1139/P06-005.

Woll, A.R., Rugheimer, P. and Lagally, M.G. 2002. Self-Organized Quantum Dots. *Selected Topics in Electronics and Systems/ Quantum Dots,* pp. 45-78, doi: 10.1142/9789812777676-0003

# Chapter 3: Epitaxial structures, Experimental Techniques, and Experimental Set-up

## 3.1 Introduction

This chapter provides information about the epitaxial structures of the devices used in this study, the experimental techniques and set-up. It briefly covers types of contact geometry of lasers used in this study. The contact stripe is used in multi section non-lasing devices and fabricated ridge mode-locked lasers (MLL). This is following by a detailed description of the experimental technique used to characterise the materials which is known as Segmented Contact Method (SCM). The chapter also covers the measurement of modal absorption under the reverse bias and the Near-field measurements.

## 3.2 Epitaxial structures

Smowton et al. (2005, 2010), and Elliot et al. (2012), have studied the influence of growth conditions (the growth temperature and using misoriented substrates) on InP QDs, and the compound compositions of the layers. These changes has affected the wavelength range. The epitaxial growth technique is metal organic chemical vapor deposition (MOCVD). The longest wavelength and good performance of InP QDs achieved in the range from 690nm to 750nm under growth temperature 710 ºC and orientation of the QD layer in regard to the substrate is 10º off (100) toward [111]. (Karomi, I. et. al. (2015)) have achieved a longer wavelength, broader width of gain spectrum, with wavelength ranging from 730nm to 775nm by adding arsenic to InP QDs under the same growth condition and better performance in term of gain spectrum and laser threshold.

The active region of the epitaxial structures studied utilising both InP and InAsP QDs (III-V compound semiconductors) follow the quantum dot-in-a-well (DWELL) system. The waveguide core is comprised of five layers of InP or InAsP QDs embedded in 8nm thick GaInP QW layers. The barrier regions of each QW are formed by the inclusion of 16nm thick AlGaInP layers. The waveguide cladding consists of two layers of $Al_{0.52}In_{0.48}P$, doped with Zn and Si respectively to form the p and n sides of a p-i-n diode. These layers were grown on n-GaAs (1 0 0) substrate oriented 10° off toward <1 1 1> and capped with p- GaAs as seen in Figure 3.1. The real densities of the dots are in the range of $10^9$ to $10^{10}$ $cm^{-2}$. These structures were grown by Dr. Andrey B. Krysa in the EPSRC National Centre for III-V Technologies, the University of Sheffield using a growth technique known as MOVPE. The dots were grown using the Stranski-Krastanov self-assembled method.

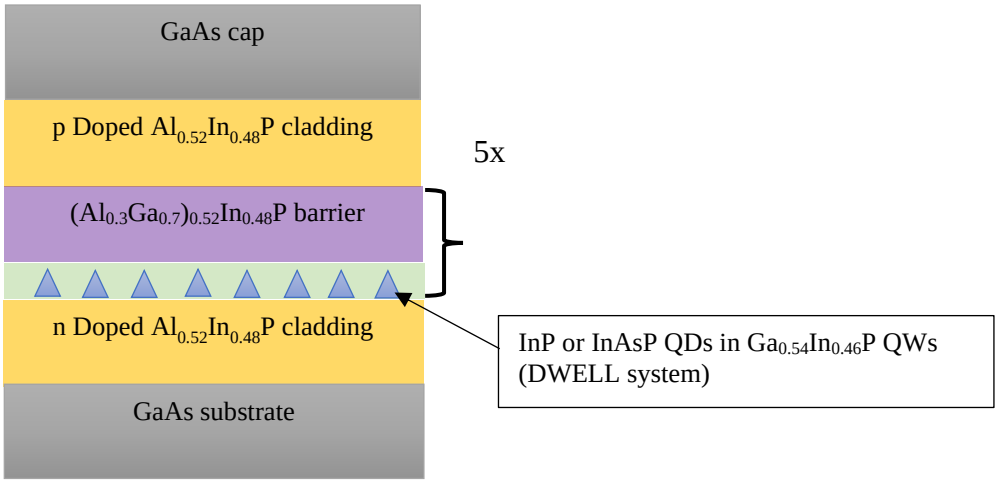


**Figure 3. 1: Schematic diagram of the structure layers of both QDs material InP and InAsP.**

Whilst the emission of InP QDs can be extended to longer wavelengths with the inclusion of arsenic in the QD composition, forming InAsP QDs, this also affects the size and inhomogeneity of dots. It has been shown that InAsP QD materials have a higher degree of QD size inhomogeneity than in InP QD materials. This inhomogeneity is obvious in the TEM images seen in Figure 3.2, which shows the irregularity of the vertical stacks in InAsP QDs and the decrease in QD size in comparison the InP QDs, with a height of 2-3 nm and a lowermost dot diameter of 20-30 nm. In contrast, the InP TEM image shows regular vertical stacks and larger dots

with a height of 4-5 nm and a dot diameter of 40-50 nm. The reason for the increased variability and irregularity in dots size and shape in InAsP is the higher lattice mismatch between the dots layer and the substrate that occurs with adding arsenic to the InP during QD growth (Krysa, A. B., 2016).

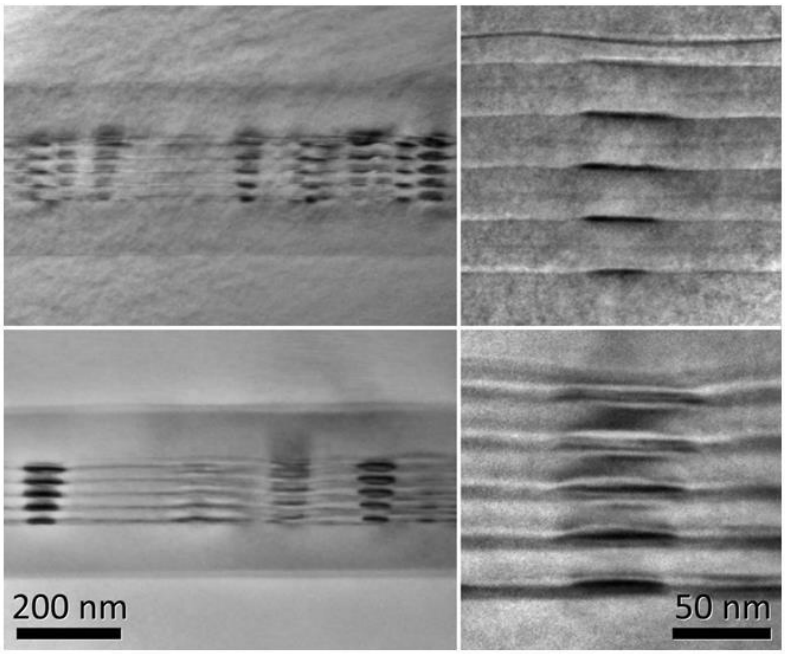


**Figure 3. 2: TEM images of the active region of InAsP dots (upper) and InP dots (lower).**

## 3.2 Device Fabrication and sample preparation mounting

The epitaxial structures studied were fabricated by Dr Zhibo Li into passively monolithic MLLs and non-lasing test structures. The non-lasing test structures were 50 µm wide broad-area oxide-isolated stripes, with segmented contacts of length of 300 µm. The metal contact for each segment was 292 µm long, and the gap between each segmented contact was 8 µm. The highly p-doped conductive GaAs cap layer was etched between adjacent segments to improve electrical isolation between segments but was not sufficiently deep to affect the optical mode in the waveguide. The non-lasing test structures were cleaved into 10 section long (3 mm) cavity lengths and emission measured from the as-cleaved uncoated facets.

Two section passively monolithic MLLs were fabricated as 2 µm wide ridge lasers. A 20 µm gap was defined to separate the p-metal contact into two, forming the gain and

saturable absorber sections of the device. The highly p-doped GaAs contact layer was also removed to improve electrical isolation between the gain and saturable absorber contacts. A range of passively monolithic MLLs were cleaved with different total cavity lengths, and ratios of gain to absorber lengths. Emission was measured from the as-cleaved, uncoated facets.

Mode-locked lasers with total cavity lengths of 3 mm have been examined, with absorber-to-gain length ratios of 1:4, 3:17,1:9 and 1:19.

Figure (3.3) shows an illustration of the passively monolithic MLL, and a scanning electron microscope image of the ridge.

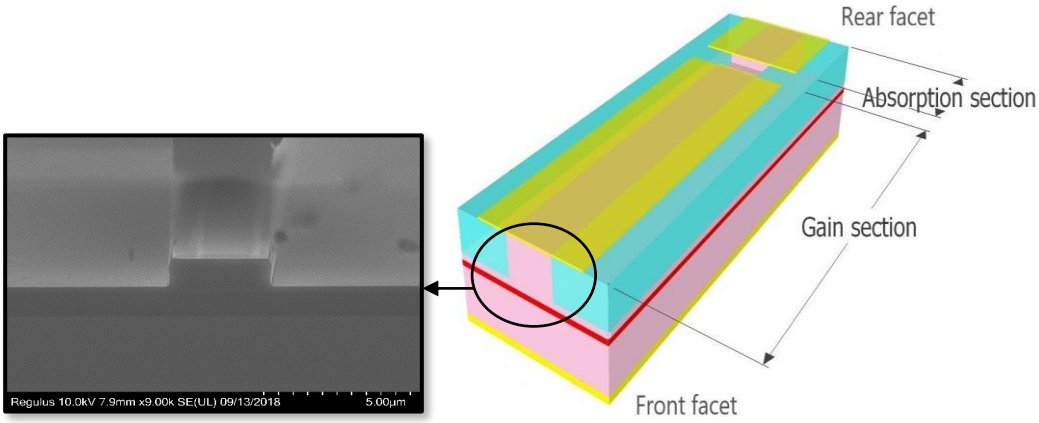


**Figure 3. 3: Schematic diagram of the ridge passively monolithic MLL and an optical microscope image of ridge laser with 2µm width.**

## 3.3 Experimental Techniques and Experimental Set-up

### 3.3.1 Overview of Segmented Contact Method

The segmented contact method, or single-pass measurement, is a technique used to measure the modal gain and absorption directly from the Amplified Spontaneous Emission (ASE) which is emitted from the edge of a multi-segmented device. It is measured as a function of pumped length of a stripe contact, and thus we use a test structure with a stripe contact which is segmented into individual and isolated sections.

Each section is electrically pumped and the amplified light for each section is measured, individually and together. To measure the ASE, the prevention of cavity round trip amplification is essential. Thus, to eliminate the round-trip amplification, the edge of the test structure is cleaved to have angled facets of 10°. In addition to the angled facets, the segments that are close to the rear facet are unpumped or reverse biased to absorb any released photons that may provide an optical feedback. Figure (3.4) illustrates the segmented contact non-lasing device. The ASE per unit length can be measured and hence the gain and absorption will be extracted from ASE spectra (P. Blood, 2015).

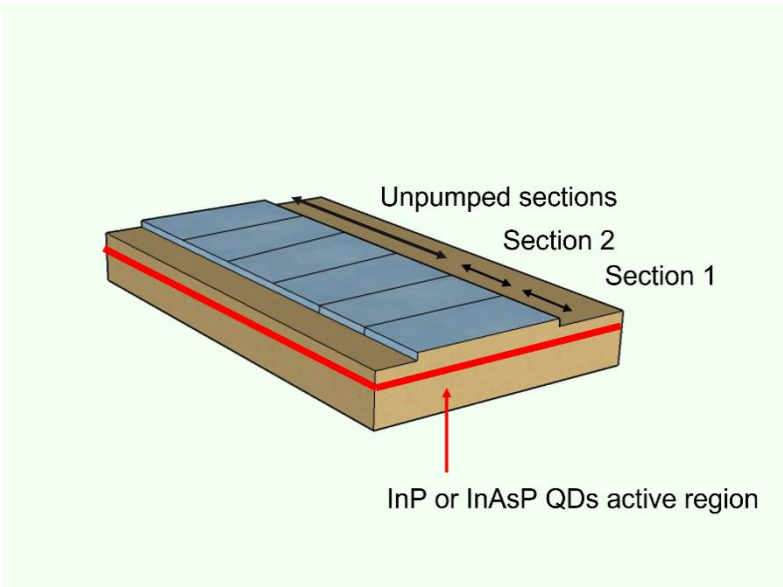


**Figure 3. 4: The design of the segmented contact oxide Laser structure illustrating section 1, section 2 and unpumped sections.**

The electrical excitation of electrons (electrical pumping) rate plays a significant role in the determination of the level of population inversion and hence the gain. When a section is electrically pumped, injected electrons in the p-n junction gain energy and fall from the conduction band into the empty states that created by the injection of holes in the valence band and thus electrons-holes pair recombination occurs. Those electrons-holes pair recombination and disappearance occurs in the active region which is a slab waveguide and the energy of electron-hole pair converts to photons through the disappearance. As long as the photon is propagating along the excited

length section in the presence of the gain, the spontaneous emission will be amplified. The intensity of the light propagates in the guided mode along the propagation direction y-axis is represented by the equation below (P. Blood, 2003),

$$I(y) = ß_{spon}\, R_{spon} \times e^{(G - \alpha_i)y} \qquad (3.1)$$

Where $ß_{spon}$ is the spontaneous emission coupling factor, $R_{spon}$ is the excitation rate of spontaneous emission, G is the modal gain and $\alpha_i$ is the internal optical loss. $R_{spon}$ and G are assumed to be uniform along the excited length (L). So, the result of the integral of equation (3.1) along the excited length is as follows

$$I(L) = \beta_{spon} R_{spon} \times \frac{(\exp(G - \alpha_i)L) - 1}{G - \alpha_i} \qquad (3.2)$$

The measured ASE from two identical sections when it is pumped separately and together can be extracted from equation (3.2) and represented as in the following equations

$$I_{ASE1}(L) = \beta_{spon}\, R_{spon} \times \frac{(\exp(G - \alpha_i)L) - 1}{G - \alpha_i} \qquad (3.3)$$

$$I_{ASE2}(L) = \beta_{spon}\, R_{spon} \times \frac{(e(G - \alpha_i)L) - 1}{G - \alpha_i} (\exp(A + \alpha_i)L) \qquad (3.4)$$

$$I_{ASE12}(L) = \beta_{spon}\, R_{spon} \times \frac{(\exp(G - \alpha_i)2L) - 1}{G - \alpha_i} \qquad (3.5)$$

Where L is the length of the section. When we electrically pump section 2, the ASE that emitted from it will pass through section 1 before it emerges from the facet. As a result, if section 1 is unpumped it will absorb part of the ASE that was emitted from section 2 and so, A in equation (3.4) represents the ASE from section 2 that is absorbed in section 1. Figure (3.6) presents TE polarized ASE of each segment, whether pumped individually or together at driven current of 152 mA and at room temperature. It is clear that the intensity of the two segments is the highest when they are pumped together. The peak of the intensity of Segment 2 has been reduced and shifted to a

longer wavelength due to most of the ASE of Segment 2 being absorbed by Segment 1.

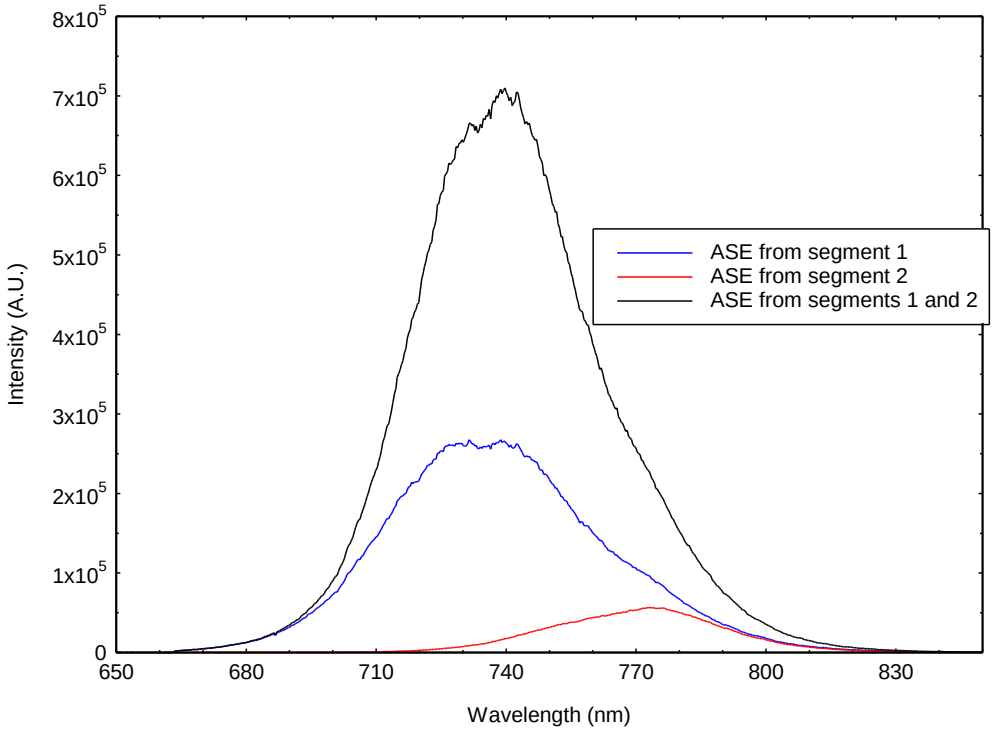


**Figure 3. 5: ASE of pumped Segments 1 and 2, individually and together.**

The calculation of modal gain and absorption can be extracted from ASE spectra. The modal gain is proportional to the ratio of ASE spectra from pumping section 1 and 2 together to the ASE from pumping section 1 with the same current density. Whilst the modal absorption is proportional to the ratio of ASE spectra from pumping section 1 to the ASE from pumping section 2. The net modal gain and absorption in real units ($cm^{-1}$) is obtained from the following two equations

$$G - \alpha_i = \frac{1}{L}\ln\left[\frac{I_{ASE12}}{I_{ASE1}} - 1\right] \tag{3.6}$$

$$A + \alpha_i = \frac{1}{L}\ln\left[\frac{I_{ASE1}}{I_{ASE2}}\right] \tag{3.7}$$

Figure 3.6 displays the net modal gain and absorption calculated from ASE spectra. The internal optical loss is extracted from the long wavelength region where the

absorption and gain curves converge, and it is related to loss associated with the scattering and the free-carriers absorption inside the waveguide. The peak of the gain profile in the x-axis indicates the lasing wavelength at the driven current. The point where the gain curve crosses the dotted line in the short wavelength range is the transparency point.

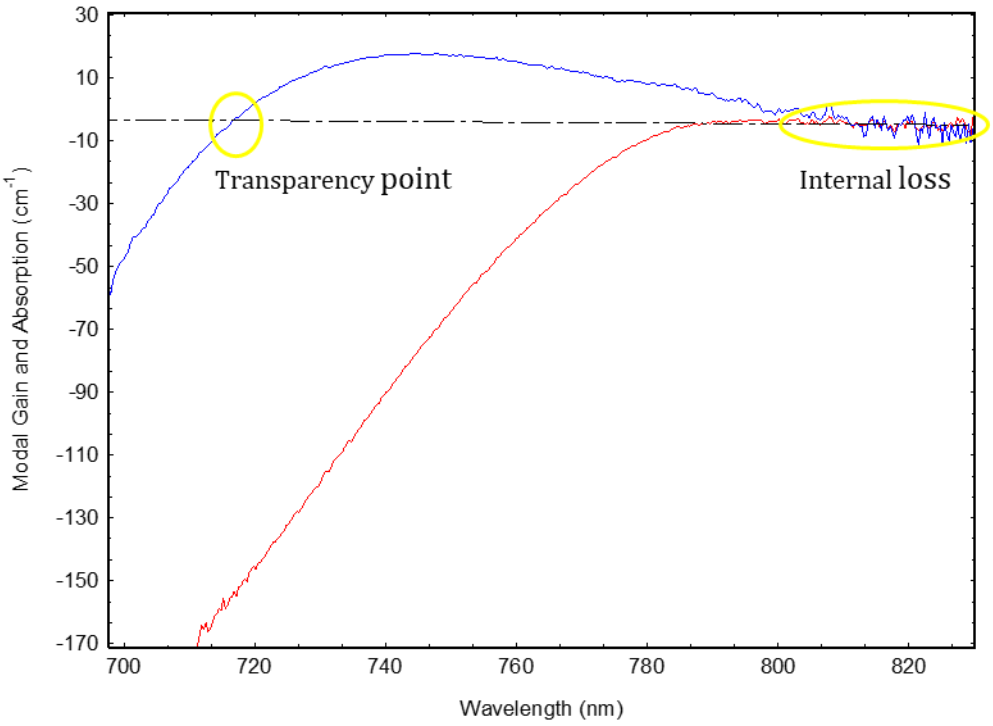


**Figure 3. 6: The modal gain and absorption of InAsP QDs at current of 152mA demonstrating the net gain peak (the maximum gain of blue curve), the transparency point, and the internal loss.**

### 3.3.2 Experimental-Setup of Segmented Contact Method

The sample is placed into an Oxford Instruments cryostat which is then placed at a micro-positioning stage, capable of aligning the sample over 6 degrees of freedom. In this measurement, the operation of the electrical pumping is set to be pulsed with a pulse generator at a repetition rate of 1KHz to eliminate the effects of self-heating. It is important to trigger this current pulse for reducing the noise. To do this, another pulse generator (delay pulse generator) is used to provide a trigger pulse with a gate mode width of 20 ns. The pulses can be monitored using an oscilloscope. The current

pulse should be synchronized with the trigger pulse. A switch box is utilised to pump the two segments individually.

The amplified spontaneous emission that results from pumping the two segments electrically is collected from the facet by a 10X magnification lens into a monochromator slit. Between this monochromator and the lens, a polarizer is placed to select the emission mode—either TE or TM. The monochromator is an MS260TM Imaging 1/4m Spectrograph. The optical configuration for this monochromator is an asymmetrical in-plane Czerny-Turner-type spectrograph. It consists of two toroidal mirrors for producing an accurate image and one grating of 300 lines/mm in order to split the ASE into wavelength spectrum. Measurement of the spectrum has been performed through an ICCD camera which is made up of a charged-coupled device and an intensifier. It used for the purpose of detection, and data is processed via a computer connection (Figure 3.7). The temperature of the sample in the cryostat is controlled using a temperature controller; the temperature is fixed at room temperature (T=294 K) for all experiments that have been made in this thesis.

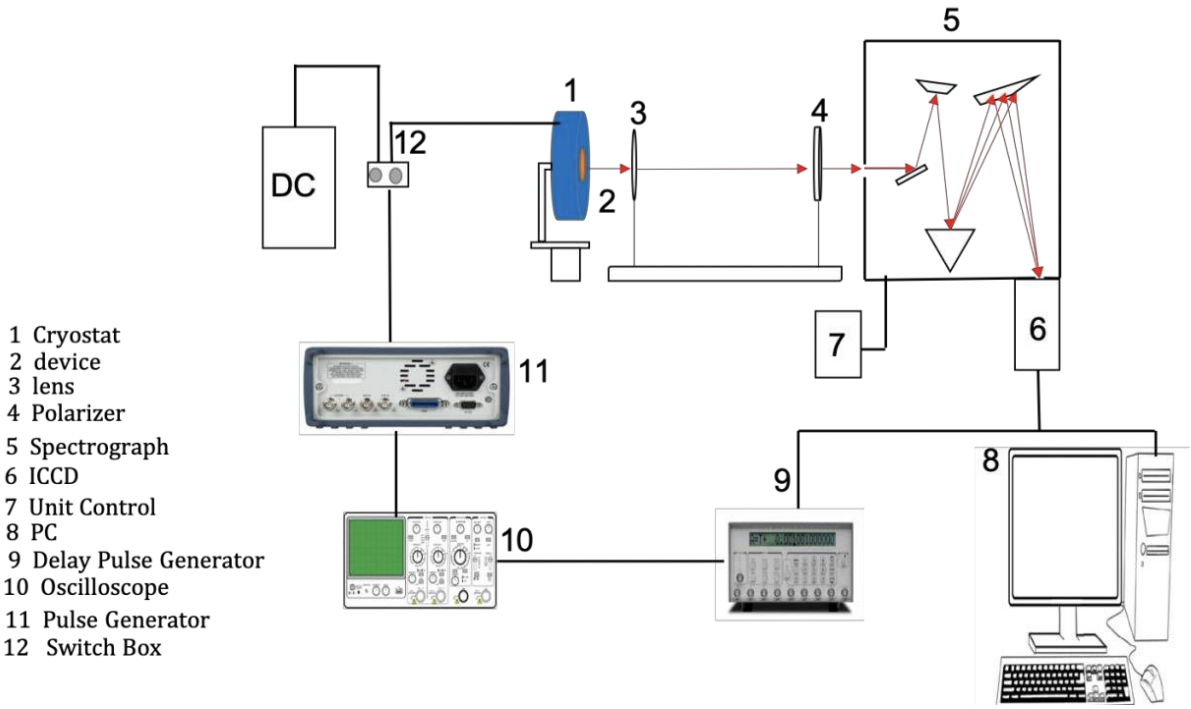


**Figure 3. 7: Schematic Diagram of Experimental setup for measuring ASE from segmented contact non-lasing edge emitting device.**

It is important to test the sample before it is placed into the cryostat in order to obtain accurate results. It should have identical near field (NF) and identical current voltage (IV) characteristics for both sections. In this work, the IV characteristics and NF are checked and illustrated in Figure (3.8) and Figure (3.9), the two segments show identical IV characteristics and identical NF. This means that the amount of current which is driven is the same for both segments. Therefore, this sample can be used to study the gain and absorption characteristics.

Several aspects are essential to the success of the experiment. The two sections must have the same lengths; 300 microns length for each section to avoid gain suppression with longer section and noise with shorter section lengths. The resistance of the inter-contact stripe should be high nearly 200 mΩ in order to prevent any leakage carriers between the two sections and hence affect the accuracy of the results. It is also essential to ground or reverse bias the passive sections by the rear facet, to avoid optical feedback. The slit width also plays an important role in this experiment: should be very narrow to exclude the unamplified light or lights which is partially amplified. Increasing the slit width will allow to this unamplified light to enter the monochromater and thus the detector (ICCD) which result in a reduction in the measured gain.

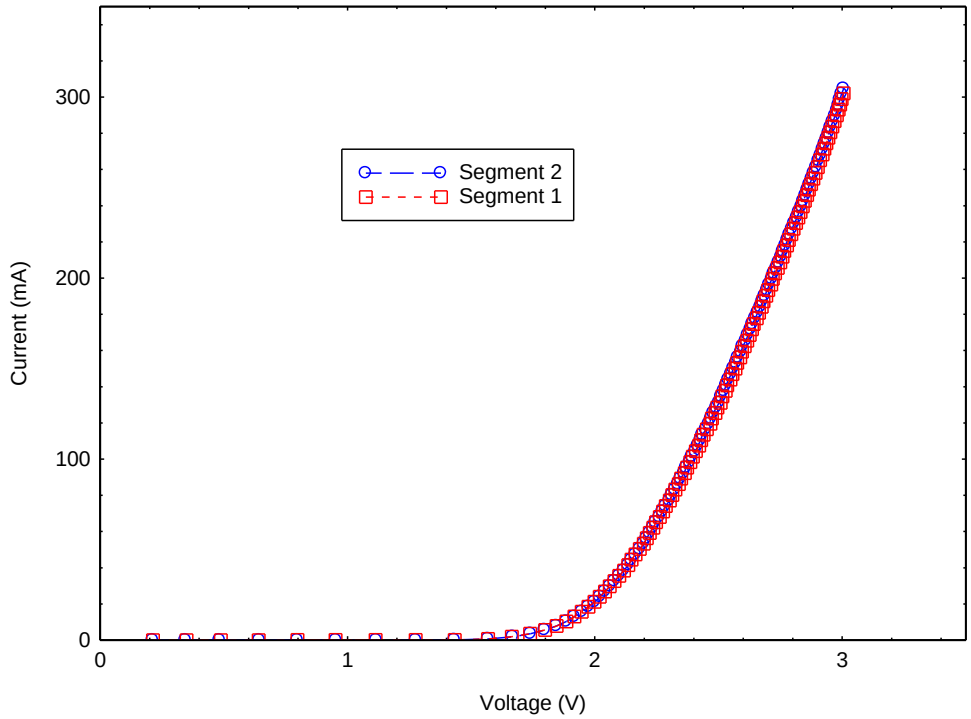


**Figure 3. 8: The IV characteristics of InP QD material of Segments 1 and 2 showing identical IV.**

**Figure 3. 9: The Near Field of InAsP QD multi-section device.**

### 3.3.2 Reverse Bias Measurement

In order to understand the behavior of absorber for any semiconductor material which used in passively monolithic MLLs, the absorption is measured under different reverse bias voltage (0 -6 V). We connect a DC voltage to the segmented contact kit for the purpose of application of reverse bias on the sections. Section 1 is pumped with driven

constant current and at the same time section 2 is reverse biased and hence producing $ASE_1$. $ASE_2$ is produced from pumping section 2 with the same current and reverse biased section 1 with the same voltage. The absorption will be the ratio of the ASE signals 1 and 2 and is directly proportional to the reciprocal length. Increasing the reverse bias applied on one section while pumping the other section with a constant current will tune the absorption peak wavelength toward longer wavelength (Red shift) as seen in Figure 3.10. In contrast, increasing the gain current at fixed reverse voltage will cause a blue shift to the wavelengths.

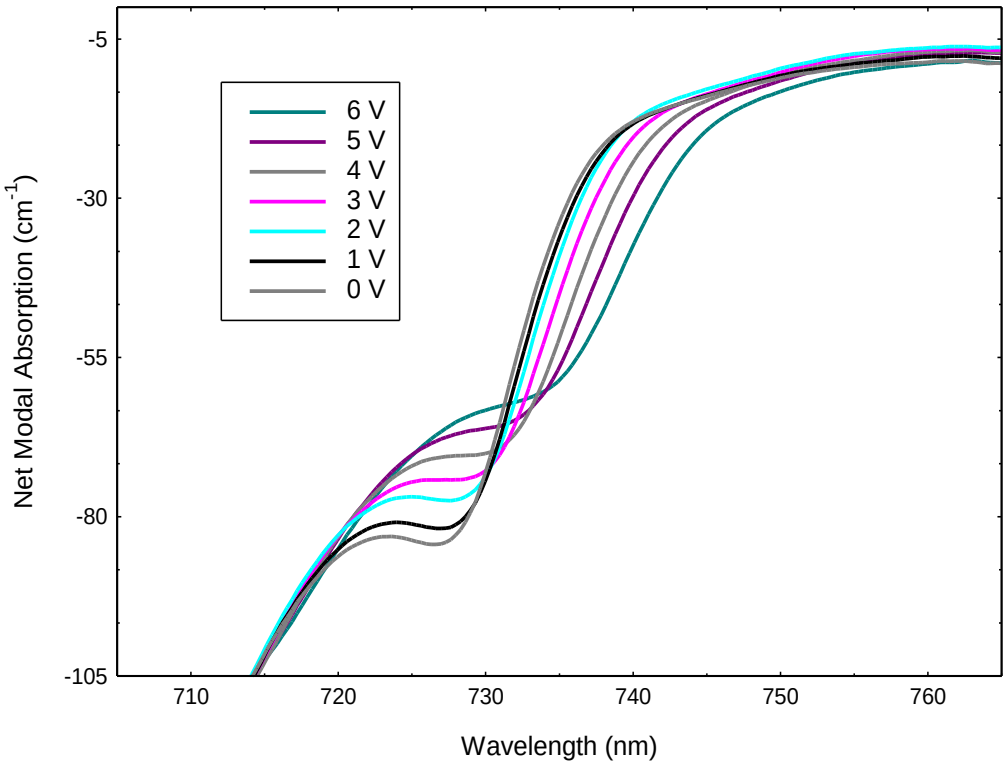


**Figure 3. 10: An example of modal absorption of InP QD material under the influence various reverse bias (0 -6 V) and constant driven current of 50 mA.**

### 3.3.4 Near Field Measurement

The Near Field (NF) is a measurement used for the purpose of imaging the carrier distribution of an optical beam. It provides the spatial intensities profile of light emission that is emitted directly from the facet of laser structure; a multi-section structure in this case. This structure is mounted into cryostat where the temperature is

stabilized by temperature controller and the value of the pulsed current is constant for each section. The ASE coupled by a lens with magnification of 10X, passed through a neutral density filter and collected by a CCD camera. The reason to put a neutral density filter in the path of the light is to reduce the intensity of light and hence, avoid the light saturation. The emitted beam is imaged for pumping section 1 and section 2 independently and from pumping the two sections together with the same driven current. In addition, the current spreading between the device contact and the active region can be known from the half width maximum (FWHM) of the intensity profile of nearfield in Figure 3.10 which provide us the pumped width of the guided light. The intensity profile in pixels due to that we used a standard camera. Calibration was done to convert the pixels numbers into centimeter. The intensity profiles of the three situations are the same which resulted in a good device to provide accurate results.

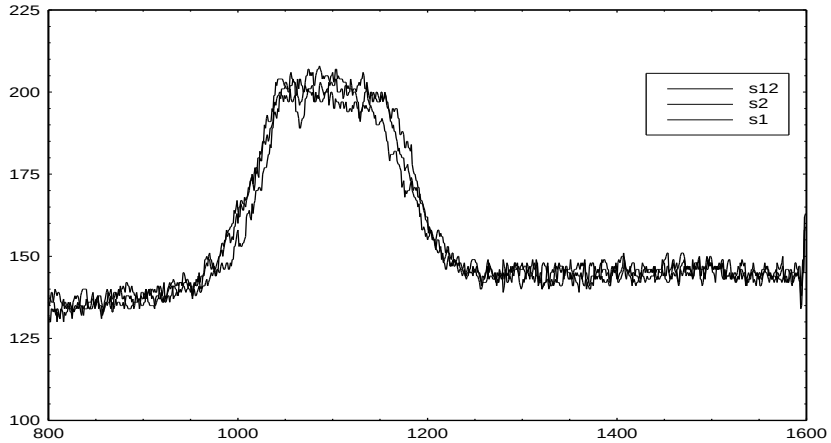


**Figure 3. 11: The optical image of the Nearfield and the intensity profile in pixels of InAsP QD multi-section device at current of 152 mA, showing identical NF for all sections which means same carrier distribution, that creates the optical beam emitted from section 1, section 2 and section 12.**

## 3.4 Summary

In this chapter, the epitaxial structures of the devices used in this study, the experimental techniques and set-up were provided. The contact stripe is used in multi section non-lasing devices and fabricated ridge mode-locked lasers (MLL) were briefly discussed. The SCM was described in detail. The chapter also covered the measurement of modal absorption under the reverse bias and the Near-field measurements.

## References

Smowton, P. M. Lutti, J. Lewis, G. M. Krysa, A. B. Roberts, J. S. and Houston, P. A. (2005), "InP-GaInP quantum-dot lasers emitting between 690-750 nm," *IEEE Journal of Selected Topics in Quantum Electronics*, vol. 11, no. 5, pp. 1035-1040, doi: 10.1109/JSTQE.2005.853838.

Smowton, P. M. Al-Ghamdi, Shutts, S. Edwards, G. Hutchings, M. and Krysa, A. B. (2010) "Effect of Growth Temperature on InP QD Lasers," *IEEE Photonics Technology Letters*, vol. 22, no. 2, pp. 88-90, doi:10.1109/LPT..2036245.

Elliott, S. N., Smowton, P. M., Krysa, A. B., & Beanland, R. (2012). The effect of strained confinement layers in InP self-assembled quantum dot material. *Semiconductor Science and Technology*, *27*(9), 094008.

Karomi, I., Smowton, P. M., Shutts, S., Krysa, A. B., & Beanland, R. (2015). InAsP quantum dot lasers grown by MOVPE. *Optics Express*, 23(21), 27282-27291

Blood, P. (2015). Quantum Confined Laser Devices: Optical gain and recombination in semiconductors. Oxford: Oxford University Press.

Blood, P., Lewis, G. M., Smowton, P. M., Summers, H., Thomson, J., & Lutti, J. (2003). Characterization of semiconductor laser gain media by the segmented contact method. *IEEE Journal of Selected Topics in Quantum Electronics*, 9(5), 1275-1282

A. B. Krysa et al., (2016) "Growth and characterisation of InAsP/AlGaInP QD laser structures," Compound Semiconductor Week (CSW) [Includes 28th International Conference on Indium Phosphide & Related Materials (IPRM) & 43rd International Symposium on Compound Semiconductors (ISCS), Toyama, pp. 1-2, doi: 10.1109/ICIPRM.2016.7528566.

Agrawal, G. P., & Dutta, N. K. (2013). Semiconductor lasers. Springer Science & Business Media. Berlin, Germany.

# Chapter 4:

# Materials Characterisation: InP and InAs

## 4.1 Introduction

In this chapter, the key properties of InP and InAsP self-assembled QD semiconductor materials are examined for the purpose of checking their eligibility for mode-locking operation. The primary objective of this chapter is to study the gain characteristics under forward bias and the absorber characteristics under reverse bias of both materials. The modal gain and modal absorption of both QDs materials have been measured using the Segmented Contact Method (SCM) that was described in Chapter 3, Section (3.3.1). It has been measured at room temperature and for different injected current density. The spectral bandwidth of both materials at the same conditions have been identified. The comparison of the gain current relation has been investigated and the mode-locked laser condition has been examined from analysis of the gain-current curves. The spectral wavelength ranges of both materials are reported as well as the gain amplitudes as a function of different electrical-pumping rate. The primary part of this chapter is to investigate the influence of reverse bias on the absorption spectrum by measuring the modal absorption that described in chapter 3, section (3.3.3). This investigation reviews some phenomena behind the different behaviour of those materials and reveals the extent of wavelength tuning under forward and reverse bias conditions. All measurements in this chapter use edge-emitting non-lasing segmented contact devices with an oxide stripe broad area contact.

## 4.2 Modal absorption of the InP and InAsP materials

The modal absorption of both QDs materials InP and InAsP has been measured by the SCM which was described in chapter 3, Section (3.3.2) at room temperature. Figure (4.1) shows the positive modal absorption which determines the absorption bandwidth of the materials; available transitions between the valence band and the conduction band in the semiconductor material. The absorption bandwidth ranges are extended from 665 nm to 730 nm for InP QDs and from 670 nm to 773 nm for InAsP QDs. It is clear in Figure (4.1) that the absorption spectra of the InAsP QD material is much smoother and with much less pronounced features or peaks that clearly originate from GS or ES transitions, as in the absorption of InP QDs. The flat region of the absorption curves at longer wavelengths represents the internal optical loss and the absorption peak at shorter wavelengths, as indicated in the left (short wavelength) side of graph, results from the carrier exchange between the dots and the QW like layer. This QW layer expands the absorption bandwidth.

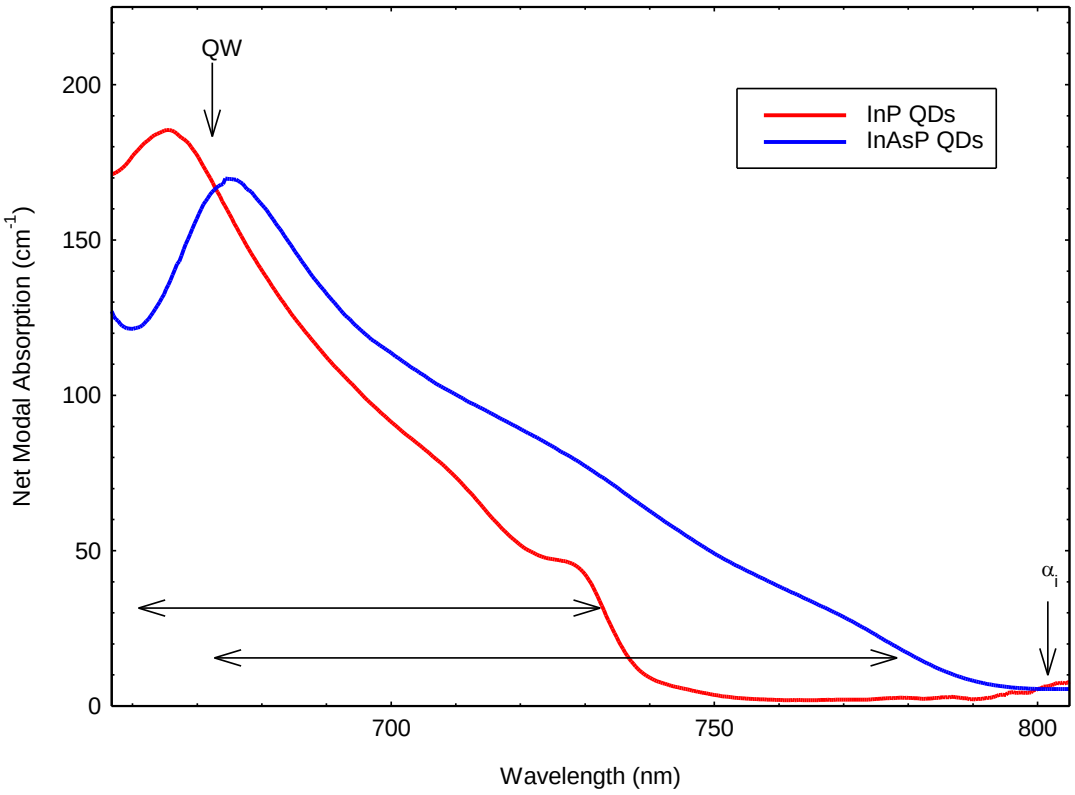


**Figure 4. 1: the positive modal absorption of InP QDs (red) and InAsP QDs (blue).**

The reason of the smooth absorption (no defined peaks) curve behaviour of InAsP QDs and more defined GS and ES peaks in the absorption spectrum of InP QDs is attributed to the degree of inhomogeneous broadening or inhomogeneous size dots distributions. The nonuniformity and great degree of the InAsP dots sizes distributions led to smooth absorption spectrum whereases the uniformity and less inhomogeneous size dots distributions of InP material led to absorption spectrum with clear and more defined GS and ES peaks. It was clear in the TEM images of both materials (that mentioned in Chapter 3, Section 3.2) the nonuniformity of small InAsP dots distribution and uniform distribution of small and large InP dots material. The large lattice mismatch between the InAsP QDs and the GaAs substrate approximately 7%, led to a great degree of dots sizes distributions (krysa, et al., 2016). This great variation of dots diameters resulted in smooth absorption spectrum. In contrast, InP QDs has more uniform distribution of dots sizes and less inhomogeneous broadening, led to more defined peaks ground states (GS) of small-size and large-size dots and excited states (ES) of Large-size dots.

The inhomogeneous size distribution of QD materials can be represented by the Bimodal size distribution as reported in literature (Al-Ghamdi et al., 2011; Porsche et al., 2000; Schulz et al., 2009). To incorporate this explanation with substance in order to simplify a quantitative understanding of the absorption data, the absorption spectra in energy are estimated and fitted to Gaussian distributions in Figure 4.2 for InP QDs and Figure 4.3 for InAsP QDs using the parameters that are listed in Tables 4.1 and 4.2. Figure 4.2 shows the Gaussian fit of three estimated absorption peaks of InP QDs : GS of small dots, GS of large dot and ES of large dot. Figure 4.3 illustrates the Gaussian fit of two estimated absorption peaks of InP QDs: GS of two different in size dots considered to be in the small range based on the TEM images that illustrated in Chapter 3, section (3.3.3). For simplicity, we have considered that there are only two different size InAsP dots in the small range. The area underneath the ES peak of large InP dot is constrained to be the double of area of the GS peak of the same dot based on the predications of energy levels of a harmonic oscillator where there is a fixed relation ruled the allowed energy levels/energy eigenvalue (Park et al., 1998). Other variables as GS absorption amplitude for small and large dots, the energy position and

the width of Gaussian curve were free to be determined as well as the same variables of ES of InP large dot as there are no rules governed it.

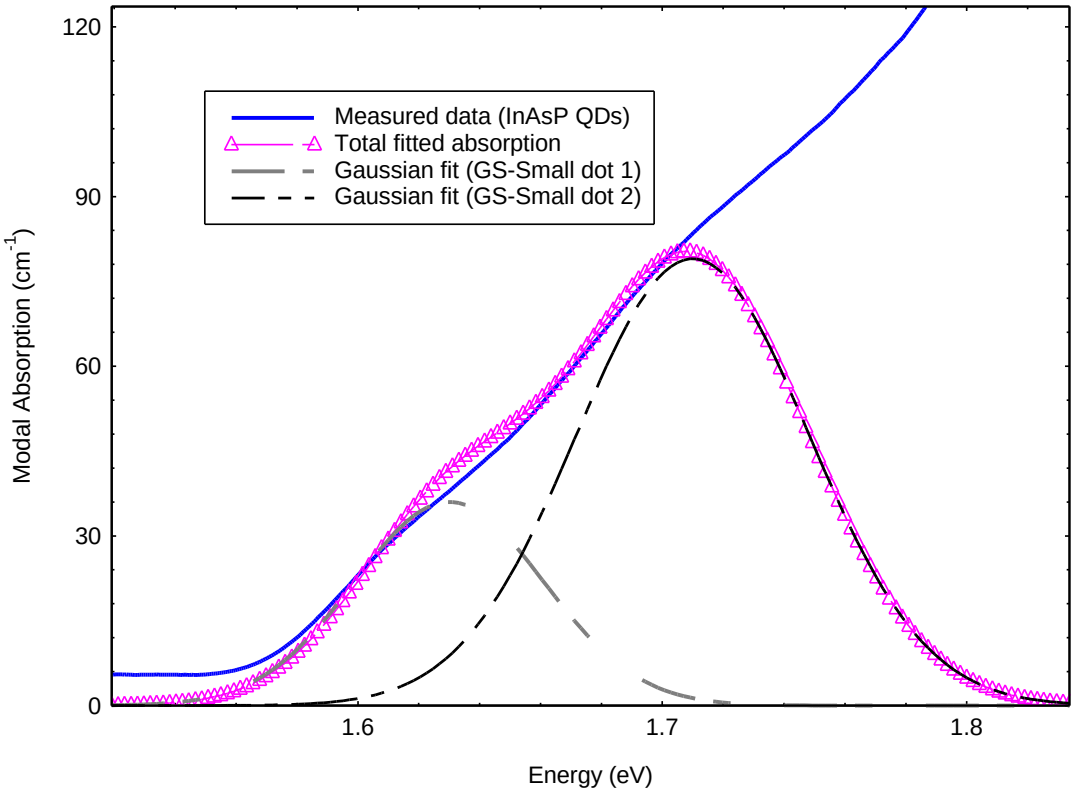


**Figure 4. 2: Gaussian fit of GS-small dot 1 and GS-small dot 2 of InAsP QDs positive modal absorption.**

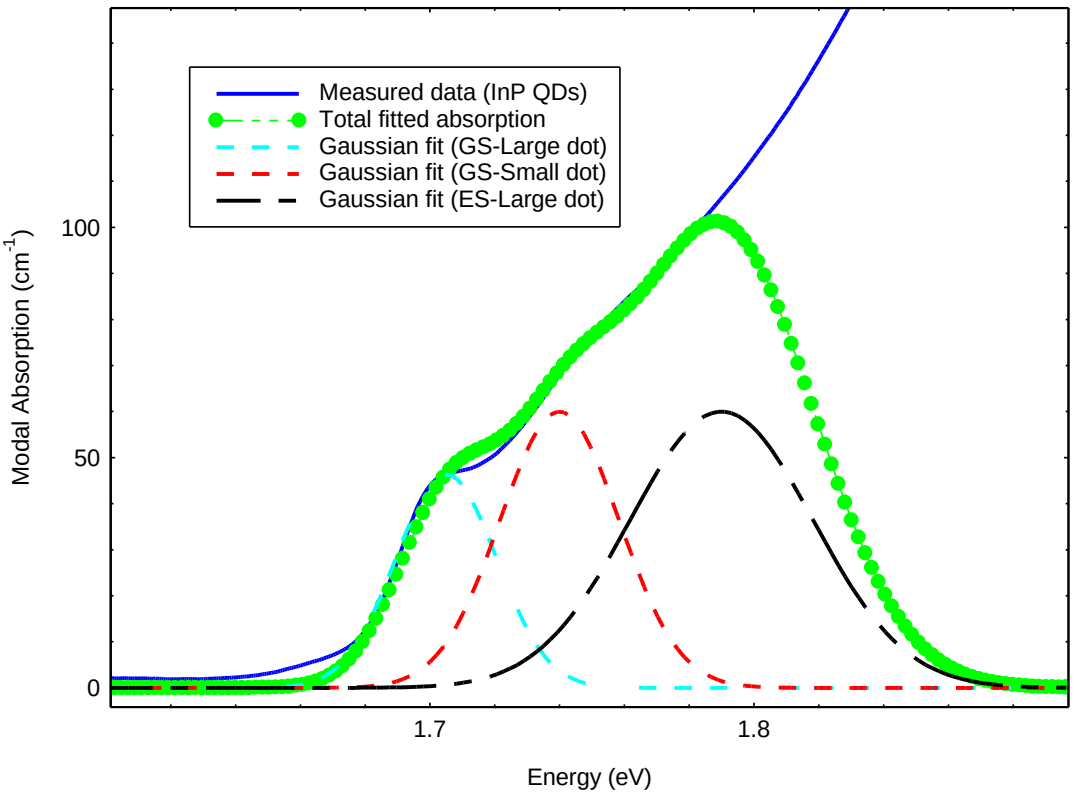


**Figure 4. 3: Gaussian fit of GS-large dot, GS-small dot and ES-large dot of InP QDs positive modal absorption.**

**Table 4. 1: A list of parameters that were used to fit the Gaussian distributions of InAsP QDs.**

| State | Amplitude ($cm^{-1}$) | Peak position (eV) | Standard deviation ( eV ) |
|---|---|---|---|
| **GS- small dot 1** | 27 | 1.63 | 0.022 |
| **GS- small dot 2** | 79.8 | 1.70 | 0.027 |

**Table 4. 2: a list of parameters that were used to fit the Gaussian distributions of InP QDs.**

| State | Amplitude ($cm^{-1}$) | Peak position (eV ) | Standard deviation (eV ) |
|---|---|---|---|
| **GS-Large dot** | 46.4 | 1.71 | 0.011 |
| **GS-small dot** | 60 | 1.74 | 0.013 |
| **ES-Large dot** | 51 | 1.79 | 0.02 |

## 4.3 Influences of reverse bias on modal absorption

The influences of applying reverse bias on the absorption spectrum are investigated to understand the behaviour of the material absorber. Figure 4.4 illustrates the influence of applying reverse bias in the range of (0- 6 V) on the absorption spectra for InP QDs and Figure 4.5 for InAsP QDs. The absorption spectrum has been measured by SCM

as described in Chapter 3, Section 3.3.3. The behaviour of ground states peaks of InP QDs absorption spectrum (see Figure 4.4) is more defined and high absorption is present when the bias is zero. Applying a reverse bias causes a red-shift in the absorption curve, this shift increases in line with an increase in the reverse bias. The red-shift in wavelength is related to QCSE phenomena that described in Chapter 2, Section 2.5. The absorption peak reduces as the increase of the reverse bias and gets broader due to the reduction of the integral overlap of the electron and hole wavefunctions and thus affect the oscillator strength. At a specific absorption point, the wavelength of InP QDs have tuned from 728 nm at zero bias to 735 nm at 6 V, whereas InAsP QDs tunning range from 773 nm to 781.8 nm at the same reverse bias conditions. The absorption peak amplitude of InP is changing with reverse voltage whereases it is constant for InAsP due to the fact that the reverse bias increases the overlap between the energy states of GS of InP large and small dots. The band gap of both materials reduces as the increase of reverse bias and this cause the wavelength redshifts. Due to the small physical size (small height) of the InAsP dots, we can only see a limited red-shift or stark-shift range. In other words, any added new carriers to InAsP dots will not contribute to the absorption; it will escape to the wetting layer due to the small height of dots as it is clear at the shorter wavelength of absorption in Figure 4.5.

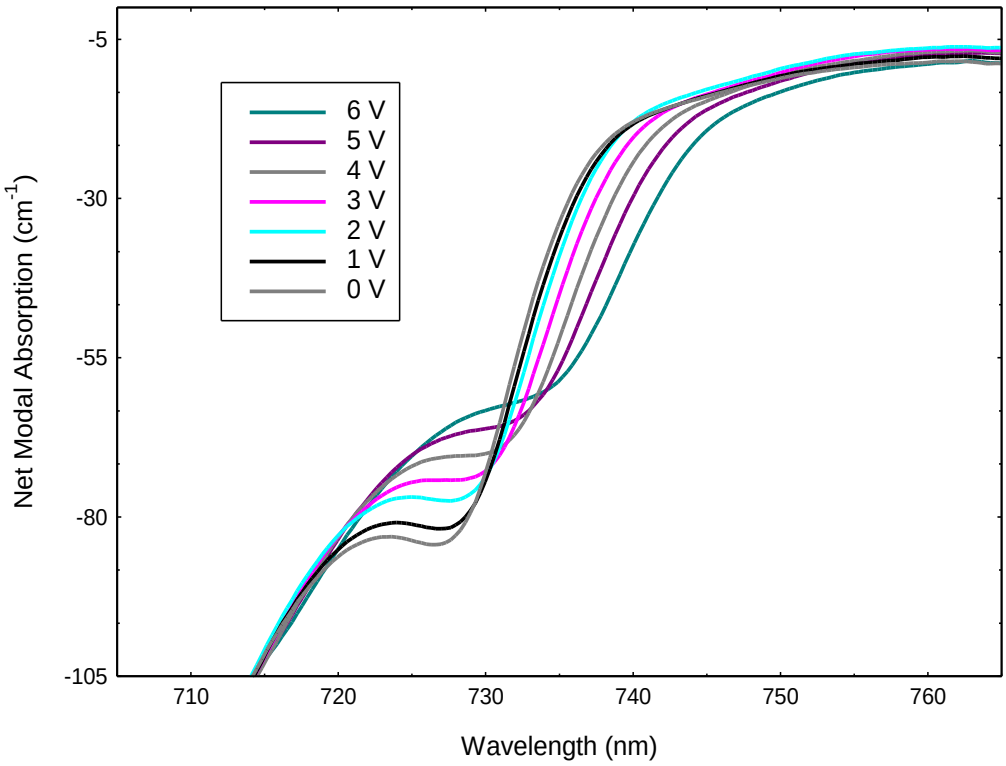


**Figure 4. 4: Influence of applied reverse bias on the absorption spectrum of InP QDs when the gain section is pumped with fixed gain-section current density.**

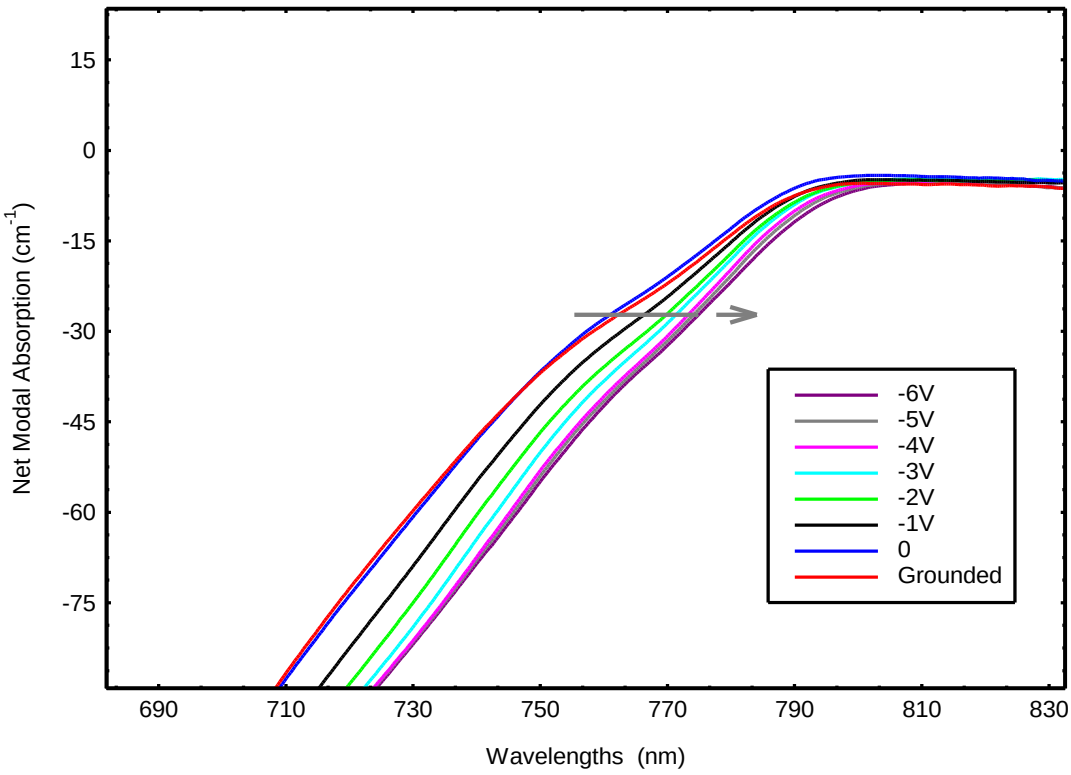


**Figure 4. 5: Influence of applied reverse bias on the absorption spectrum of InAsP QDs when the gain section is pumped with fixed gain-section current density.**

Figure 4.6 displays the red-shift of absorption peak wavelength for both studied QDs materials at different amount of reverse bias ranging from 0 to 6 V. The application of the reverse bias causes a linear change of the absorption wavelength in both materials. The estimated wavelength peaks are plotted in the two figures with a linear regression curve fit in order to calculate the rate of change in wavelength per voltage. The measured rate of shifts is nearly 2±0.1 nm/V and 1±0.1 nm/V, resulting in a total shift of 7nm and 9nm in the range (0- 6V) for both QDs materials InP and InAsP, respectively. The red-shift of InAsP absorption suppressed at high reverse bias (4 V-6 V) and the shift rate changed to nearly 1 nm/V. The reason of this suppressing might be related to the tunnelling of carriers due to the small barrier hight of InAsP dots compared to InP dot (details of sizes of InAsP and InP QDs are mentioned in Chapter 3, Section 3.2). The red-shift suppression in InAsP dots will limit the absorber compression parameter which is responsible of shortening mechanism of ML pulses (Rafailov & Avrutin, 2013).

An interesting observation can be made from this investigation is that the red-shift could be limited by the dot size. Therefore, the improvement of the QD growth is critical to optimise them for mode-locking devices for expanding the wavelength tuneability ranges at different driving bias condition.

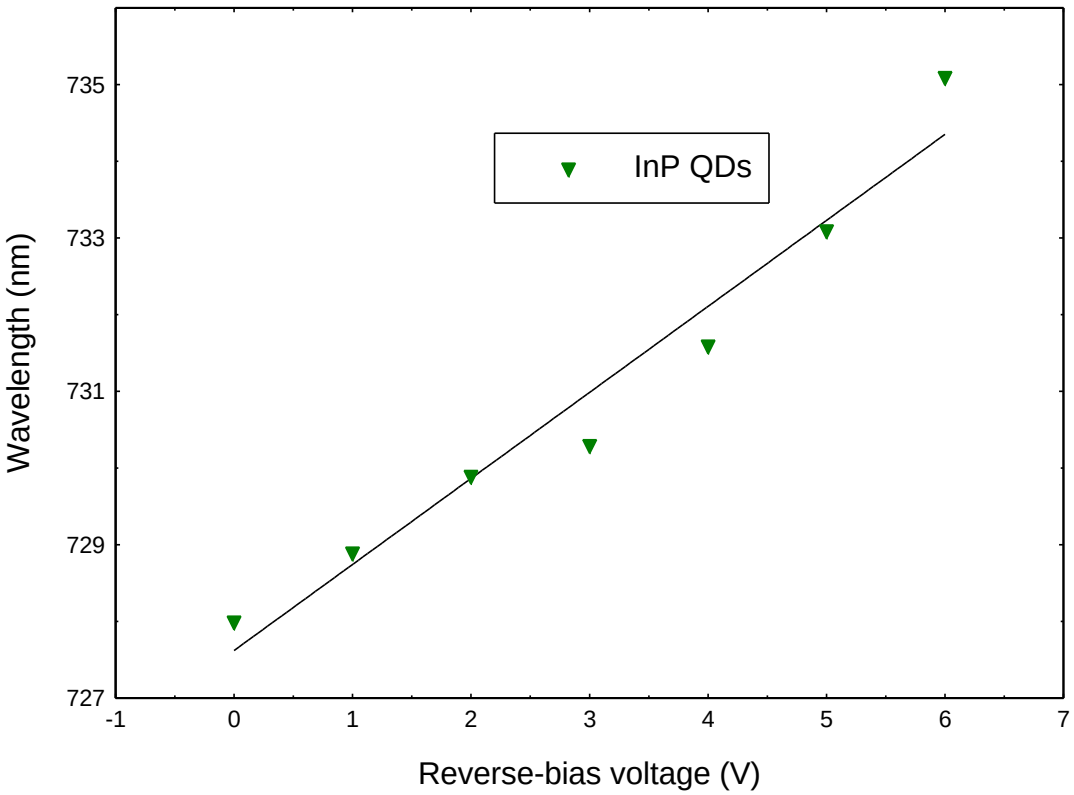


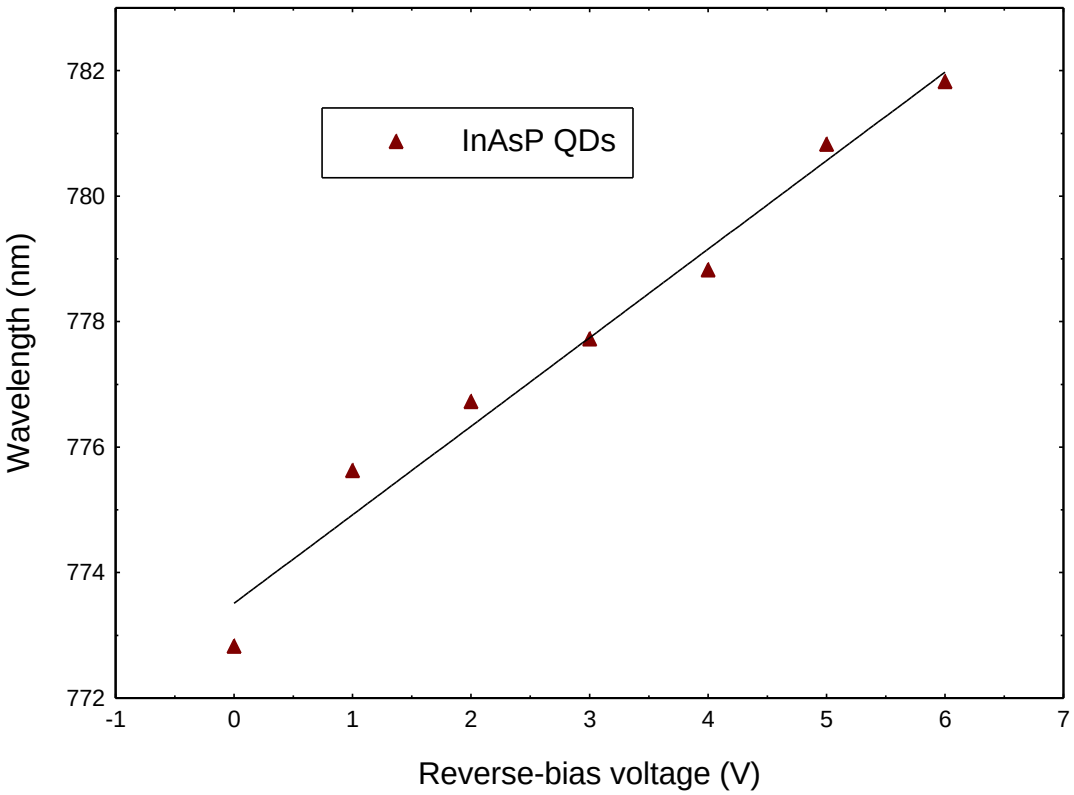


**Figure 4. 6: the red-shifts of peak absorption wavelength at different reverse bias conditions of InP QDs (top) and InAsP QDs (bottom).**

## 4.4 Modal gain of InP and InAsP QDs semiconductor materials

The characteristics of the absorber-section under reverse bias of InP and InAsP QDs materials, for the purpose of understanding the performance of passively monolithic MLLs, have studied in the beginning of this chapter. Here in this section, the characteristics of gain section under different current density have been investigated.

The net modal gain and absorption (see Figure 4.7) of InP QDs material are obtained and measured at current densitiy varying from approximately 300 A.cm$^{-2}$ to 1800 A.cm$^{-2}$ at room temperature. In addition to InP QDs, the net modal gain and net modal absorption of InAsP QDs material (see Figure 4.8) at current density ranging from approximately 95 A.cm$^{-2}$ to 1667 A.cm$^{-2}$ are also measured and at room temperature. These measurements have been done by the SCM which described in (Chapter 3, section 3.3.1). Significant parameters can be extracted from the net modal gain and net modal absorption such as gain bandwidth, internal optical loss, gain amplitudes and wavelength ranges at various injected current density. The internal optical loss due to the free-carrier absorption or the scattering inside the waveguide can be obtained from the long wavelength region beyond the band edge of the gain and absorption curve. It is nearly $5\pm1$ cm$^{-1}$ for InP QDs and $2\pm1$ cm$^{-1}$ for InAsP QDs. The higher loss of InP QDs might be attributed to the existence of the large dot in InP material (Al-Ghamdi et al. 2011). The peak modal gain increases with increasing injected current density due to state filling of energy states. The gain peaks saturate at nearly 17 cm$^{-1}$ of InP QDs at the highest injected current density. The same scenario occurs with InAsP QDs, but the gain peaks saturate at nearly 13 cm$^{-1}$. The gain peak saturated at lower gain peak compared to InP QDs due to the high degree of dot sizes distributions of this structure. The gain saturation in both materials is due to the depletion of population inversion that caused by stimulated recombination (Peter Blood 2015). This resulted in a finite gain bandwidth that was considerably narrower than the absorption bandwidth.

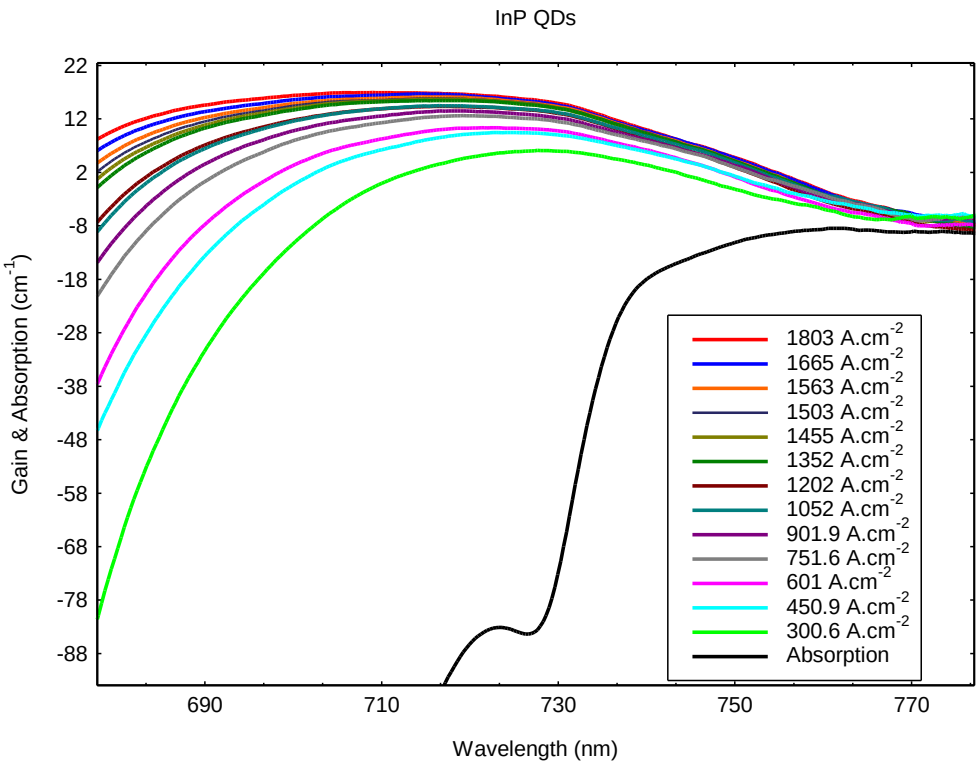


**Figure 4. 7: the net modal gain of InP QDs materials as a function of current density.**

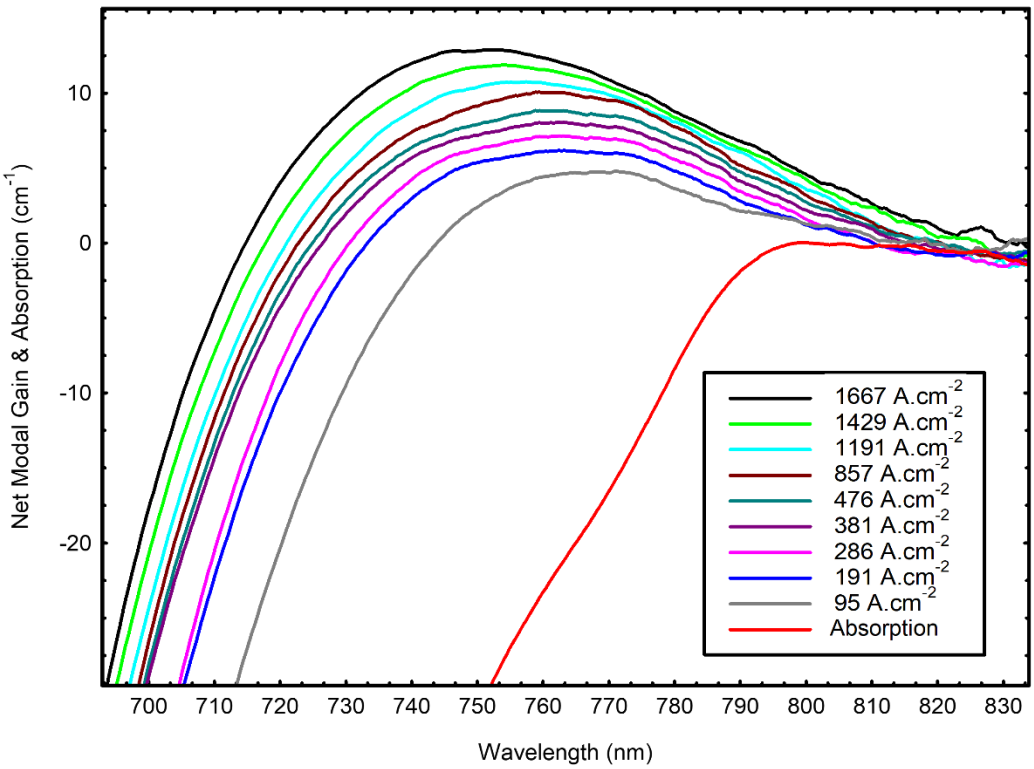


**Figure 4. 8: The modal gain of InAsP QDs materials at different pumping rate.**

Figure 4.9 plots the wavelength peak of InP and InAsP QDs materials as a function of current density (forward bias). As the current density increases, the wavelength is shifted toward longer wavelength (blue-shift) due to filling states of lower energy level and recombination started at high levels. The wavelength of peak modal gain of InP QDs shifted toward shorter wavelength from 729 nm at J = 300 $A.cm^{-2}$ to 709 nm at J = 1800 $A.cm^{-2}$ due to the filling of the lower energy states. The gain peak wavelength of InAsP QDs blue-shifted from 770nm at J= 95 $A.cm^{-2}$ to 745nm at J=1667 $A.cm^{-2}$. A sign of the gain saturation is clear at the graphs in Figure 4.9 at the range of current density between 1000 to 1300 $A.cm^{-2}$ for InP QDs and 900 to 1600 $A.cm^{-2}$ for InAsP QDs. We believe that it is related to the gain saturation of the GS of the large size InP dot and GS of small InAsP dots; lower energy states in general. The rate of the change in blue-shift divided into two regions for both studied materials. The first region is the gradient of the change at injected low current density and the second region is the gradient at high injected current density. The rate of blue shift in the lower current density is greater than the second gradient in case of InAsP dots material. In case of InP QDs, the rate of change continues to rise and this attributed to the existence of large size dots where there are GS and ES transitions. The existence of GS and ES in InP QDs could be beneficial in dual-wavelength or harmonic mode-locking in one device (Sobiesierski & Smowton, 2011). In both studied materials, the blue-shift rate is the highest at lower injected current density. At the high injected current density, the blue-shift rate changes slowly in the case of InAsP whereases it saturates first and then continue to increase steeply in case of InP. This could be attributed to the size of the dots; small dots saturate faster than large dots.

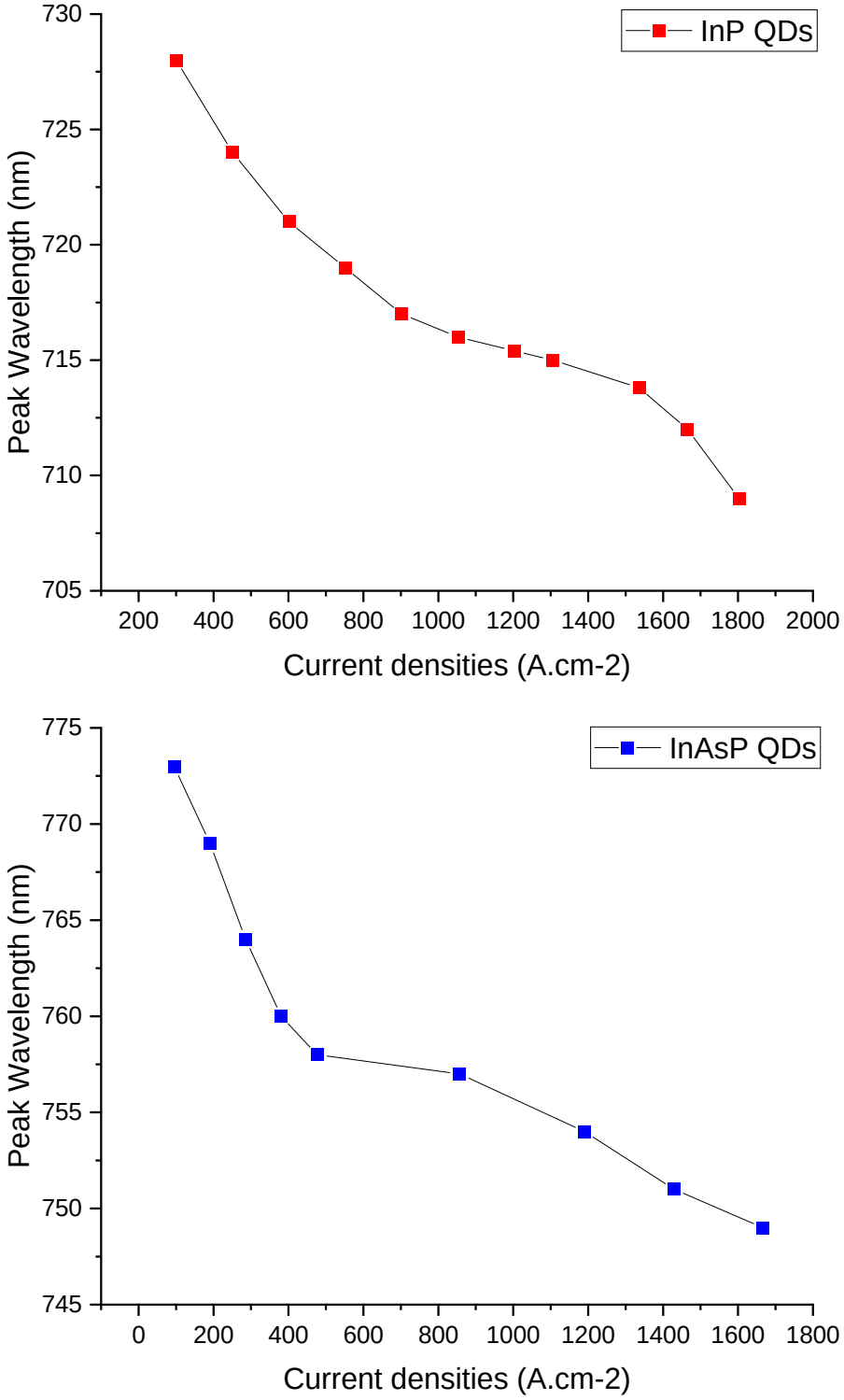


**Figure 4. 9: the blue-shift of InP (upper) InAsP (lower) QDs materials as a function of current density.**

The gain bandwidth of both QDs material are relatively broad, with Full width at Half-Maximum (FWHM) approximately 24 nm for InP QDs and 36 nm for InAsP QDs at wavelength peaks 728 nm and 770 nm, respectively. The rationale behind this broad bandwidth is associated to the inhomogeneous broadening due to the fluctuation of the dot sizes of these structures. FWHM broadens with the increases of injection level. InAsP QDs has wider FWHM than InP QDs due to the high degree of dots sizes inhomogeneity resulting in more broadening as being clear in the TEM images (see Chapter 3, Section 3.2). This broad optical gain feature is promising for generating ultrashort pulses for mode locking as mentioned Chapter 1. However, high level of inhomogeneous broadening will cause low level of gain amplitude and this is the case in InAsP QDs, have wider gain bandwidth and lower gain amplitude compared to InP QDs as illustrated in Figure 4.10. This figure plots a comparison of the gain of the InP and InAsP QDs at the same injected current 125 mA. InP has higher gain nearly 11 $cm^{-1}$ with narrower FWHM of 39 nm whereas InAsP has lower gain approximately 9 $cm^{-1}$ with broader FWHM of 53 nm.

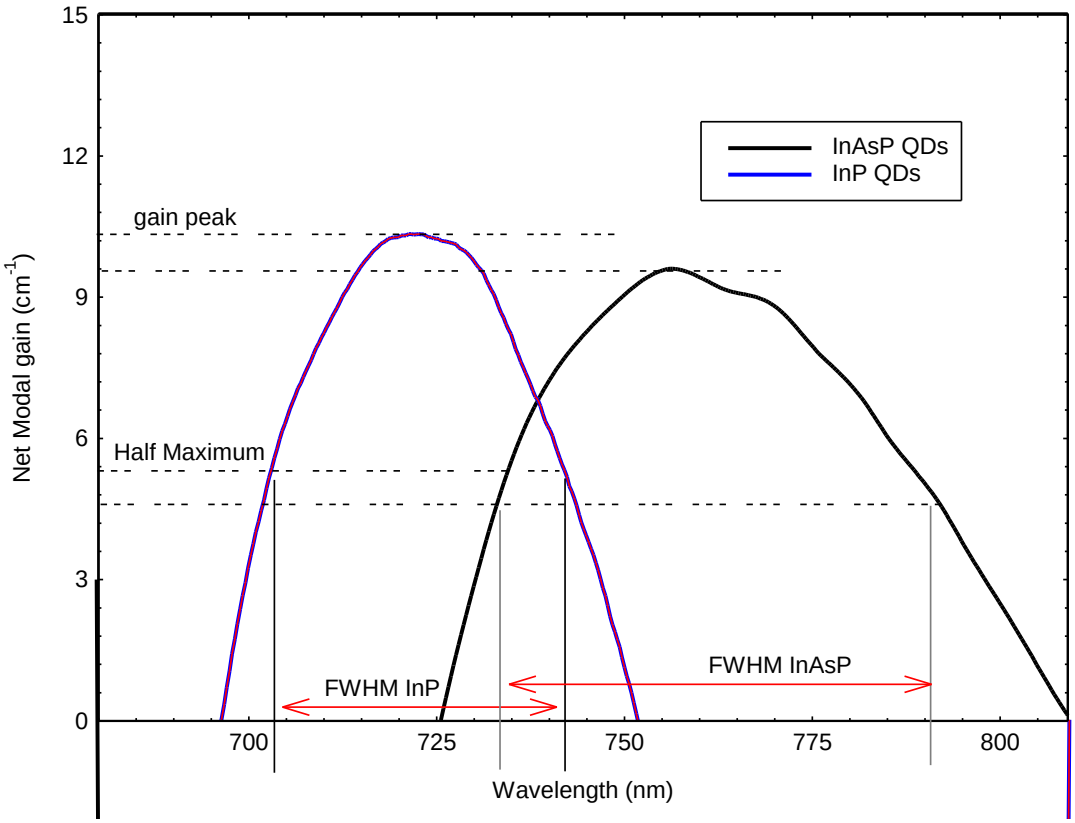


**Figure 4. 10: comparison of FWHM of InP QDs (blue) InAsP QDs (black) materials at the same injected current 100 mA.**

Figure 4.11 displays the gain amplitude and FWHM as a function of current density for both materials. This provides detail about the maximum gain can be achieved from those QDs materials and the wavelength ranges. Both parameters increase as the injection level increases. The gain amplitude increases faster than the FWHM in case of InP, whereas FWHM increases much faster than gain amplitude in case of InAsP. Again, we believe that this is related to the distribution of the dot sizes or the shape of dot. The high degree of inhomogeneity of dots size distribution of InAsP QDs broaden the FWHM whereases the uniform distribution of InP dots increases the gain amplitude. As the increase of the current injection level in case of InAsP QDs material, we think that new energy transitions will be added to the broadening. This attributed to the shape of the dots, the dot height and diameter. It has been reported that the decrease of the dot height will result in strong quantum confinement and thus an increase in the splitting of energy levels (Williamson 2002). This leading us to conclude that the increase of the degeneracy levels causes an increase in the FWHM of InAsP dots. InP dots have less degeneracy level due to the greater height of the dot.

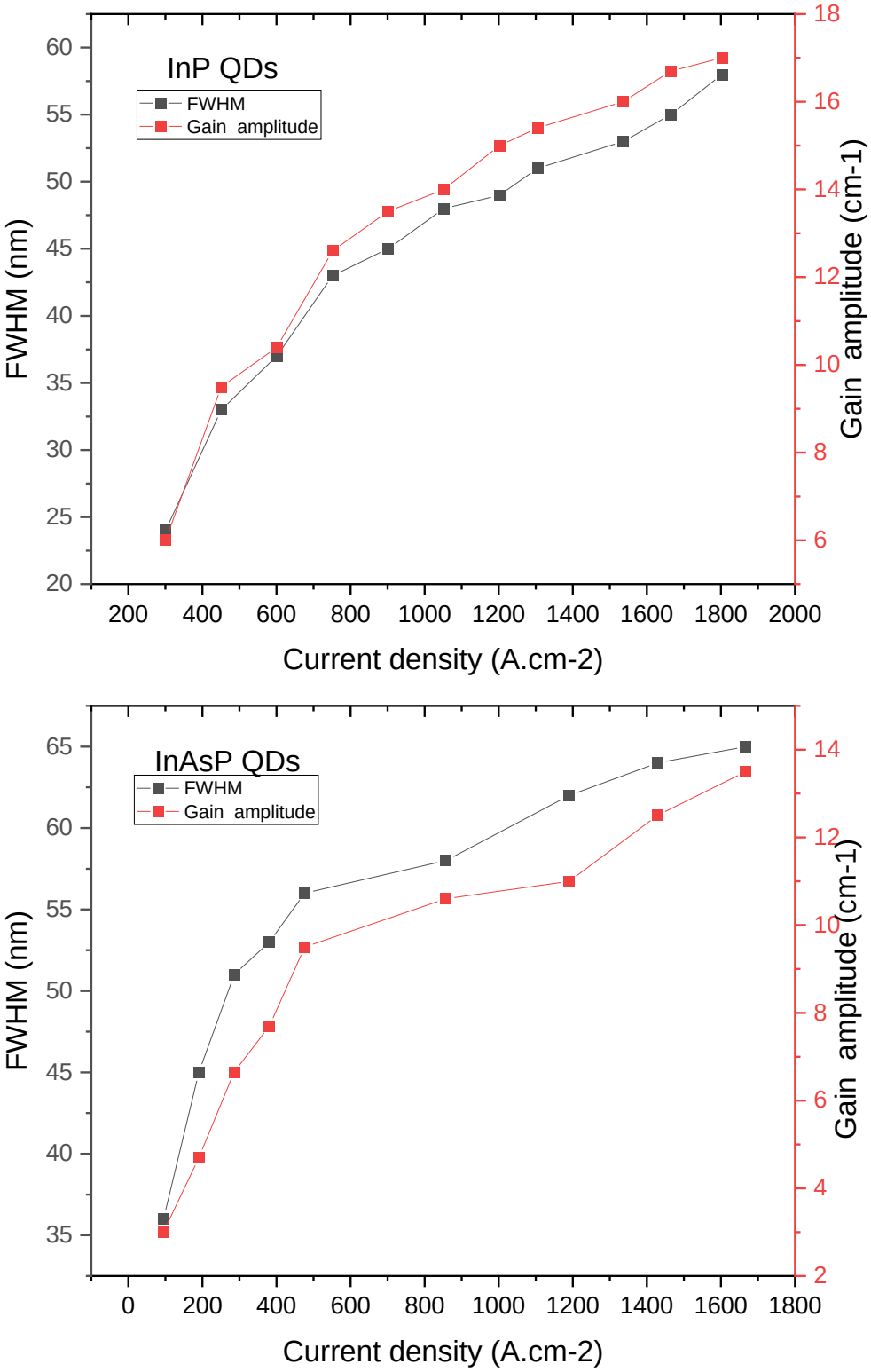


**Figure 4. 11: the gain amplitude and FWHM of InP (upper) InAsP (lower) QDs materials as a function of current density.**

In short, InAsP QDs are more broadband and InP QDs have higher gain, leading to the predictions of the possibility of achieving Mode-locking pulses from InP QDs at lower pumping rate, but wider pulse width compared to InAsP QDs .

## 4.5 Gain- Current Relation

The gain-current relation is a plot of gain peaks that extracted from the net modal gain curves presented in Figures 4.11 and 4.12 as a function of current density. This relation identifies numerous parameters that can be calculated, including threshold current density, transparency current density, differential gain and differential loss and the latter establish the requirement for mode-locking regime. Figure 4.11 presents the gain peaks extracted from the gain measurement as a function of current density of InP QDs and Figure 4.12 illustrates the gain peaks versus current density of the InAsP QDs. The peaks fitted to a QD non-linear curve using Equation (2.8) in Chapter 2. The gain peaks increases rapidly at the low level of current injection and start to increase more slowly and eventually saturate at high level of injection. The same scenario occurs for both studied materials.

It is known that the cavity length has a major effect on MLL devices in term of repetition rate. So, it is important to investigate the parameters that may change as the cavity length vary by the use of gain data. It is important to study the threshold current density for various cavity lengths. From the laser condition Equation 2.6 that mentioned in Chapter 2, the gain threshold of 2 mm, 3 mm, and 4 mm cleaved laser, where the reflectively of the cleaved facet are 0.33, are 6 $cm^{-1}$, 4 $cm^{-1}$ and 2.4 $cm^{-1}$ respectively. The threshold gain is reduced with the increase of the cavity length and this reduction is due to the decrease of internal optical loss with the increase of the cavity length and thus the threshold current decreases as well. In addition, the wavelength will be slightly tuned with changing the cavity length. This information is required to optimise a Mode-Locking device for a specific application. The values that correspond to the threshold gain on the curve is the threshold current density is listed in Table 4.3. The transparency current density is the current density when the curve crosses the x-axis in the figure of InAsP QDs is nearly 82 A. $cm^{-2}$ while it is 100 $A.cm^{-2}$ for InP QDs.

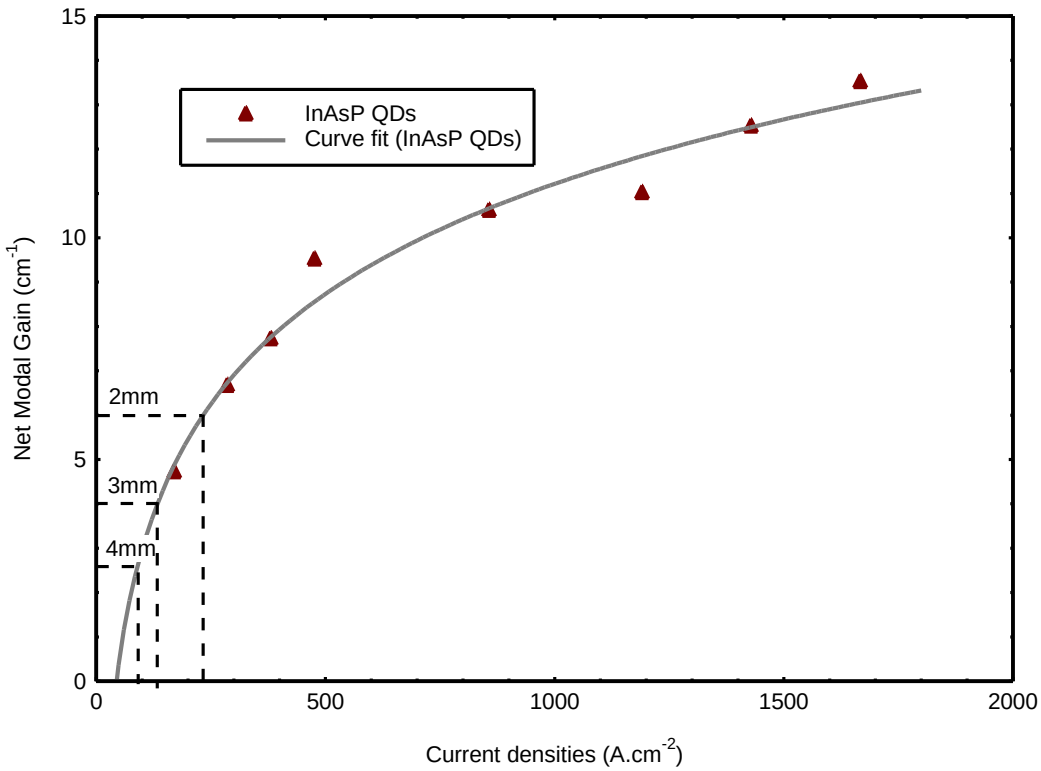


**Figure 4. 12: gain-current relation of InAsP QDs.**

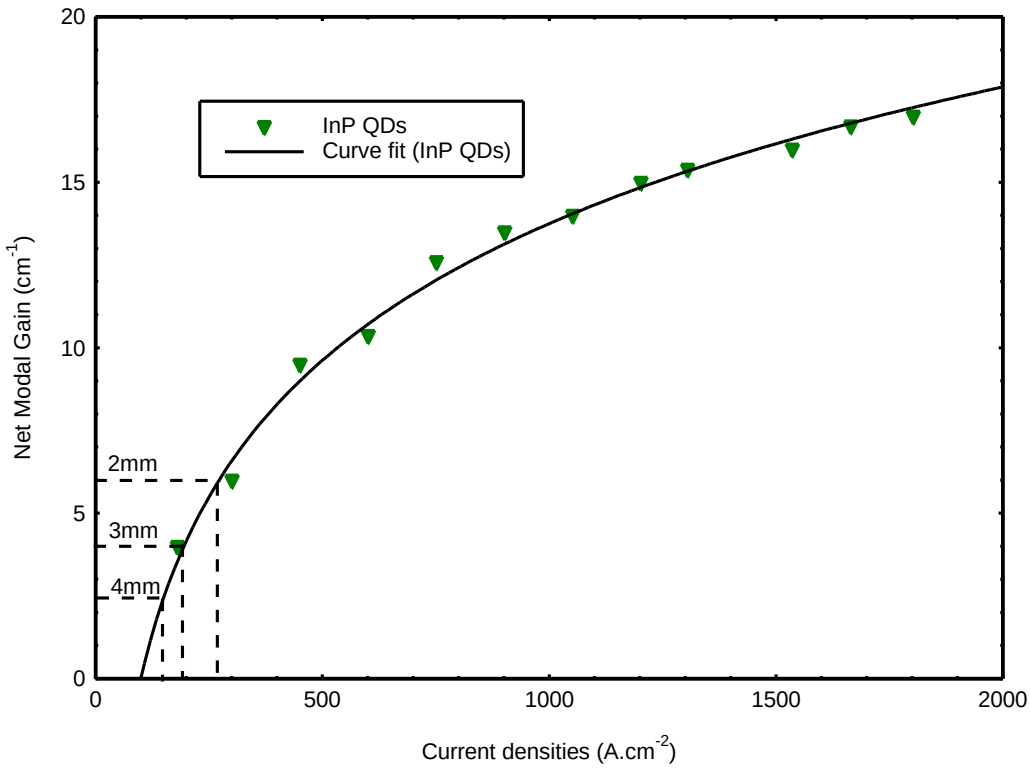


**Figure 4. 13: gain-current relation of InP QDs.**

**Table 4. 3: Extracted threshold current density from the gain measurement for different cavity lengths of InP and InAsP QDs.**

| Cavity length (cm) | Threshold current density InP QDs ($A.cm^{-2}$) | Threshold current density InAsP QDs ($A. cm^{-2}$) |
|---|---|---|
| **2** | 262 | 237.3 |
| **3** | 183 | 137.4 |
| **4** | 139.5 | 89.5 |

InP QDs requires more driven current density to initiate a laser compared to InAsP QDs. However, both materials exhibit much lower threshold current density compared to quantum wells and bulk materials (Sobiesierski & Smowton, 2016).This feature is required for good performance MLLs and the emission of stable pulses (Rafailov et al. 2007). The materials exhibit low threshold current density means that it requires low pumping rate to initiate lasing and thus less ASE. This will enhance the laser in term of noise and jitter. Consequently, both InP and InAsP QDs materials are expected to be run as MLL devices with less instability that might be caused by jitter effect. The timing jitter quantifies the temporal fluctuations of the MLL output that could be resulted from internal noise sources.

A significant factor for determining how stable the passive two-sections MLLs is known as the s-factor or the absorber-to-gain saturation energies ratio. This factor plays a critical role in pulse shaping performance; the gain section is responsible of broadening mechanism while the SA section is responsible of shortening mechanism and an attentive balance between those two mechanisms is needed to achieve stable Mode-Locking operation. The s-factor is the ratio of saturation energies of the gain section to the absorber section (Edik U. Rafailov 2011). The saturation energy of both sections would be directedly deduced from the differential gain (dg/dn) and differential loss (da/dn) from the gain-current relation. The gradient of the curve below the threshold indicates the differential loss (da/dn), whereases the gradient for the curve above the threshold shows the differential gain (dg/dn). We have obtained a bigger

differential loss than differential gain from the gain current plot (Figure 4.14) as it obvious in the two curves. This tells us that the change in absorption with carrier density is much greater than the change in gain with carrier density due to the filling states effect. Nonlinear gain current relation is a significant dynamical feature for mode-locking. Pulse broadening mechanism is caused by the increase of injected current density in the gain-section of passive monolithic MLL, whereas the shortening mechanism of the same pulse is caused by the increase in reverse bias in SA-section. According to the Equation (2.17) mentioned in Chapter 2, the discipline between the two mechanism is governed by the saturation energy of these two sections. However, both studied materials have higher gain saturation energy compared to the QW and bulks. In comparison of the two studied QDs materials, InAsP has higher gain energy saturation than InP has. They fulfil the condition of Mode-locking. The saturation energy of a reverse biased SA-section will be smaller than the saturation energy of forward biased gain-section.

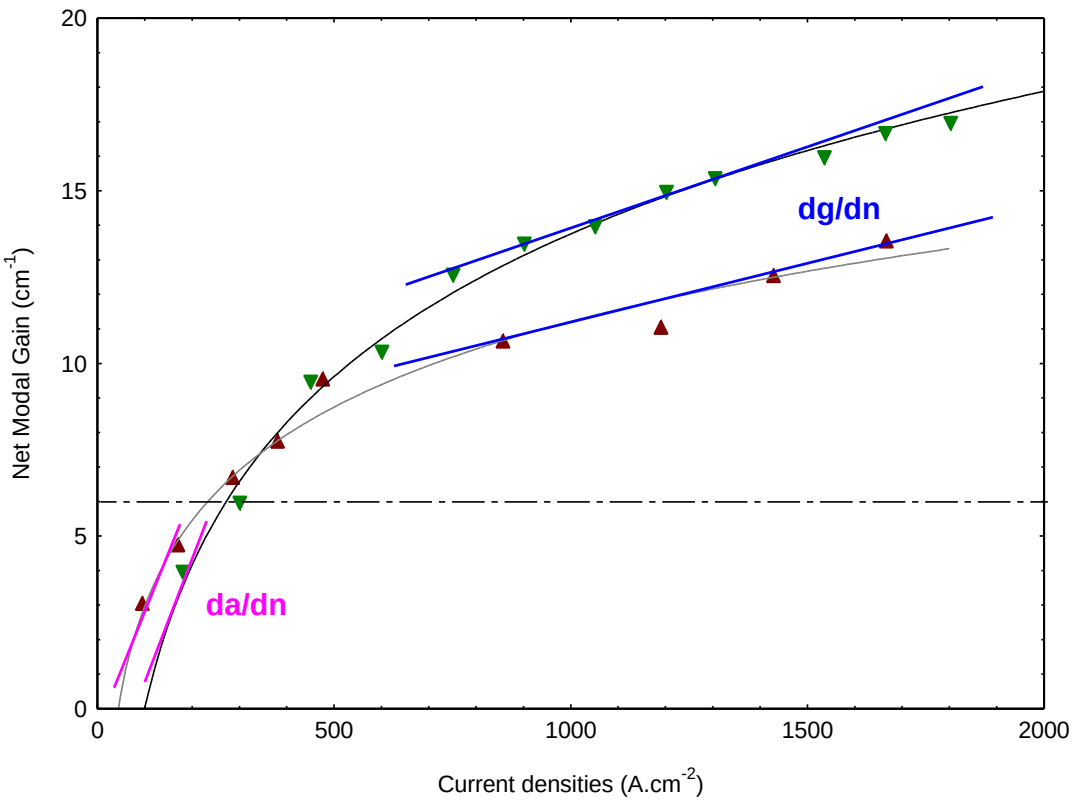


**Figure 4. 14: gain current relation of InP and InAsP QDs ilustrating the differential gain and loss.**

The region, where pulsed operation is occurs, is bounded by two expressions: the mode locking condition and threshold condition of lasing. Both expressions can be found from the gain current relation that have studied in this section. It has been found that both studied materials fulfil those two conditions, and we could achieve stable ML pulses for wavelength range of (728 nm– 735 nm) and (773 nm– 781.8 nm) for InP and InAsP QDs, respectively.

.

## 4.5 Conclusion

The modal gain and absorption at room temperature and for different injected current density has been measured for both QDs materials InP and InAsP. In addition, an investigation of the influence of reverse bias at room temperature has been performed. The ML requirements for achieving ML pulses from those two materials are also studied by the gain- current relation. From these measurements, we have achieved a complete understanding of the characteristic of the forward biased gain-section of passively monolithic MLLs as well as the characteristic of reverse-biased absorber section.

Both materials meet the requirements for generating stable ML pulses. The broad gain bandwidth, higher gain amplitude to overcome the loss, low threshold current density, lower level of ASE and fast gain saturation. Additionally, high differential loss in the absorption regime with low differential gain in the gain regime, the absorption shift range identified.

Limited spectral bandwidth has been found; limited blue-shift tuneability range as well as red-shift tuneability range. The wavelength can be tuned to depends on the value of the reverse bias but this tunning is limited by the characteristics of the quantum dots materials, in particular, the size and the height of quantum dots.

Based on this characterisation, we believe that we could achieve stable ML pulses from both QDs materials InP and InAsP at only limited conditions of gain current and reverse bias of SA, and for specific wavelength tuneability ranges of (728 nm– 735

nm) and (773 nm– 781.8 nm) for InP and InAsP QDs, respectively. For InP QDs, we could achieve ML pulses from shorter cavity resonator due to the high gain it owes, but with wider pulsed width. In contrast, we could achieve shorter pulse width from InAsP QDs, but only with longer cavity length due to the lower gain amplitude. In short, InAsP QDs are more broadband and InP QDs have higher gain, leading to the predictions of the possibility of achieving Mode-locking pulses from InP QDs at lower pumping rate, but wider pulse width compared to InAsP QDs .

## References

Al-Ghamdi, M.S., Smowton, P.M., Blood, P. and Krysa, A.B. 2011. Dot density effect by quantity of deposited material in InP/AlGaInP structures. *IEEE Photonics Technology Letters* 23(16), pp. 1169–1171. doi: 10.1109/LPT.2011.2157910.

Edik U. Rafailov, Maria Ana Cataluna and Eugene A. Avrutin 2011. *Ultrafast Lasers Based on Quantum dot Structure:Physics and Devices*. first edition. Rafailov. Edik, Cataluna. M. Avrutin. E. ed. Germany: WIELY-VCH.

Park, G., Shchekin, B.O., Huffaker, D.L., and Deppe, D.G. 1998. Lasing from InGaAs/GaAs quantum dots with extended wavelength and well- defined harmonic-oscillator energy levels. *Appl. Phys. Lett.* 73, pp. 3351–3353.

Blood, P. (2015). Quantum Confined Laser Devices: Optical gain and recombination in semiconductors. Oxford: Oxford University Press.

Porsche, J., Ost, M., Scholz, F., Fantini, A., Phillipp, F., Riedl, T. and Hangleiter, A. 2000. Growth of self-assembled InP quantum islands for red- light-emitting injection lasers. *IEEE J. Sel. Topics Quantum Electron* 6(3), pp. 482–490.

Rafailov, E.U. and Avrutin, E. 2013. Ultrafast pulse generation by semiconductor lasers. In: *Semiconductor Lasers: Fundamentals and Applications*. Elsevier Ltd, pp. 149–217. doi: 10.1533/9780857096401.1.149.

Rafailov, E.U., Cataluna, M.A. and Sibbett, W. 2007. Mode-locked quantum-dot lasers. *Nature Photonics* 1(7), pp. 395–401. doi: 10.1038/nphoton.2007.120.

Schulz, W.-M., Rossbach, R., Reischle, M., Beirne, G.J., Bommer, M., Jetter, M. and Michler, P. 2009. Optical and structural properties of InP quantum dots embedded in Al Ga In P. *Phys. Rev. B,* 79

Sobiesierski, A. and Smowton, P.M. 2011. Quantum-Dot Lasers: Physics and Applications. *Chapter 2 Comprehensive Semiconductor Science and Technology* (6). pp 353-384.

Williamson, A.J., 2002. Energy states in quantum dots. *International journal of high speed electronics and systems*, 12(01), pp.15-43.

# Chapter 5:

# A Novel approach for optimising InP QD passively monolithic MLLs

## 5.1 Introduction

In Chapter 4, we have concluded that InP QD materials can generate ML pulses at specific conditions. In this chapter, we are interested in investigating the performance of ML pulses of InP QD passively monolithic MLLs. Therefore, we propose a novel semi-empirical approach that is used as a basis for predicting the optimal performance of InP QDs passive monolithic MLLs. The chapter starts with detailed guidelines of the criterion of determining the ML regimes. Investigating the performance begins with studying the characterisation of net MLLs modal gain at different gain-section current density, at various reverse bias conditions, and for different device designs in term of absorber-to-gain length ratios. This is followed by the investigation of the influence of the same parameters on threshold current density for the studied device designs. By understanding these characterisations and by using the criterion described in the first section, we are able to predict the operational map of the bias conditions and the lasing wavelength and spectral width of the ML pulses. Moreover, we have explored the ML trends, blue-shift of wavelengths with the increase of forward bias, red-shift with increasing reverse bias, the broadening and shortening mechanisms at various absorber-to-gain length ratios. In other words, we examine the formation of the ML pulse shapes. This approach will be helpful to design the most reliable device with the shortest ML pulses that could be achieved from the InP QD material and provides a priori understanding of what limits the best performance that could be achieved.

## 5.2 Basis of semi-empirical approach

Here in this section, we aim to provide an insightful overview of the semi-empirical approach established in this work. It is based on combining the modal gain as a function of current density data and the modal absorption as a function of reverse-bias data that have been measured and discussed in Chapter 4, Figure 4.4 and Figure 4.7. The combination was constructed for different absorber-to-gain lengths ratios in order to simulate the conditions of a laser under a mode-locked regime and design the best performing InP QD MLL devices. The three significant parameters that most impact the performance of passively monolithic MLL as shown in the literature ((Thompson et al. 2009) , (Brown et al. 2007), (Mee et al. 2014)) are , gain-section current density, reverse bias, and absorber-to-gain length ratio. The main step to optimize the device performance is to predict the net MLL modal gain by combining the modal absorption data as a function of the reverse bias into the modal gain data as a function of current density at specific designs of absorber-to-gain length ratios 1:3, 1:4, 3:17, 1:9, and 1:19.

In passively monolithic MLLs, a trade-off must be made between the gain and the absorption to obtain the most reliable ML pulses. The gain dynamic represents the broadening pulse performance, and the absorption dynamic represents the shortening shape performance. It has been proven in literature that ML operation occurs at the gain saturation and additional gain is required to overcome the loss due to the absorption (Rafailov et al. 2013). Based on this knowledge, we have established a criterion for determining ML regimes in our approach. The boundary condition of the operating biases necessary to provide the mode-locking regime is that their net MLL gain curves should lie on or slightly above the gain threshold line (the level of gain requirement). Any net MLL modal gain curves that are above the threshold from 0 $cm^{-1}$ to approximately 2 $cm^{-1}$ could be considered in ML regime. To clarify this point, an example of the net MLL gain versus the wavelength is plotted for all the studied absorber-to-gain length ratios in Figure 5.1 at bias conditions $J_{gain}$= 1803 $A.cm^2$ and $V_{abs}$=1 V. The dashed lines represent the gain peaks, and these peaks shift toward longer wavelengths as the SA-section length increases. According to the established criterion, the device with absorber-to-gain length ratio designs that are expected to

generate ML pulses under these fixed bias conditions ($J_{gain}$= 1803 A.cm$^2$ and $V_{abs}$=1 V) are 1:4 and 3:17 (see Figure 5.1).

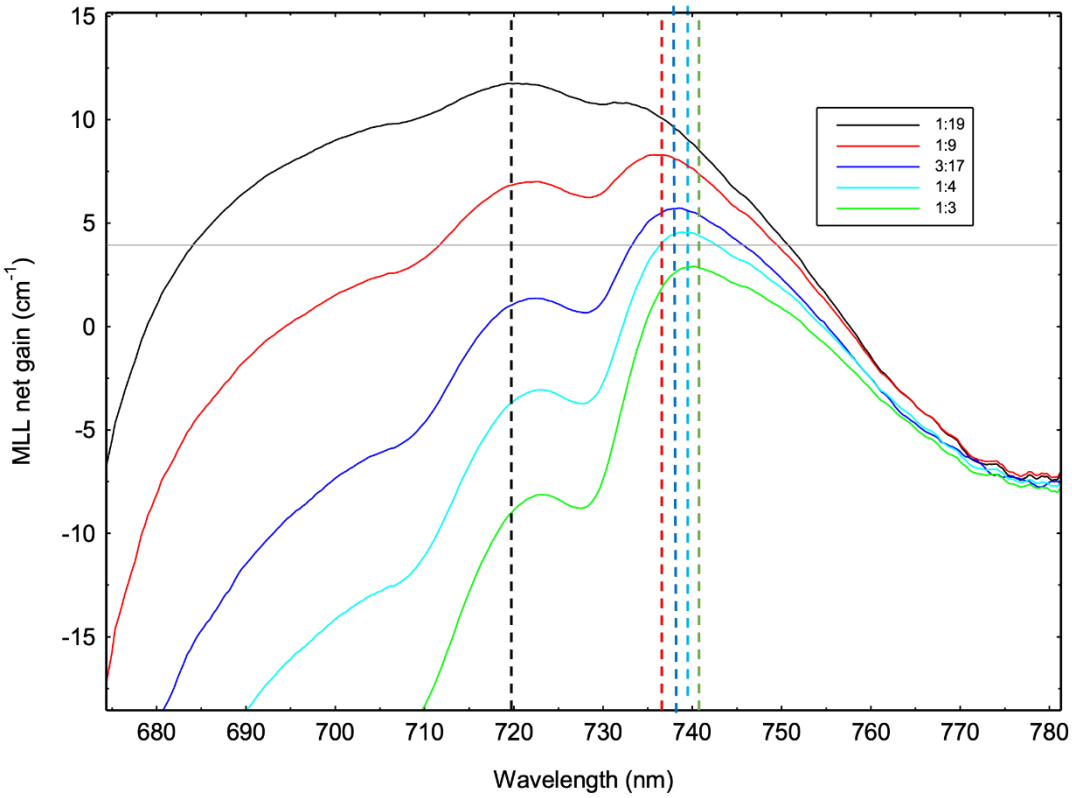


**Figure 5. 1 : Net MLL gain versus wavelengths for all investigated absorber-to-gain length ratios at fixed gain current density 1803 A.cm-2 and fixed reverse bias of SA-section 1 V.**

## 5.3 Characterisation of net MLL modal gain

Figures 5.2, 5.3, 5.4, 5.5 and 5.6 present the predicted net InP QD MLL modal gain of device designs with absorber to gain lengths ratios of 1:19, 1:9, 3:17, 1:4, and 1:3, respectively. This has been analysed for different gain current density starting from approximately 300 A.cm$^{-2}$ to 1803 A.cm$^{-2}$, and a range of selective fixed reverse biases between (1 V– 6 V). The observed general behaviour of the net MLL modal gain versus current density is in line with the behaviour of the net modal gain of a laser plotted in Chapter 4, Section 4.3. The gain peak amplitudes and width increase with the increase in the current density until they eventually become saturated at high current density for the studied cavity designs, and this is attributed to the state-filling of the inhomogeneously broadened states resulting from the different sized QDs

(Blood 2015). The same behaviour pattern is seen for all the net MLL modal gain curves for each fixed reverse bias. The wavelength peak of the device with ratio 1:19 is blue-shifted from 735 nm at 300 A.cm$^{-2}$ to 720.6 nm at 1803 A.cm$^{-2}$, and the gain amplitude is saturated at approximately 11 cm$^{-1}$ at the highest gain current density. For other device designs and under the same conditions, the blue-shift of wavelength peaks vary as reported in Table 5.3.1 and the saturation level of device designs 1:9, 3:17, 1:4, 1:3 is at 8 cm$^{-1}$, 6 cm$^{-1}$, 5 cm$^{-1}$ and 2 cm$^{-1}$ respectively. It can be seen from the reported peak wavelength ranges for the different device designs that the blueshift rate decreases as the length of the absorber section increases, and there is also a reduction in the saturation level at longer SA lengths. These obvious changes in the blueshift rate and the saturation level of the studied device designs are a consequence of the maximizing of the absorption of the material waveguide. Specifically, when the SA is added to the device, the absorption data that combined to the gain data, manifest in a minor shortening effect observed at the middle of the curve for the lowest absorber section and starts to include shorter wavelengths as the absorber lengths increase, indicating an impact on the gain peak amplitude and wavelengths. The shortening effect is minimal on the device with the lowest SA-section length of ratio 1:19, and the broadening performance is dominant because the absorption is not enough to establish ML pulses. It gradually increases in both amplitude and width with the increase of the length of the SA. The widths increase to include shorter wavelengths as the SA length increases. The shortening mechanism eventually becomes dominant at ratio 1:3. Accordingly, there will be no ML pulses or lasing generated from the material with the longest SA section of device with absorber-to-gain length ratio of 1:3.

Switching to reverse bias of the SA for device designs with the shortest SA-section length 1:19 has no impact either on the gain amplitude or the wavelength peaks. The impact of changing to reverse bias for device designs with longer absorber sections 1:9, 3:17, 1:4, and 1:3 dramatically reduces the gain amplitude and moderately influences the peak wavelengths, spectral width and shaping performance. It has been observed that the reverse bias has a significant impact on the red-shift range of wavelengths. The wavelength shifts toward longer wavelengths with reverse bias is due to QCSE that described in Chapter 2, Section 2.5 (Mark Fox 2010). The range of redshift wavelengths increases gradually with the increasing the length of the SA-

sections (Table 5.1). When a reverse bias is applied to the SA section, the carriers photogenerated by the pulse can be easily swept out from the SA, allowing the SA to return to its original state of high loss more rapidly. Increasing the reverse bias reduces the absorber's recovery time, which results in further shortening of the pulse (Rafailov et al. 2013).

**Table 5. 1: Blue-shift and red-shift wavelength ranges for the studied absorber-to-gain length ratios of 3mm cavity length. The blue-shift resulted from increasing the gain carrier density at fixed reverse-bias of 1 V whereas the red-shift resulted from increasing the revers-bias at fixed gain current density of 1803 A.cm$^{-2}$.**

| Absorber-to-gain length ratios | Blue-shift wavelength range (nm) | Red-shift wavelength range (nm) |
|---|---|---|
| **1:19** | 735-720.6 | 720.2-724.4 |
| **1:9** | 738-734 | (736.9-741.9) and (721.7-727.6) |
| **3:17** | 739-737 | 737.6-745 |
| **1:4** | 740-739 | 738.7-742 |
| **1:3** | 740.3-739.5 | 739-746 |

Compared to the modal gain characteristics of a laser device with no passive waveguide section that was previously reported in Chapter 4, Section 4.3, we have found that the gain amplitude was reduced by 5 cm$^{-1}$ at the highest gain current density with ratio 1:19 and reduced by 13 cm$^{-1}$ of the ratio with the longest SA length 1:3. Additionally, the blue-shift rate narrows with the increase of the absorber lengths,

whereas, in contrast, the redshift rate expands. It seems that greater pulse shortening occurs in the devices with longer absorber sections. The internal optical loss is nearly the same for all net MLL gain curves (-6 ± 1) $cm^{-1}$ extracted from the region of long wavelengths where the gain curve converges with the absorption curve.

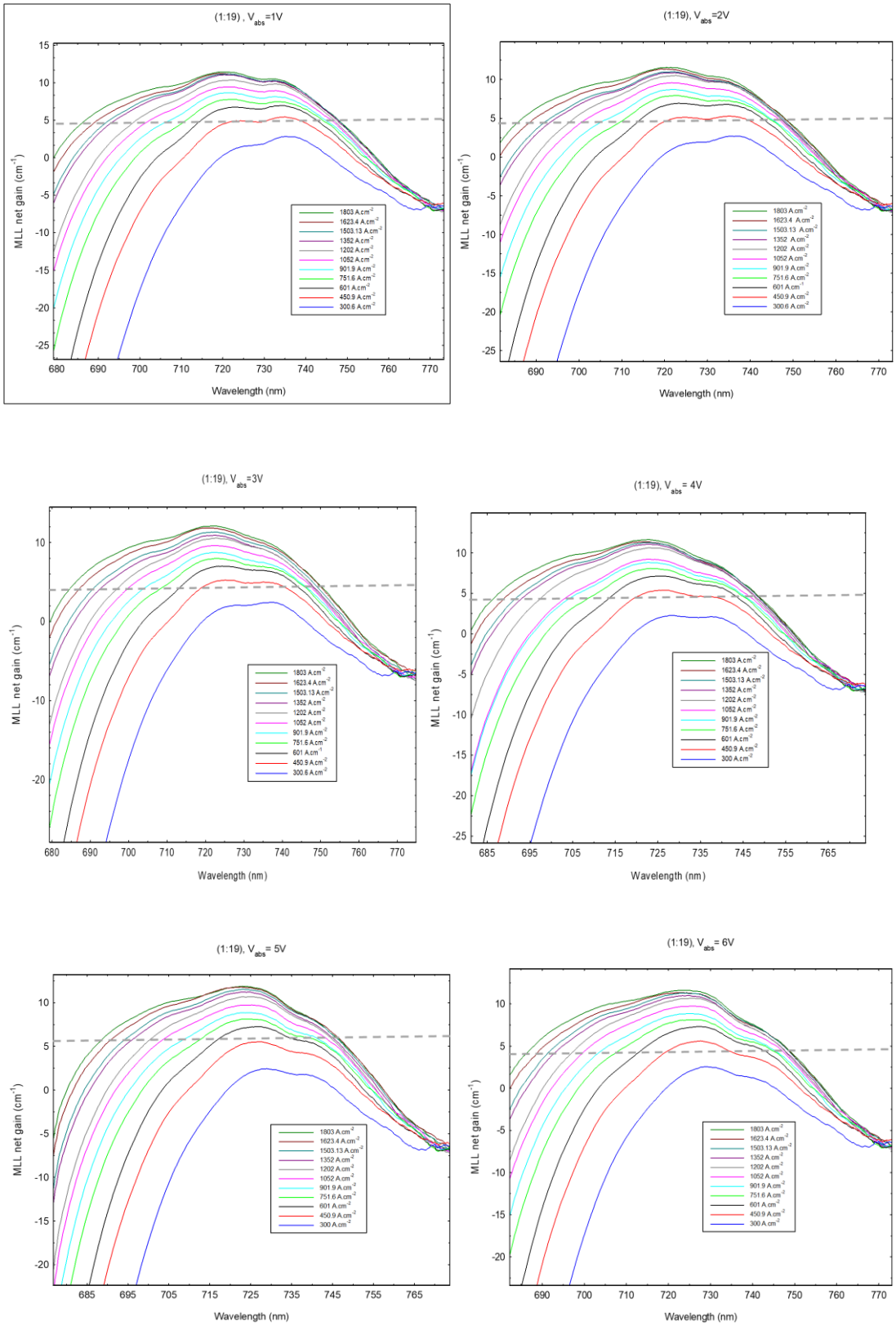


**Figure 5. 2 : The net MLL modal gain of a device design (1:19) at various fixed reverse bias (1 V, top left –6 V, bottom right) (The dashed line on the graphs represents the gain requirement).**

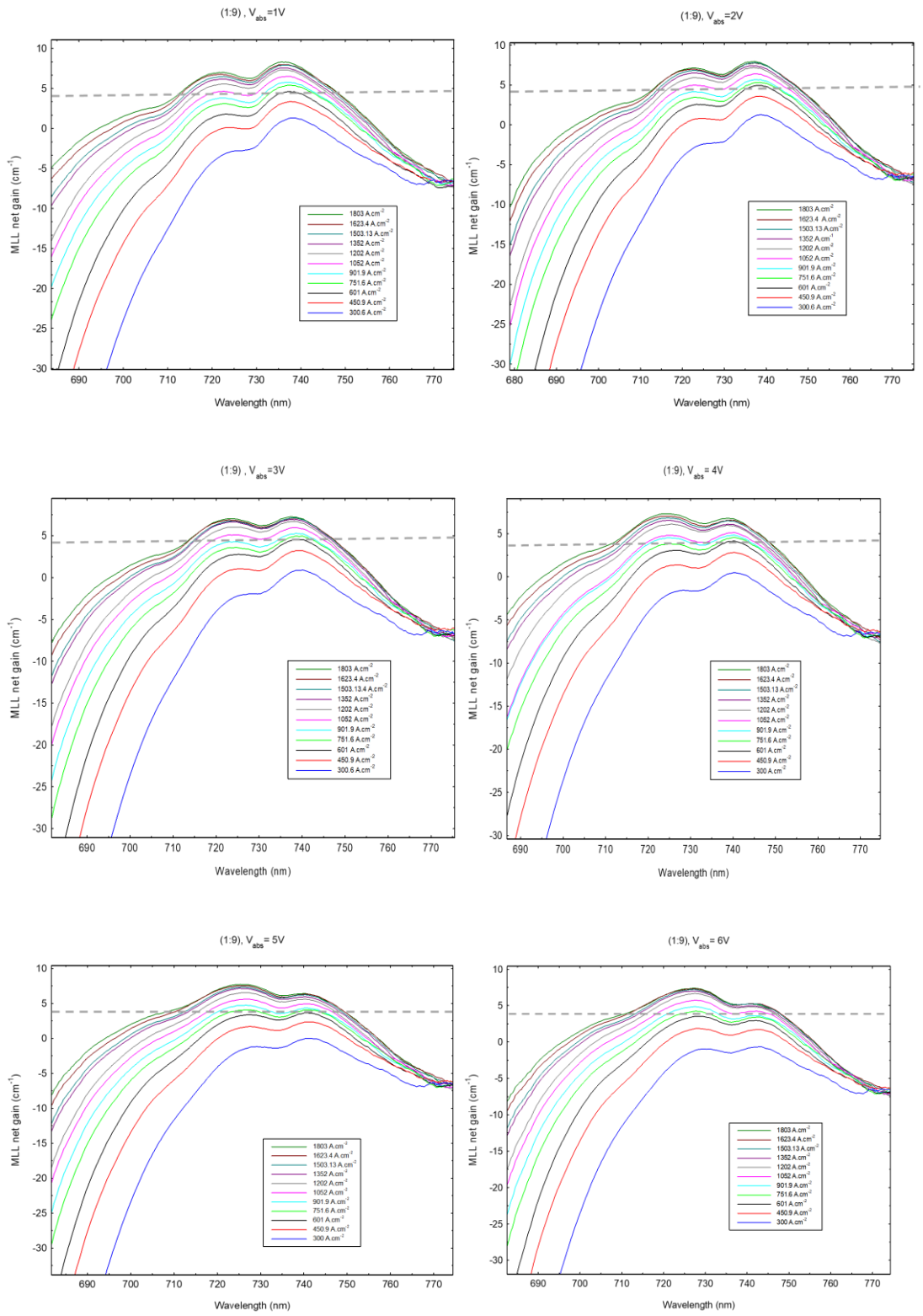


**Figure 5. 3 : The net MLL modal gain of a device design (1:9) at various fixed reverse bias (1 V, top left –6 V, bottom right) (The dashed line on the graphs represents the gain requirement).**

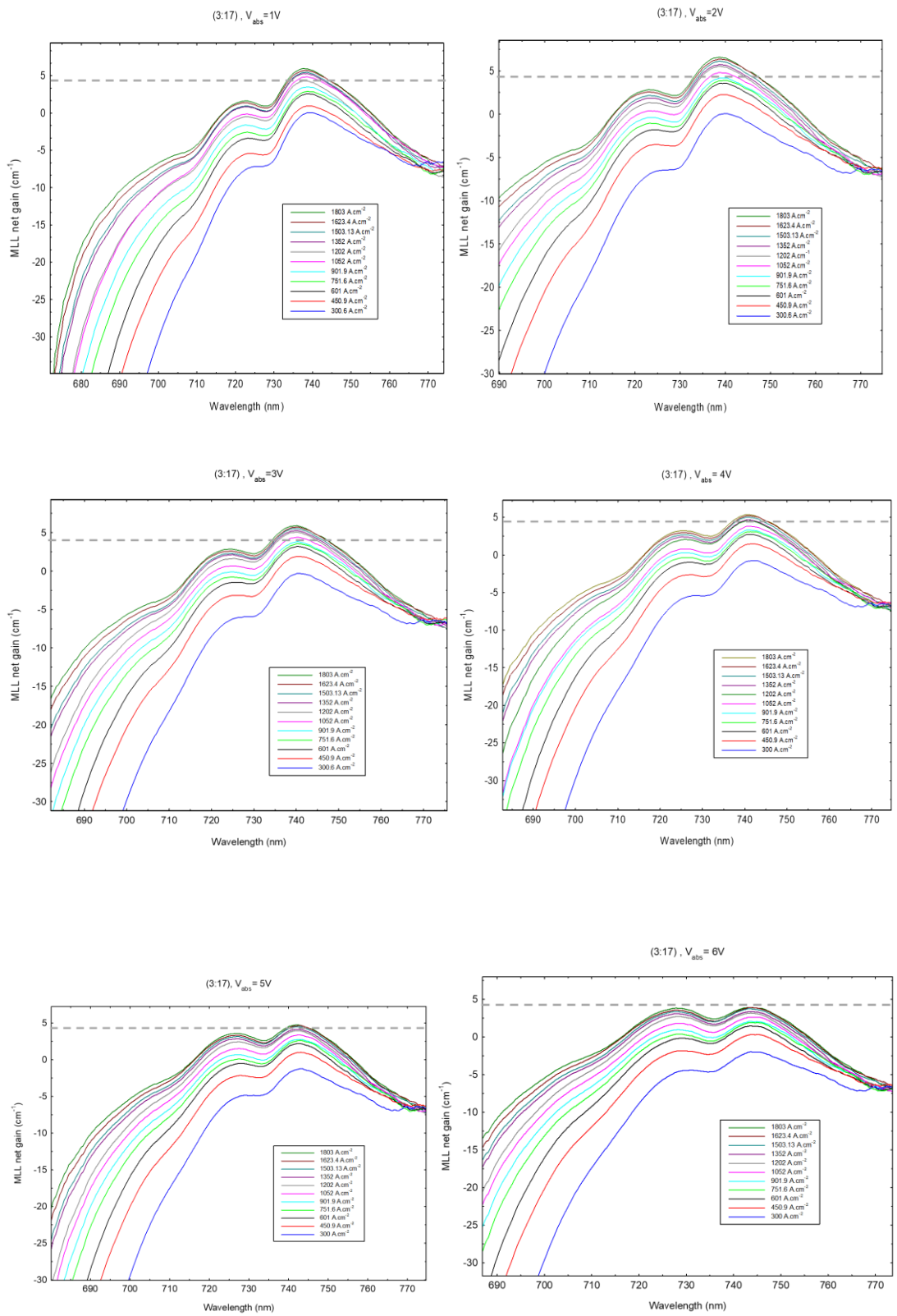


**Figure 5. 4 : The net MLL modal gain of a device design (3:17) at various fixed reverse bias (1 V, top left –6 V, bottom right) (The dashed line on the graphs represents the gain requirement).**

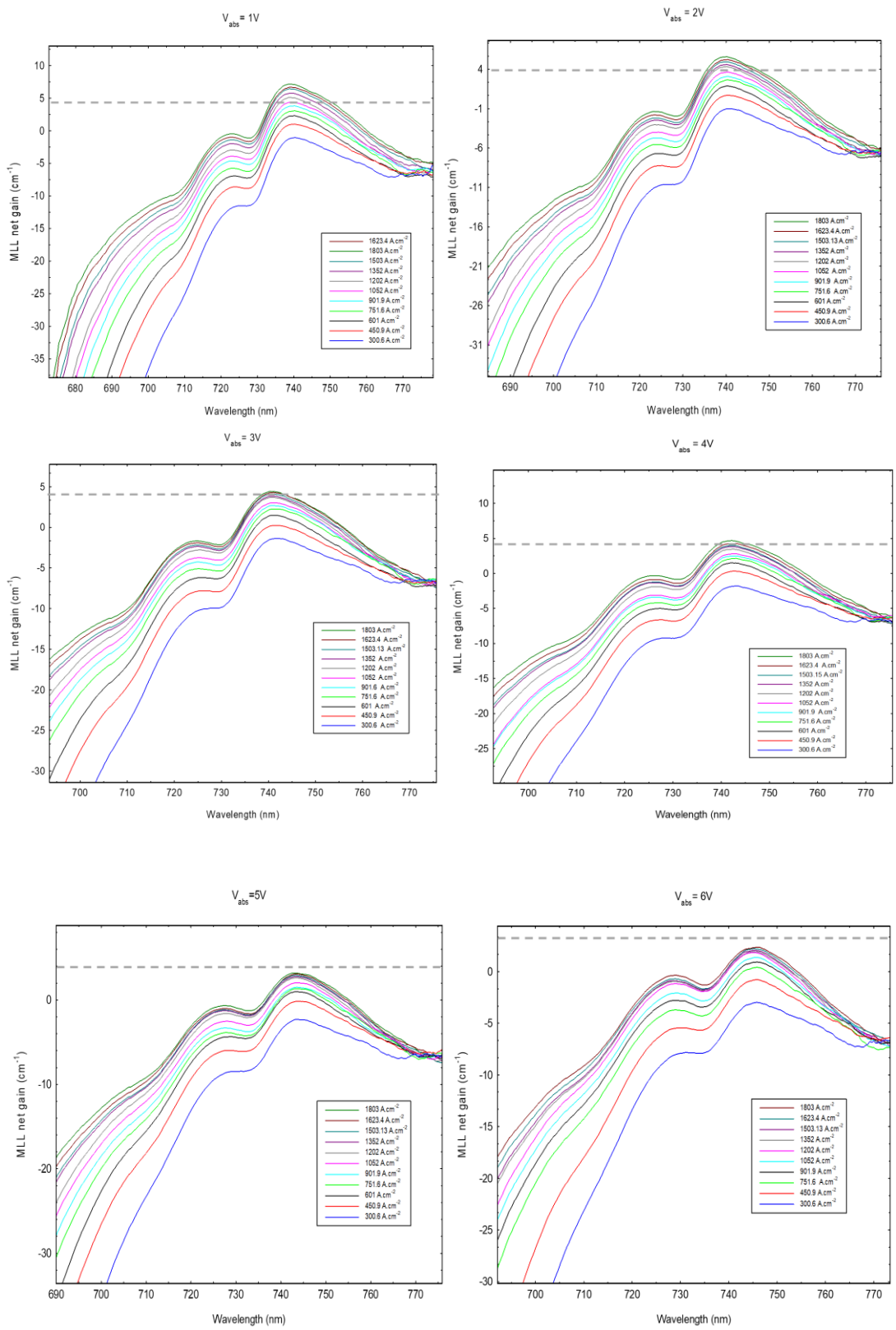


**Figure 5. 5 : The net MLL modal gain of a device design (1:4) at various fixed reverse bias (1 V, top left –6 V, bottom right) (The dashed line on the graphs represents the gain requirement).**

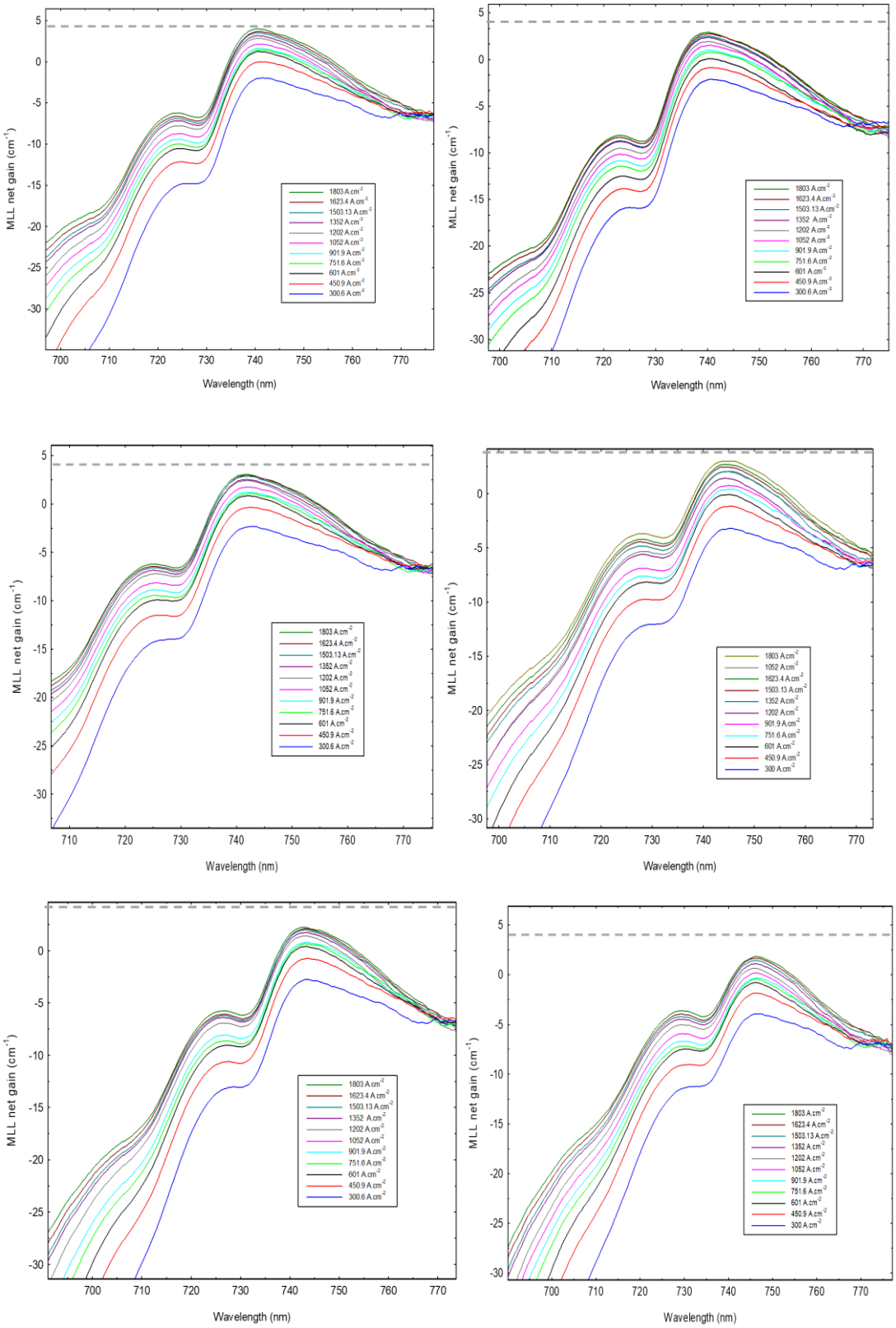


**Figure 5. 6 : The net MLL modal gain of a device design (1:3) at various fixed reverse bias (1 V, top left –6 V, bottom right) (The dashed line on the graphs represents the gain requirement).**

An interesting observation has been found using this approach. The device at absorber-to-gain length ratio of 1:9 and at reverse bias conditions of 3 V, 4 V, 5 V and 6 V could generate two pulses circulating in the device during the same duration time in two modes: GS and ES. Figure 5.7 illustrates the generation of GS and ES ML pulses. The influence of the increase of reverse bias on the gain amplitude of the two ML pulses is clearly seen as the decrease of GS peak amplitude. This decrease corresponds to the increase of gain peak amplitude of ES. This behaviour is associated with the saturation of GS and the transition to the ES region. The ML pulses could be operated on GS and ES modes of wavelength approximately (724.3 nm to 727 nm) and (738.9 nm- 741.9 nm), respectively under this range of current density (901.9 A.cm$^2$ and 1052 A.cm$^2$). This significant feature could lead to the new generation of tuneable passive ML devices that provide stable ML pulses at different wavelength in the shorter wavelength range for bio-photonics applications.

In comparison to the other QD passive monolithic MLL studied in the literature, there is only one report of experiments using QD passive MLL that involving a ML operation in two modes: GS and ES in the long wavelength range (O band) for telecommunication applications (Cataluna et al. 2005; Cataluna et al. 2006) .

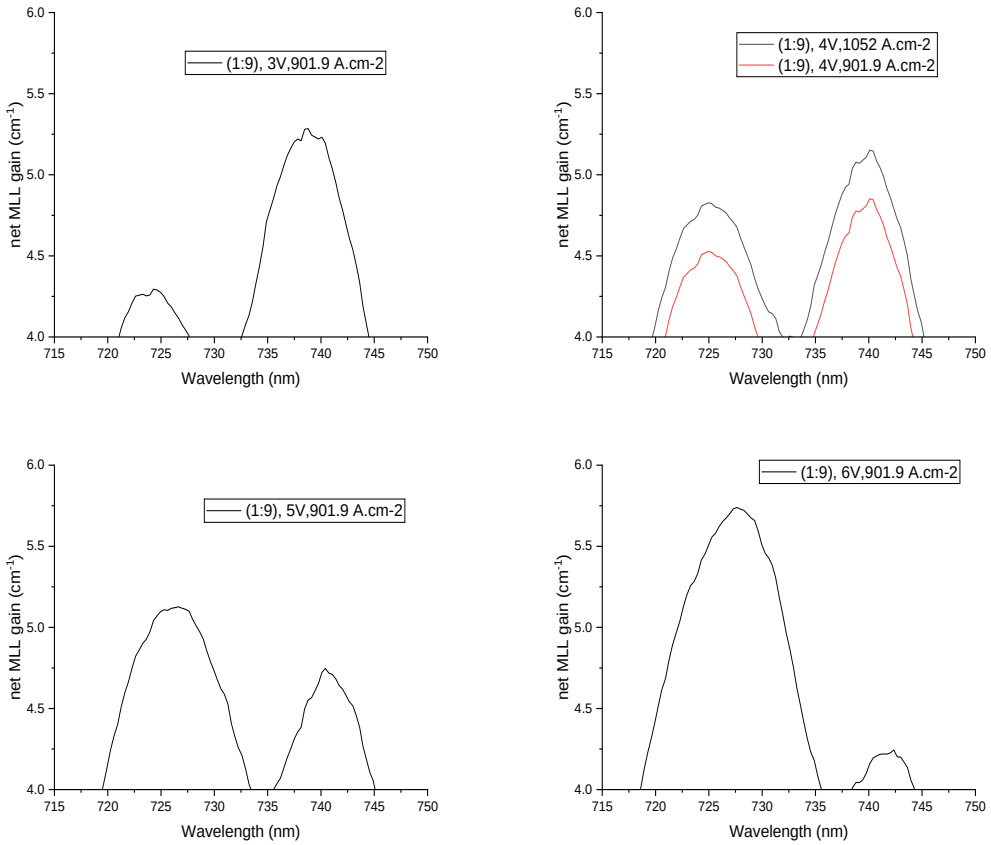


**Figure 5. 7 : The net MLL modal gain of a device design (1:9) at specific driving conditions when double pulse regime (GS and ES) is generated.**

## 5.4 Gain-current density characteristic

In passive monolithic MLLs, stable ML pulses can be achieved by deliberately regulating the pulse broadening and pulse shortening mechanisms within the device. Saturable absorption in the reverse biased absorber section creates pulse shortening, whereas gain saturation in the forward biased section creates pulse broadening. The condition of this regulating and thus, generation of ML pulses, has been described in Chapter 2, Section 2.4.3.1 Here in this section, we are investigating the impact of SA-section length and increasing reverse bias absorber voltages on net differential MLL modal gain and, consequently, the gain saturation and the threshold current density.

The gain-current curves for different ML devices with different absorber-to-gain length ratios 1:19, 1:9, 3:17 and 1:4 are illustrated in Figure 5.8 Figure 5.9, Figure 5.10, and Figure 5.11, respectively. The curve fit used is the same as that used in

Chapter 4, Section 4.4 and is described in Chapter 2, Section 2.8. The device design with the shorter absorber length 1:19 shows an insignificant impact on the net differential modal gain and consequently gain saturation and threshold current density. Interestingly, the devices with longer absorber sections 1:9, 3:17 and 1:4 exhibit a significant impact on these parameters and the impact becomes more noticeable with the increase in the absorber length and the increase in reverse bias voltage. The net differential MLL modal gain is identified as the rate of change in net gain with current density. Therefore, it can be linked to the blueshift ranges described above in section 5.3 and presented in Table 5.1. It was clear that the decrease in blue-shift ranges corresponded to the increase in absorber length. This confirms the impact of absorber length on the net differential MLL modal gain, hence the gain saturation and the ML stability condition (the differential gain in the gain regime must be lower than the differential loss in the absorption regime) (Haus 2000). Additionally, the application of reverse bias on all device designs decreases the differential gain in the gain regime, but the differential gain is still greater in the absorption regime that provides faster absorption saturation. In brief, all the investigated device designs fulfil the ML stability condition.

The threshold current density are listed in Table 5.2 for all device designs and reverse bias conditions. The threshold current density are shifted significantly higher from the threshold current density of the InP QD laser device previously reported in Chapter 4, Section 4.4. This is attributed to the increasing absorption within the waveguide and due to the increase of non-radiative recombination. For a device design with the shortest SA length, the result shifted higher with a 182.5 $A.cm^{-2}$ difference at all reverse bias conditions. For device designs with longer absorber section length, the differences are slightly higher due to the to the increasing absorption within the longer SA-section and due to the increase of non-radiative recombination.

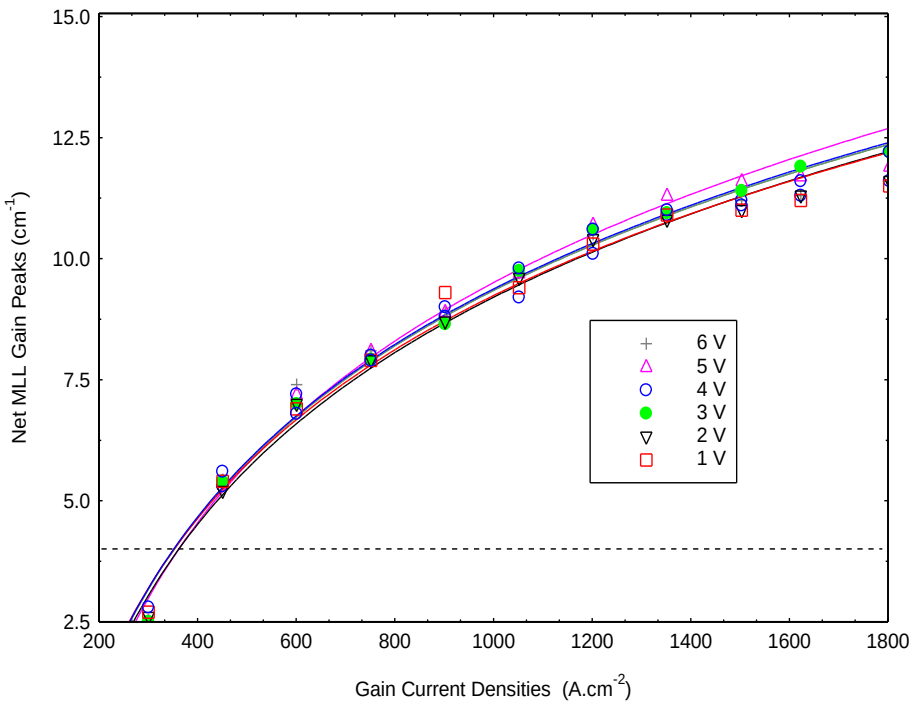


**Figure 5. 8 : The gain-current curve of device design 1:19 as a function of current density and for various reverse bias conditions (1 V– 6 V) (Uncertainty values =gain peaks ± 0.4).**

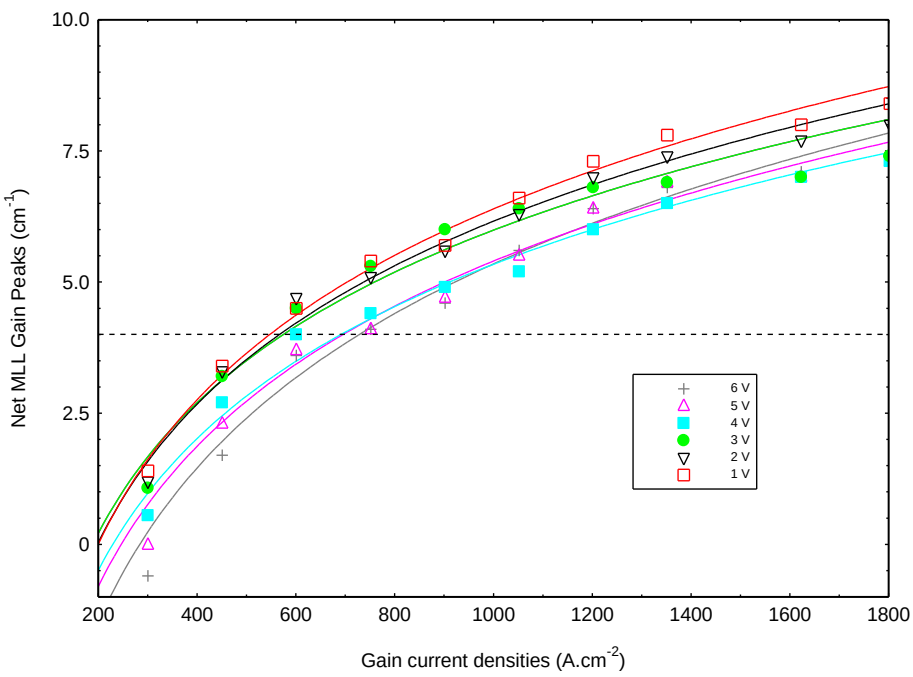


**Figure 5. 9 : The gain-current curve of device design 1:9 as a function of current density and for various reverse bias conditions (1 V– 6 V) ) (Uncertainty values =gain peaks ± 0.4).**

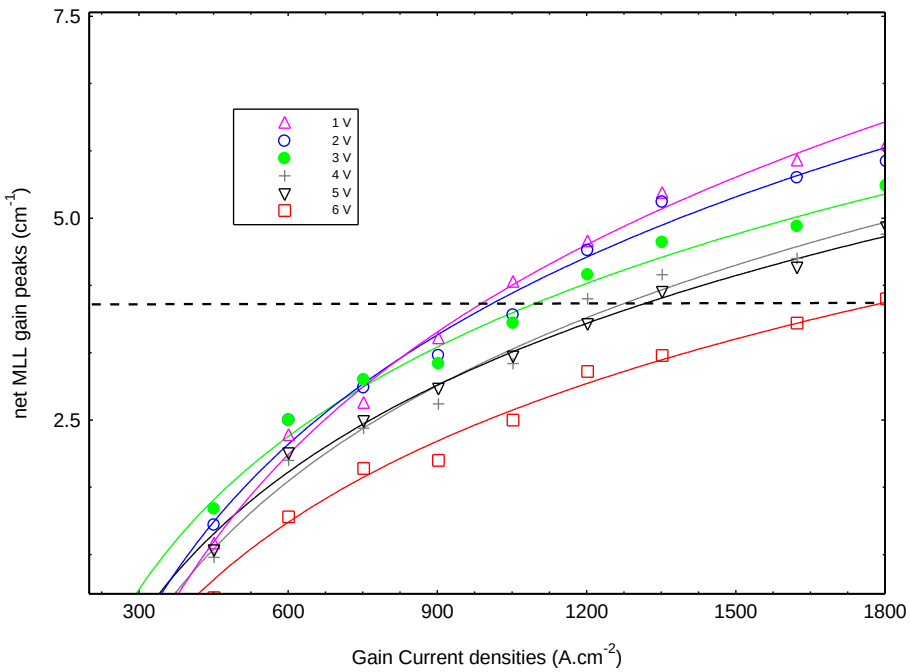


**Figure 5. 10 : The gain-current curve of device design 3:17 as a function of current density and for various reverse bias conditions (1 V– 6 V) ) (Uncertainty values =gain peaks ± 0.4).**

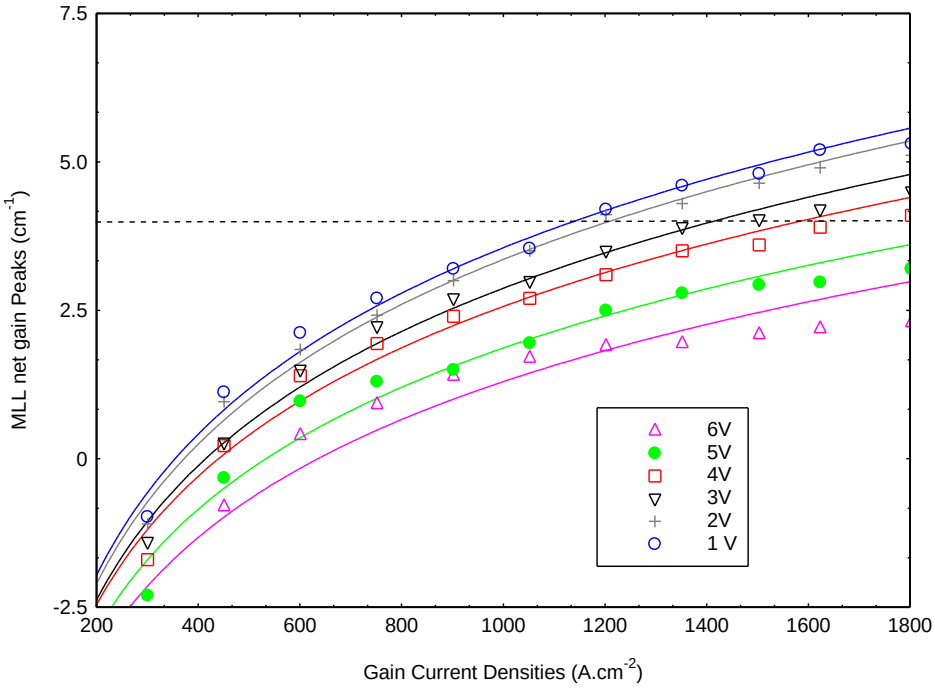


**Figure 5. 11 : The gain-current curve of device design 1:4 as a function of current density and for various reverse bias conditions (1 V– 6 V) ) (Uncertainty values =gain peaks ± 0.4).**

**Table 5. 2: Threshold current density for all studied absorber-to-gain length ratios and at fixed reverse bias ranged between (1 V– 6 V).**

| Absorber Reverse-bias (V) | Threshold Current Density ($A.cm^{-2}$) | | | |
|---|---|---|---|---|
| | 1:19 | 1:9 | 3:17 | 1:4 |
| **1** | 356.5 | 542 | 985 | 1127 |
| **2** | 356.5 | 574 | 1017 | 1225 |
| **3** | 356.5 | 587 | 1092 | 1418 |
| **4** | 356.5 | 676 | 1262 | 1598 |
| **5** | 356.5 | 686 | 1332 | - |
| **6** | 356.5 | 726 | 1803 | - |

## 5.5 Influence of reverse bias and absorber section length on threshold current density

It is observed from the gain-current density analysis in the previous section that the extent of the influence of reverse bias voltage on threshold current density is strongly correlated to the length of the SA-section. This extent increases with the increase of the SA-section length. Figure 5.12 illustrates the impact of absorber to gain length

ratios of a passive MLL on the threshold current density for different SA reverse bias voltages between 0 and 6 V. The required threshold current density increases as the absorber length increases. The impact of the increase of absorber length in the device length ratio on threshold current density is changing dramatically due to the fact that longer SA-section would require more current density to allow the gain to build up. Therefore, the influence of reverse bias absorber voltage on threshold current density is governed by the length of the absorber section.

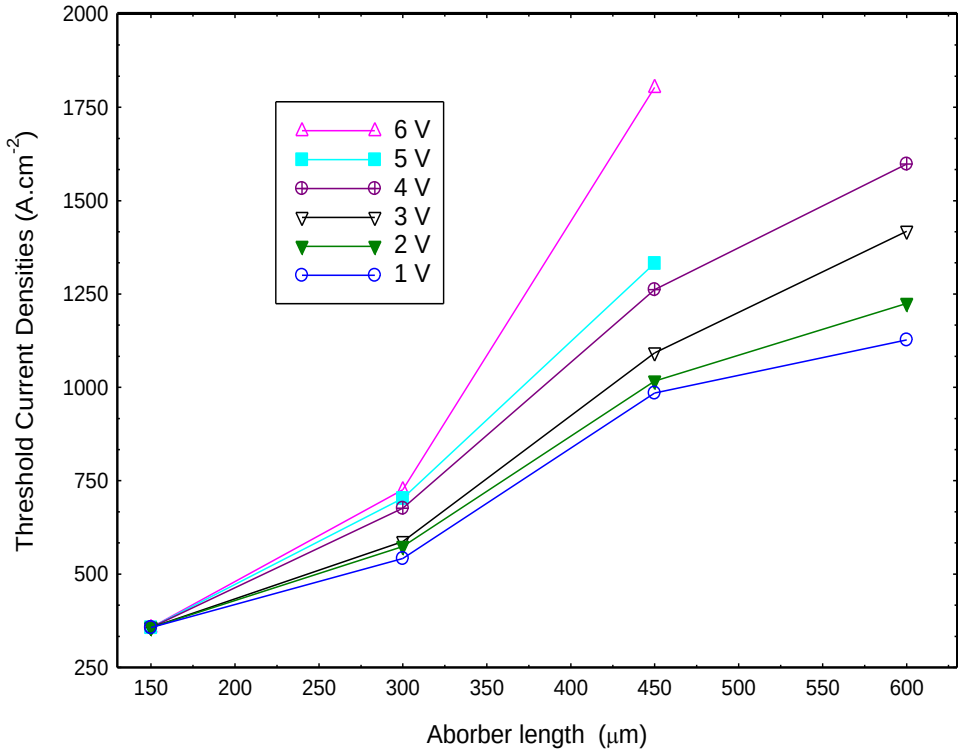


**Figure 5. 12 : The threshold current density as a function of SA length for various reverse bias conditions (1 V– 6 V).**

Figure 5.13 shows the impact of reverse bias voltage (1 V– 6 V) on threshold current density for different investigated absorber-to-gain length ratios of a passive MLL. The impact of the reverse-bias is not significant in the shortest SA-section lengths however, it becomes significant as the SA length is increased. This shows that it is difficult to mode-locking behaviour with SA-section lengths greater than 600 µm for a 3mm total cavity length laser in this material.

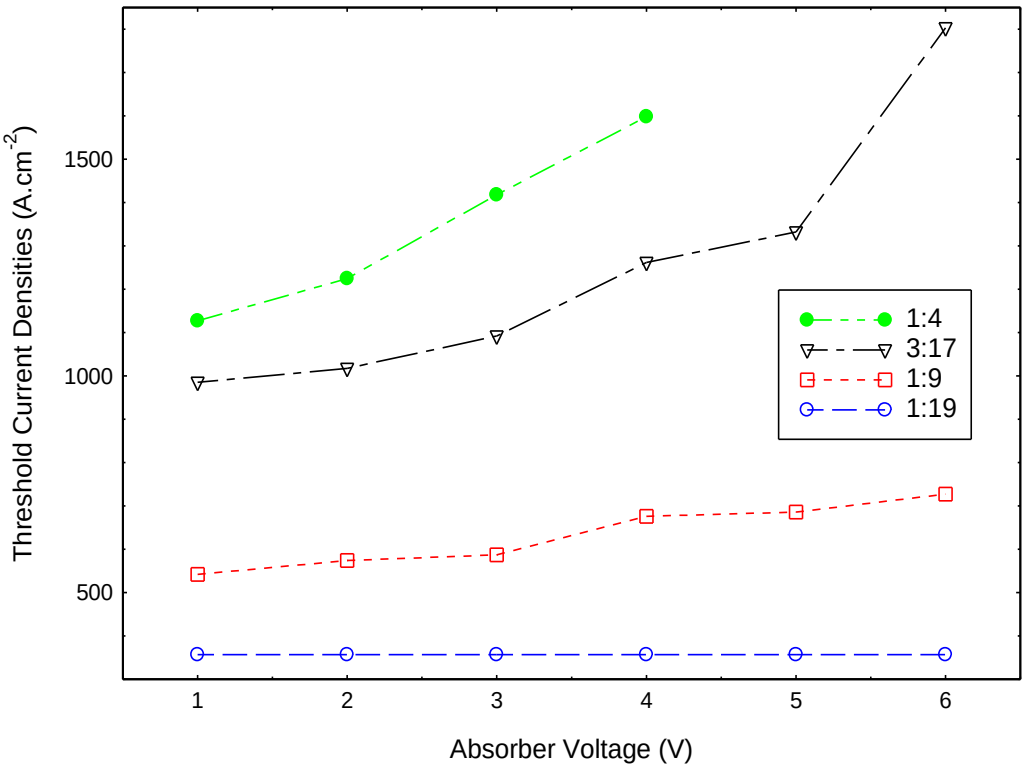


**Figure 5. 13 : The threshold current density as a function of reverse biases for all investigated device length ratios designs.**

## 5.6 Mapping of the operational bias conditions

Figures 5.14 shows the maps of the operational conditions for all the device designs 1:19, 1:9, 3:17, 1:4 and 1:3, the method to determine the mode-locking regions described in Section 5.2. It illustrates the region of ML, lasing and non-lasing in terms of driving conditions: gain current density and reverse bias. The broader ML regime range predicted for devices with this absorber-to-gain length ratio 3:17 over the reverse bias absorber voltage range from 1 V to 5 V and at high drive current density above 901.9 A.cm$^{-2}$. The increase of reverse bias reduces the range of ML regimes. For the device with length ratio 1:4, the ML regime is determined over a reverse bias absorber voltage range only between 1 V to 4 V and at high drive current density above 1202 A.cm$^{-2}$. The range of ML narrows with the increase of reverse bias to 3 V and 4 V, and no ML regime is predicted for reverse bias above 4 V.

The ML regime predicted at low current density in devices with length ratio 1:9 is between 601 $A.cm^{-2}$ and 1052 $A.cm^{-2}$ and over the entire studied reverse bias absorber voltage range (1 V- 6 V). There are no ML regimes predicted for devices with length ratio 1:19, but only lasing due to the SA length being too short, resulting in inadequate saturable absorption for pulse shortening. Devices with length ratio 1:3 prevent ML and lasing as well due to the absorption being greater than the gain, which disturbs the balance between the shortening and broadening.

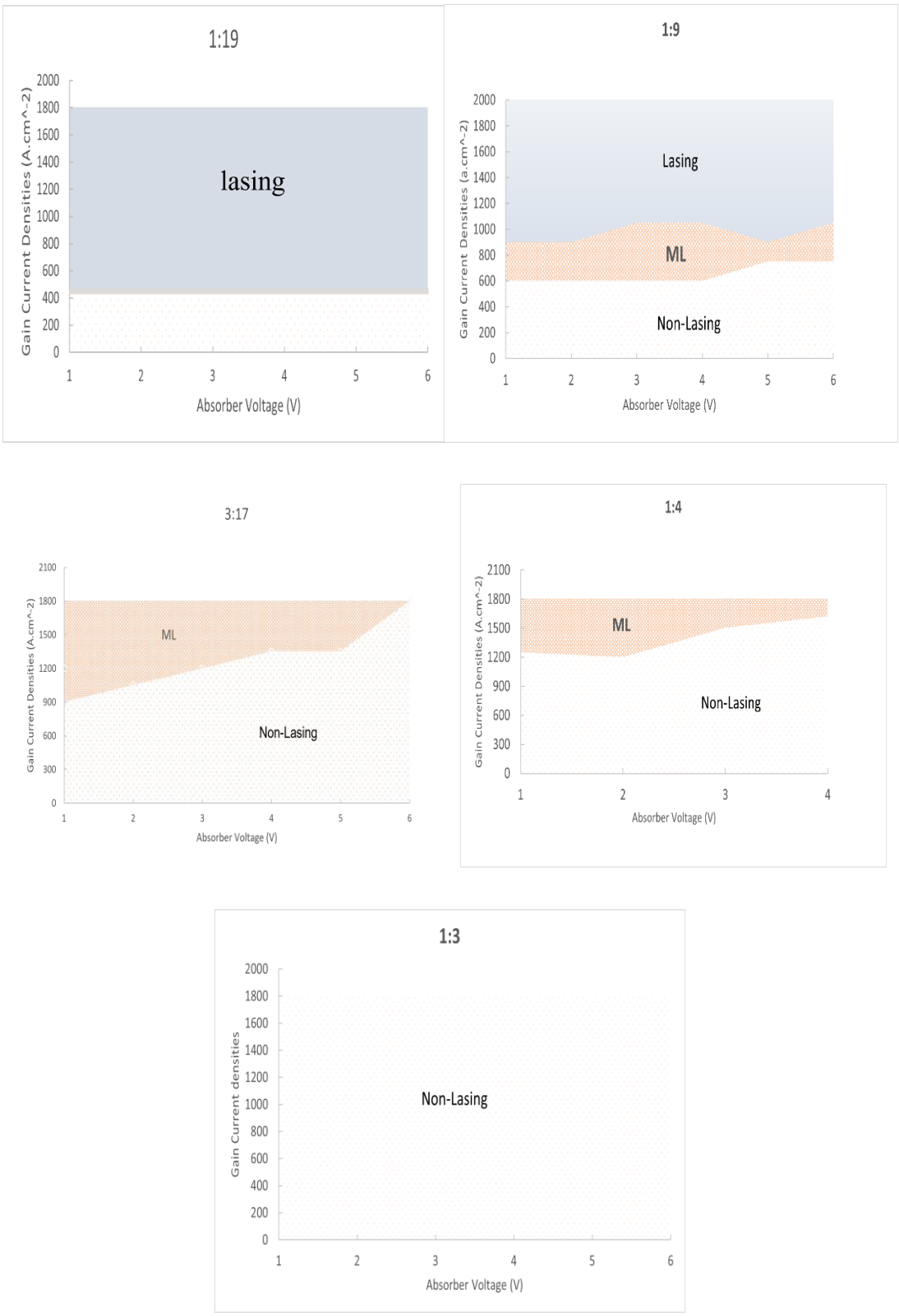


**Figure 5. 14 : The ML operational maps of biases conditions for all the device length ratio designs.**

## 5.7 Peak wavelength and spectral FWHM of Predicted ML pulses

The peak wavelength and spectral FWHM performance of the predicted ML pulses for the range of biases conditions are explored in this section. The peak wavelength and spectral FWHM performance of the predicted ML regimes for all investigated device designs with absorber-to-gain length ratios of 1:4, 3:17 and 1:9, respectively, are plotted in Figure 5.15, Figure 5.16, Figure 5.17, and Figure 5.18. A common observation for all investigated device designs is that the peak wavelengths of ML pulses at a fixed reverse bias slightly shift toward shorter wavelengths with the increase of the gain current density and the spectral FWHM broadens due to the increase of broadening level. Although the shift of the peak wavelengths with the reverse bias and at a fixed gain current density is in a bit higher rate and toward longer wavelengths and the spectral FWHM narrows due to the QCSE (Mark Fox 2010). This behaviour agrees with experimental work that has been done in literature for different QD materials(Thompson et al. 2009).

The peak wavelength of ML pulses for device design 1:4 ranges from 738.7 nm to 742.5 nm for all reverse bias values, corresponding to a FWHM of spectral FWHM from 10.8 nm to 2 nm (see Figure 5.15). The range of peak wavelength of ML pulses for device design 3:17 is between 737.6 nm and 742.6 nm, with FWHM of 9.5 nm and 2.4 nm (see Figure 5.16). The device design with ratio 1:9 has two wavelength range: one at GS from 736.9 nm to 741.9 nm (see Figure 5.17), and the second range at ES start from 724.3 nm to 728.3 nm with FWHM of the GS range between 9.4 nm to 3.9 nm and for the ES between 2.4 nm to 11.1 nm (see Figure 5.18).

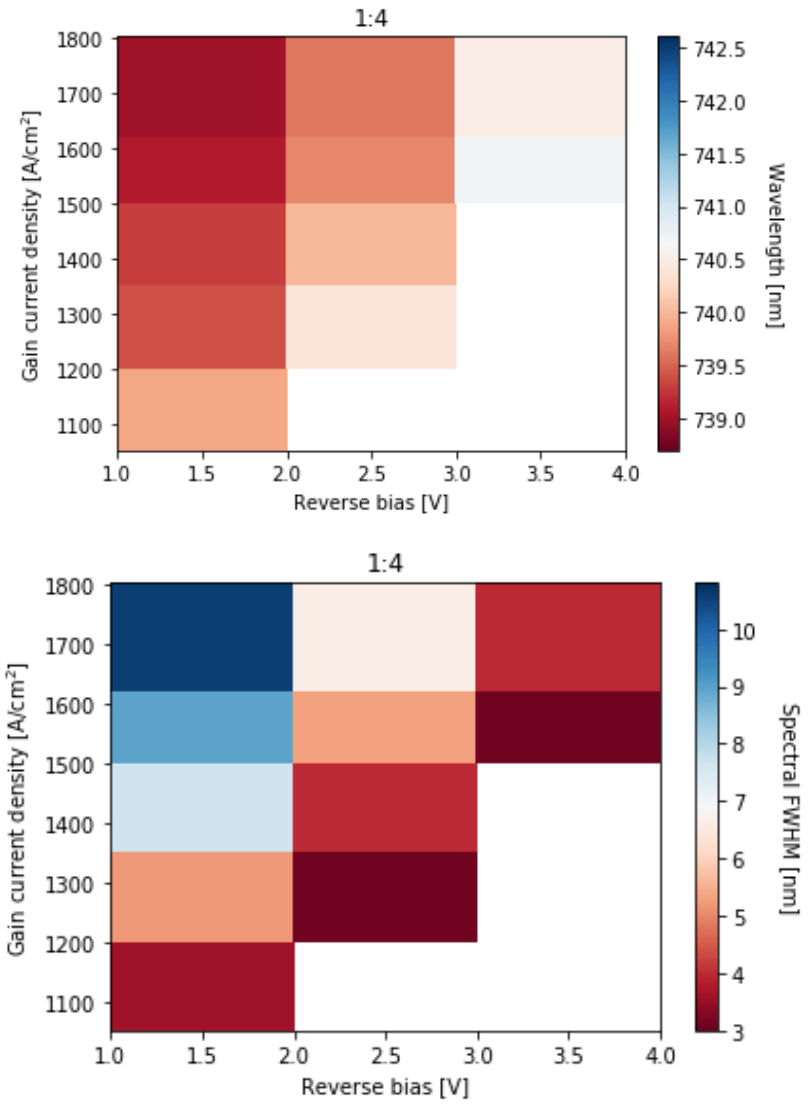


**Figure 5. 15 : The peak wavelength and spectral FWHM of the predicted ML regimes for device length ratio design 1:4 as a function of operating biases conditions (The white area denotes no ML regime region).**

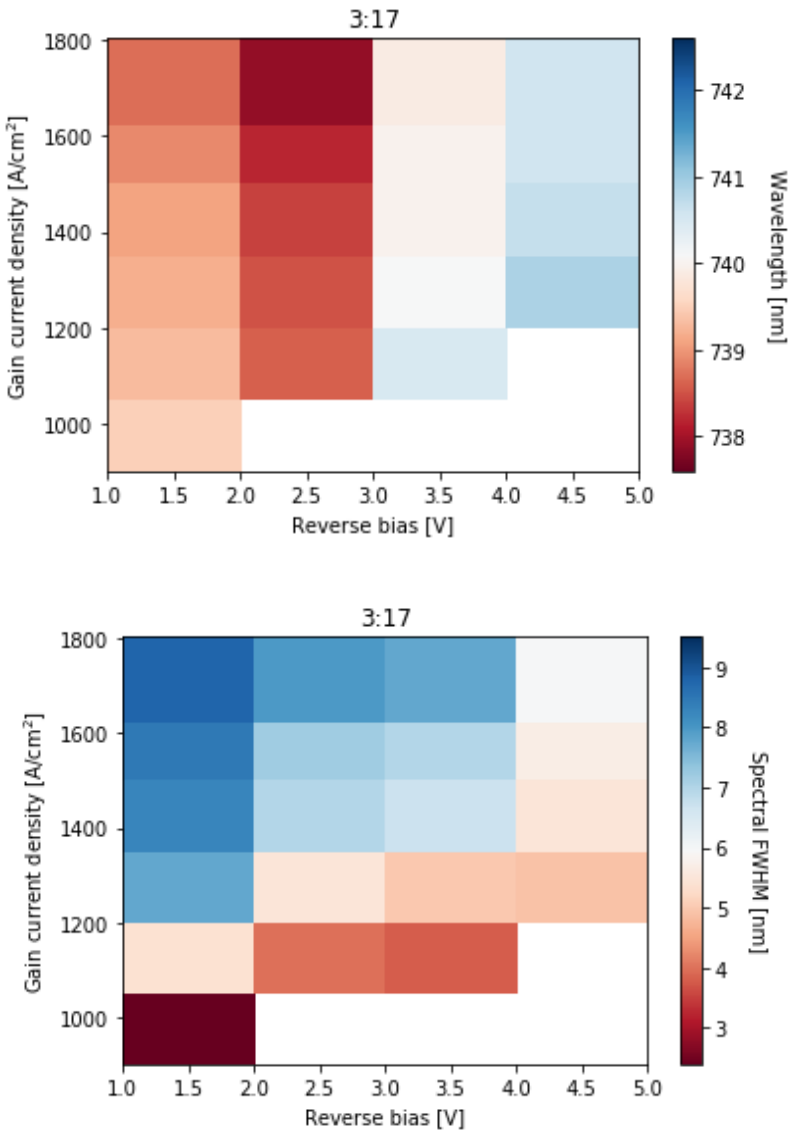


**Figure 5. 16 : The peak wavelength and spectral FWHM of the predicted ML regimes for device length ratio design 3:17 as a function of operating biases conditions (The white area denotes no ML regime region).**

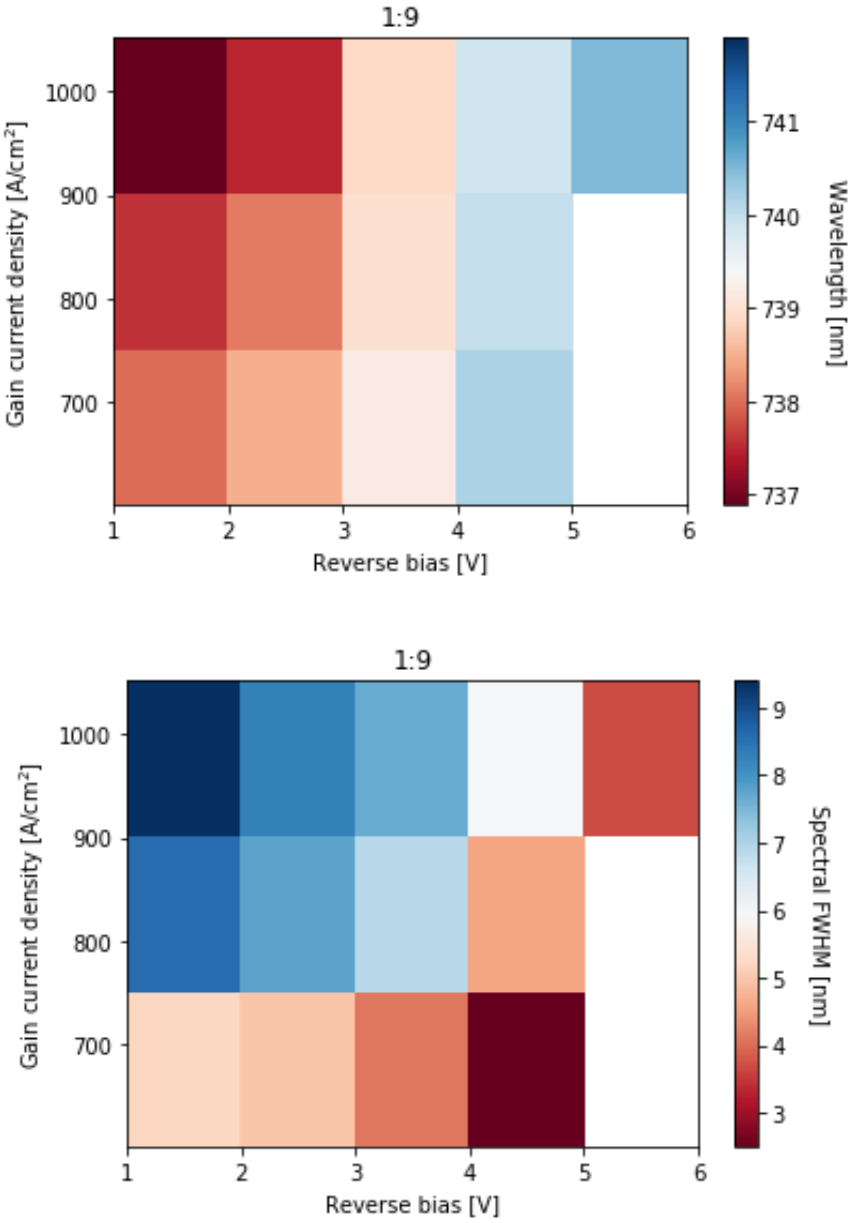


**Figure 5. 17 : The peak wavelength and spectral FWHM of the predicted ML regimes at GS operation for device length ratio design 1:9 as a function of operating biases conditions (The white area denotes no ML regime region).**

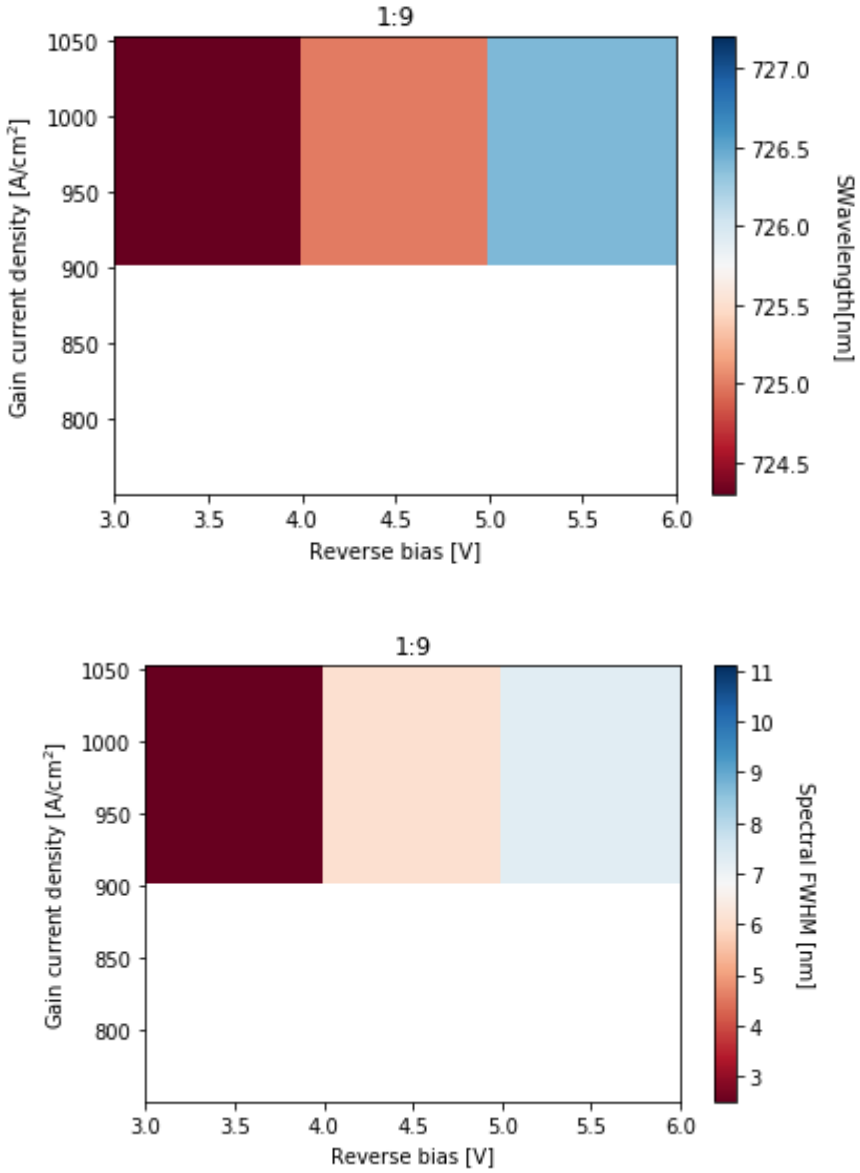


**Figure 5. 18 : The peak wavelength and spectral FWHM of the predicted ML regimes at ES operation for device length ratio design 1:9 as a function of operating biases conditions (The white area denotes no ML regime region).**

## 5.8 Mode-Locking Trends

As we know, the ML pulse characteristics can be determined by three parameters: gain current, reverse bias absorber voltage and absorber-to-gain length ratios. In this section, we present some of the likely ML trends associated with changing these three parameters by plotting different studied correlations. These trends have already been covered adequately in other research work, but for different QD materials and by using experimental methods (Thompson et al. 2009).

### 5.8.1 Current density of gain-section

Figure 5.19 demonstrates the influence of the gain current density on peak wavelength and the spectral FWHM of each wavelength peak at a fixed reverse bias of 2 V and fixed absorber-to-gain length ratio of (1:4). It is clear that the increase of the gain current density broadens the spectral width and shifts the peak wavelength slightly toward shorter wavelengths. This shift is attributed to the increase of broadening due to the filling of the lower energy level states and the transition to the higher energy levels. However, the reverse bias decreases this energy shift rate due to the effect of absorption. In addition to the increase of the broadening, the gain amplitude also increases with the increase of gain current density. This trend has been observed for other QDs MLLs (Thompson et al. 2009). This could lead us to conclude that the increase of the gain current density could improve the device performance in terms of output power due to the increase of gain amplitude.

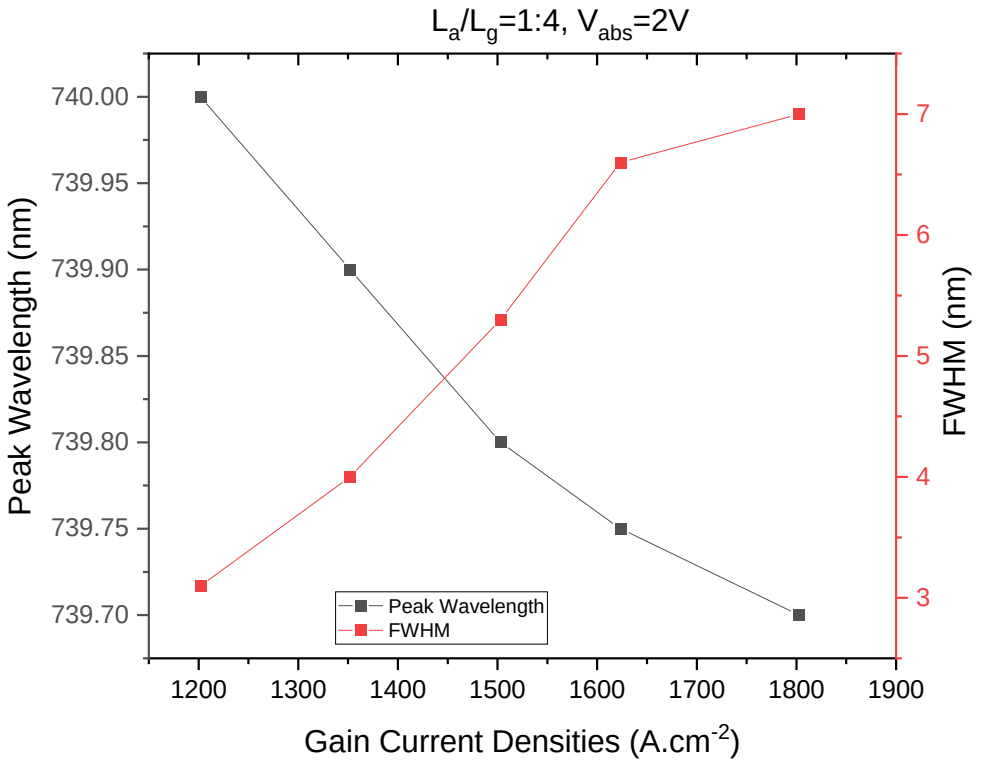


**Figure 5. 19 : The peak wavelength and the spectral FWHM versus the gain current density for device length ratio 1:4 and at fixed reverse bias 2 V.**

### 5.8.2 Reverse bias of absorber section

Figure 5.20 illustrates the impact of the reverse bias on operating wavelength and FWHM of spectral width at fixed gain current density 1803 A.cm$^{-2}$ and device design with ratio (1:4). Increasing the reverse bias absorber voltage shifts the peak wavelength toward a longer wavelength because of the drift of the band gap due to QCSE (Mark Fox 2010). The spectral FWHM corresponding to these wavelengths narrow with the increase of reverse bias due to the higher sweep-out rate of the carriers, thus decreasing the absorption recovery time and creating the pulse shaping formation (Williams et al. 2004). Consequently, less broadening and, as a result, shorter pulses could be achieved. Additionally, the reverse bias causes a reduction in gain amplitude and consequently the output power. Therefore, the ML trend regarding the application of reverse bias is shifting the wavelength toward longer, less broadening, more

shortening, better shaping performance and shorter pulse duration, but with low output power.

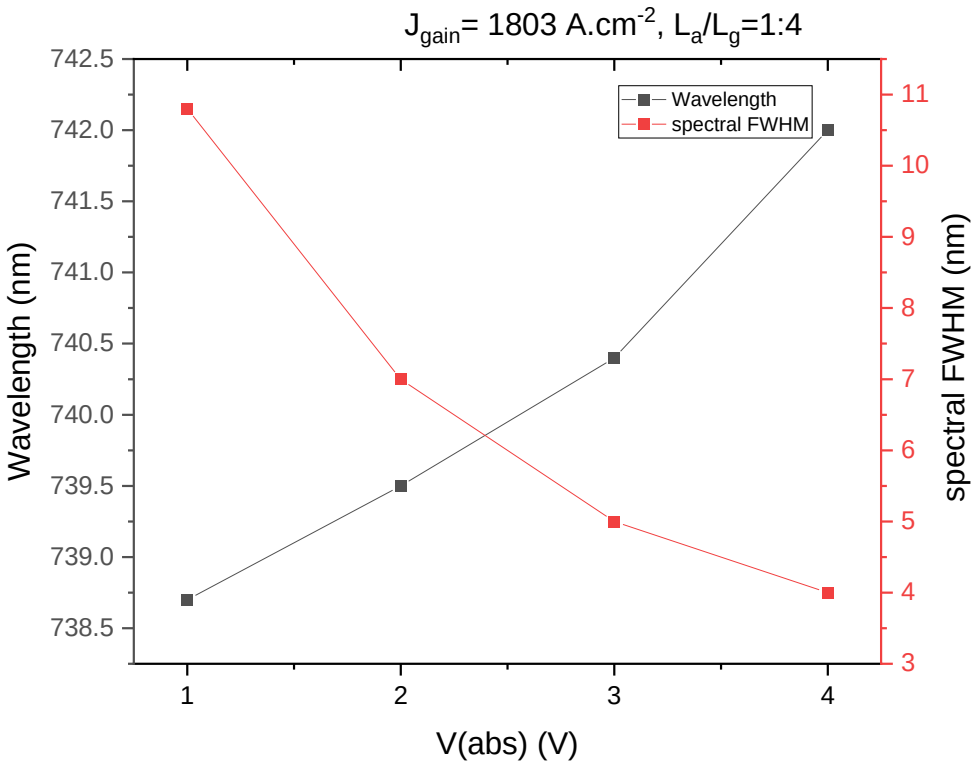


**Figure 5. 20 : The peak wavelength and the spectral FWHM versus the reverse bias for device length ratio (1:4) and at fixed gain current density 1803 A.cm$^{-2}$.**

### 5.8.3 Absorber-to-gain length ratio

The effect of absorber-to-gain length ratio plays an important role in shaping performance. Figure 5.21 shows the effect of absorber-to-gain length ratio on the operating wavelength and FWHM of spectral width at a fixed reverse bias of 4 V and at the highest gain current density that could generate ML pulse identified in the range of ML regime in Section 5.6. The FWHM decreases, and the operating wavelength shifts toward longer wavelengths with the increase of the SA length. Increasing the SA length will enhance the device performance in terms of chirping performance. The increase in SA length might result in pulse shortening due to the increasing saturable absorption encountered by the pulse as it propagates through the long SA section.

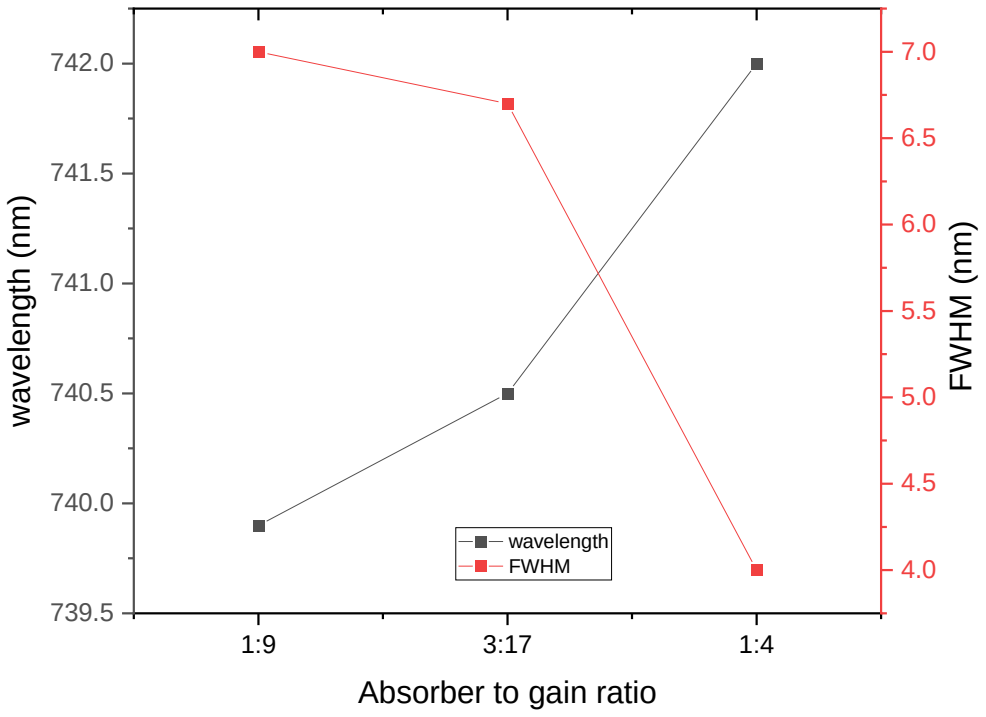


**Figure 5. 21 : The peak wavelength and the FWHM versus the reverse bias for the highest gain current density produced ML pulse and at fixed gain reverse bias 4 V.**

## 5.9 Conclusion

In this chapter, we have provided a detailed review of our semi-empirical approach to understanding the performance of passively monolithic MLLs. The net modal gain of InP QDs MLLs was predicted for different gain current density, reverse bias voltage and for various absorber-to-gain length ratios. The threshold current density were estimated for the studied device designs and the whole set of reverse bias voltages. The bias conditions operational map, the operating wavelength and the FWHM of the spectral width were predicted for all device length ratio designs. In addition, ML trends at gain current density, reverse bias voltage and length ratios were investigated.

Device designs with ratios 1:4, 3.17 and 1:9 were predicted to generate ML pulses in different circumstances. Device designs with ratios 1:4 and 3.17 were predicted to

achieve stable ML pulses at high injected current density above 1202 A.cm$^{-2}$ of 1:4 at a range of reverse bias voltages from 1 V to 4 V and above 901.9 A.cm$^{-2}$ of 3:17 for reverse bias voltage between 1 V to 5 V. The device design with ratio 1:9 was predicted to generate ML pulses at lower gain current density between 601 A.cm$^{-2}$ and 1052 A.cm$^{-2}$ at the full range of the investigated reverse bias voltages (1 V to 6 V). At higher current density than 1052 A.cm$^{-2}$, the device will only lase. However, the most interesting finding is that device with design absorber-to-gain length ratio 1:9 could generate two ML pulses in the GS and ES. The device designed with the longest absorber section 1:3 was predicted to not provide ML or lasing, whereas a device design with the shorter absorber section 1:9 does not offer any significant ML performance benefits but does have lasing benefits.

Gain current density shift the wavelengths toward a shorter wavelength (blue-shift), whereas reverse bias voltages shift them toward a longer wavelength (red-shift). The ranges of the operating wavelength of ML pulses are as follows: 738.7 nm to 742.5 nm for device design 1:4, 737.6 nm to 742.6 nm for 3:17 and two ranges for 1:9; GS range from 736.9 nm to 741.9 nm and ES range from 724.3 nm to 728.3 nm.

Significant improvements in pulse shaping are observed after modifying the SA length. The studied device designs provide the shortest pulse duration at different reverse bias voltage. The shortest pulses predicted for device designs 1:4, 3:17 and 1:9 were at reverse bias conditions 1 V, 1 V and 6 V with FWHM 10.8 nm, 9.5 nm and 11.1 nm, respectively.

In conclusion, this semi-empirical approach allows a more complete understanding of the performance of an InP QD passively monolithic MLL in terms of spectral perspective. With this knowledge, future InP QD MLL devices can be designed to generate ML pulses with a shorter pulse width and high output power. This investigation considered the bias conditions, the total length of the cavity, the SA section length, and the gain section length. However, the approach did not take into account the width of ridge MLL. Therefore, further investigations are required to include the width of ridge MLL.

## References

Brown, K., Fanto, M., Murrell, D., Kovanis, V., Xin, Y.-C. and Lester, L.F. 2007. Automated analysis of stable operation in two-section quantum dot passively mode locked lasers. In: *Physics and Simulation of Optoelectronic Devices XV*. SPIE, p. 64681M. doi: 10.1117/12.710845.

Derickson, D.J., Helkey, R.J., Mar, A., Karin, J.R., Wasserbauer, J.G. and Bowers, J.E. 1992. Short Pulse Generation Using Multisegment Mode-Locked Semiconductor Lasers. *IEEE Journal of Quantum Electronics* 28(10), pp. 2186–2202. doi: 10.1109/3.159527.

Haus, H.A. 2000. Mode-locking of lasers. *IEEE Journal on Selected Topics in Quantum Electronics* 6(6), pp. 1173–1185. doi: 10.1109/2944.902165.

Malins, D.B., Gomez-Iglesias, A., White, S.J., Sibbett, W., Miller, A. and Rafailov, E.U. 2006. Ultrafast electroabsorption dynamics in an InAs quantum dot saturable absorber at 1.3 μm. *Applied Physics Letters* 89(17). doi: 10.1063/1.2369818.

Mark Fox 2010. *Optical Properties of Solids*. second edition. Fox. Mark ed. New York: Oxford University Press.

Mee, J.K., Raghunathan, R., Wright, J.B. and Lester, L.F. 2014. Device geometry considerations for ridge waveguide quantum dot mode-locked lasers. *Journal of Physics D: Applied Physics* 47(23). doi: 10.1088/0022-3727/47/23/233001.

Peter Blood 2015. *quantum confined laser devices*. First edition. Blood, P. ed. New York: Oxford University press.

Rafailov, E.U. and Avrutin, E. 2013. Ultrafast pulse generation by semiconductor lasers. In: *Semiconductor Lasers: Fundamentals and Applications*. Elsevier Ltd, pp. 149–217. doi: 10.1533/9780857096401.1.149.

Thompson, M.G. et al. 2004. Transform-limited optical pulses from 18 GHz monolithic modelocked quantum dot lasers operating at ∼1.3 [micro sign]m. *Electronics Letters* 40(5), p. 346. doi: 10.1049/el:20040220.

Thompson, M.G. et al. 2006. Subpicosecond high-power mode locking using flared waveguide monolithic quantum-dot lasers. *Applied Physics Letters* 88(13). doi: 10.1063/1.2186110.

Thompson, M.G., Rae, A.R., Xia, M., Penty, R. v. and White, I.H. 2009a. InGaAs quantum-dot mode-locked laser diodes. *IEEE Journal on Selected Topics in Quantum Electronics* 15(3), pp. 661–672. doi: 10.1109/JSTQE.2008.2012265.

Thompson, M.G., Rae, A.R., Xia, M., Penty, R. v. and White, I.H. 2009b. InGaAs quantum-dot mode-locked laser diodes. *IEEE Journal on Selected Topics in Quantum Electronics* 15(3), pp. 661–672. doi: 10.1109/JSTQE.2008.2012265.

Williams, K.A., Thompson, M.G. and White, I.H. 2004. Long-wavelength monolithic mode-locked diode lasers. *New Journal of Physics* 6, pp. 1–30. doi: 10.1088/1367-2630/6/1/179.

# Chapter 6:

# Mapping the performance of InAsP QD monolithic passively MLLs

## 6.1 Introduction

In Chapter 4, it has been concluded that InAsP QD materials can generate shorter ML pulses than InP QDs. This chapter will investigate the performance of passively monolithic InAsP QDs MLLs using the novel semi-empirical approach we have used for InP QDs in Chapter 5. The investigated areas involve the net MLL gain for different gain-section current density at fixed reverse-bias voltage starting from 1 V to 6 V and for different device designs in terms of absorber-to-gain length ratios, which are 1:19, 1:9, 3:17 and 1:4 for a device with total cavity length of 3 mm. Additionally, the threshold current density will be investigated as a function of different reverse-bias voltages and absorber lengths. The operational map of the bias conditions, the lasing wavelengths and the ML pulses' spectral FWHM are predicted. Furthermore, the ML trends at fixed gain-section current density, fixed reverse bias and fixed device design in terms of absorber-to-gain length ratios are studied. The approach will aid in designing the most reliable device with the shortest ML pulses obtained from InAsP QD material and offer a priori insight into what limits performance.

## 6.2 Semi-empirical approach

Figure 6.1 illustrates the shape of the predicted net MLL modal gain of InAsP QDs at fixed gain-section current density of 1667 A.cm$^{-2}$, fixed reverse-bias voltage of 3 V, and for different studied device designs with absorber-to-gain length ratios of 1:19, 1:9, 3:17 and 1:4 for a MLL with total cavity length of 3 mm. Unlike the shape of net MLL modal gain of InP QDs, no absorption peak is obvious here and this could be attributed to the irregular distribution of InAsP dots' sizes. The added absorption

reduces the gain amplitude and narrows the net MLL gain bandwidth. However, similar to the criterion used for InP QDs, which was discussed in Chapter 5, Section 5.2, it has been assumed that the net MLL modal gain curves must be at the threshold level (the level of gain requirement) for the device to be in the ML regime. Any net MLL modal gain curves that are above the threshold from 0 $cm^{-1}$ to approximately 2 $cm^{-1}$ could be considered in ML regime due to the fact that additional gain is required to overcome the losses (Rafailov et al. 2013). Therefore, all the net MLL modal gain curves in the Figure 6.1 are predicted to produce ML pulses. The red vertical dashed lines represent the change of gain peaks with the variation of absorber-to-gain length ratios.

.

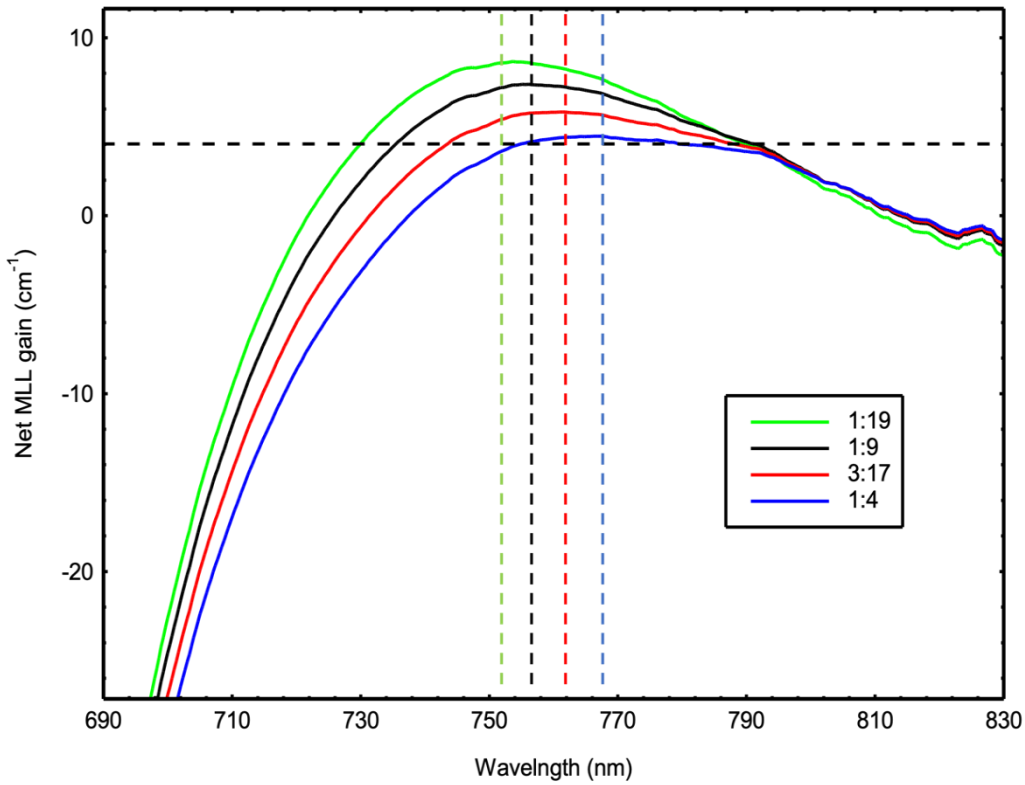


**Figure 6. 1: Net MLL gain as a function of wavelengths for all investigated absorber-to-gain length ratios at fixed gain-section current density 1667 A.cm-2 and fixed reverse bias of SA-section 3 V.**

## 6.3 Characterisation of net MLL modal gain

The predicted net InAsP MLL modal gain of device designs with absorber-to-gain length ratios of 1:19, 1:9, 3:17 and 1:4 are demonstrated in Figures 6.2, 6.3, 6.4 and 6.5, respectively. The

net MLL gain is predicted for a gain current density range of (95 $A.cm^{-2}$– 1667 $A.cm^{-2}$) under a fixed reverse bias ranging from 1 V– 6 V. Similar to the net MLL modal gain versus current density of InP QDs, which were plotted in Chapter 5, Section 5.3, these figures show that as the current density increases, the gain peak amplitudes and widths increase accordingly. This increase eventually saturates at a high current density, which is attributed to the filling of the states due to the inhomogeneous distribution of sizes of the QDs (Blood, 2015). A similar pattern is seen for all the net MLL modal gain curves for each fixed reverse bias condition.

In line with the findings from InP QDs, investigated in Chapter 5, a blue-shift occurred with the increase of gain current density, and a red-shift occurred with the increase of reverse bias. For example, the blue-shift of the wavelength peak of the device with a device ratio of 1:19 ranges from 770 nm at 95 $Acm^{-2}$ to 750 nm at 1667 $Acm^{-2}$. The blue-shift of wavelength peak changes for other device designs under the same conditions as reported in Table 6.1. The gain amplitude of the device design with a ratio of 1:19 is saturated at approximately 8.5 $cm^{-1}$ at the highest gain current density and a fixed reverse bias of 1 V. For other device designs under the same conditions, the saturation level of device designs 1:9, 3:17 and 1:4 are at 7.9 $cm^{-1}$, 6.6 $cm^{-1}$ and 5 $cm^{-1}$, respectively. The peak wavelength ranges for each device design indicate that the blue-shift rate and saturation level decrease with increasing SA length due to the shortening effect caused by the absorption of the SA section. The reduction of the gain peak increases with the increase of reverse-bias voltage of SA. This reduction is further reduced in devices with a longer SA section. In more detail, switching the SA reverse bias for the device design with the shortest absorber section lengths 1:19 and 1:9 slightly affects the gain amplitude. The effect starts to become more obvious for device designs with longer absorber sections 3:17 and 1:4. In addition to the reduction of the gain amplitude, the peak wavelengths, the spectral FWHM and shaping performance are affected as well.

**Table 6. 1: Blueshift and redshift wavelength ranges for the studied absorber-to-gain length ratios at fixed 1 V (blue-shift) and fixed gain-section current density of 857A.cm$^{-2}$ (red-shift).**

| Absorber-to-gain length ratios | Blue-shift wavelength range (nm) | Red-shift wavelength range (nm) |
|---|---|---|
| **1:19** | 750-770 | 760-763.4 |
| **1:9** | 755-774 | 767-769 |
| **3:17** | 759-777 | 771-774.9 |
| **1:4** | 763-780 | 779-777.7 |

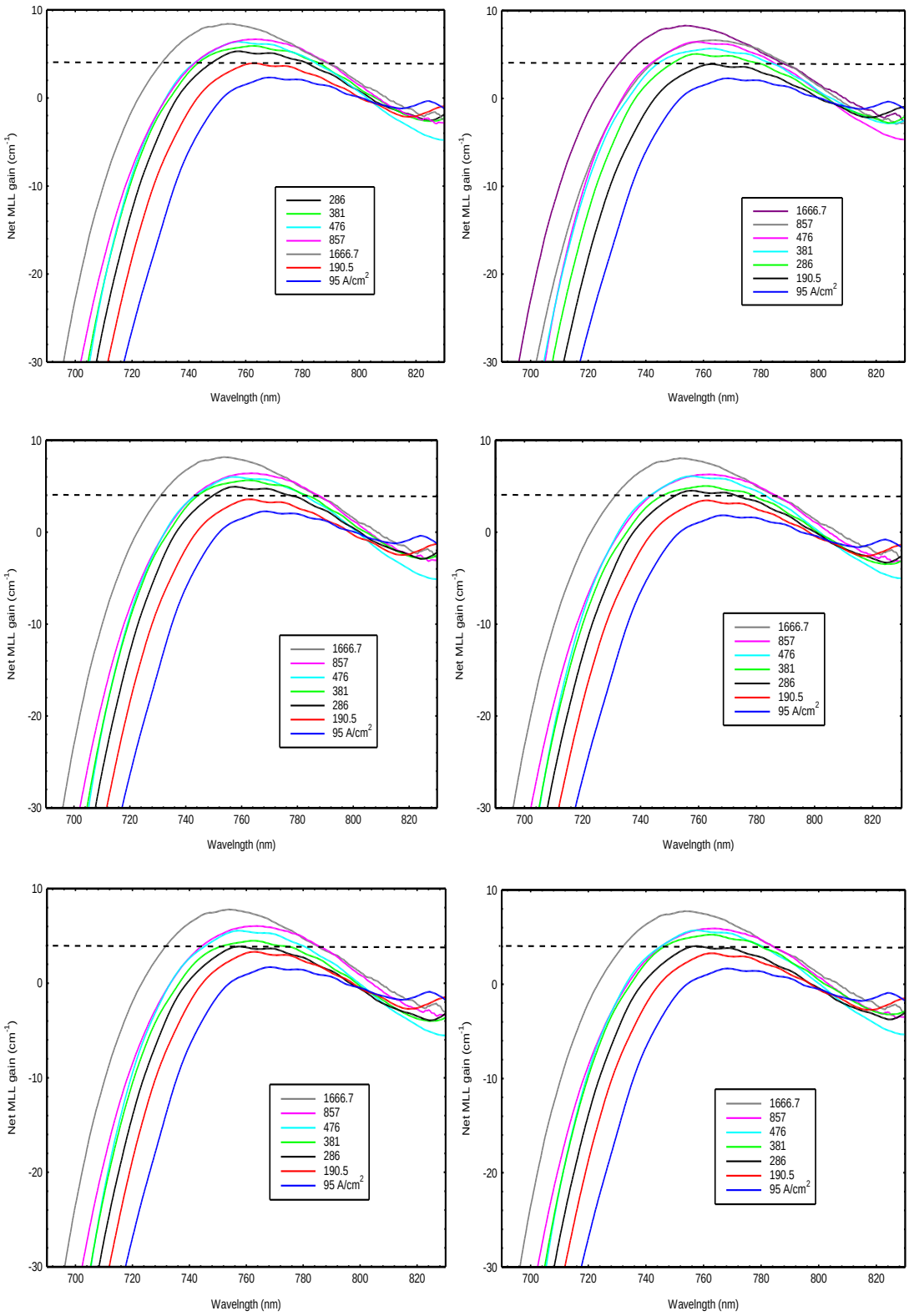


**Figure 6. 2: The net MLL modal gain of a device design with absorber-to-gain length ratio of (1:19) at various fixed reverse bias (1 V, top left–6 V, bottom right) (The dashed line on the graphs represents the gain requirement).**

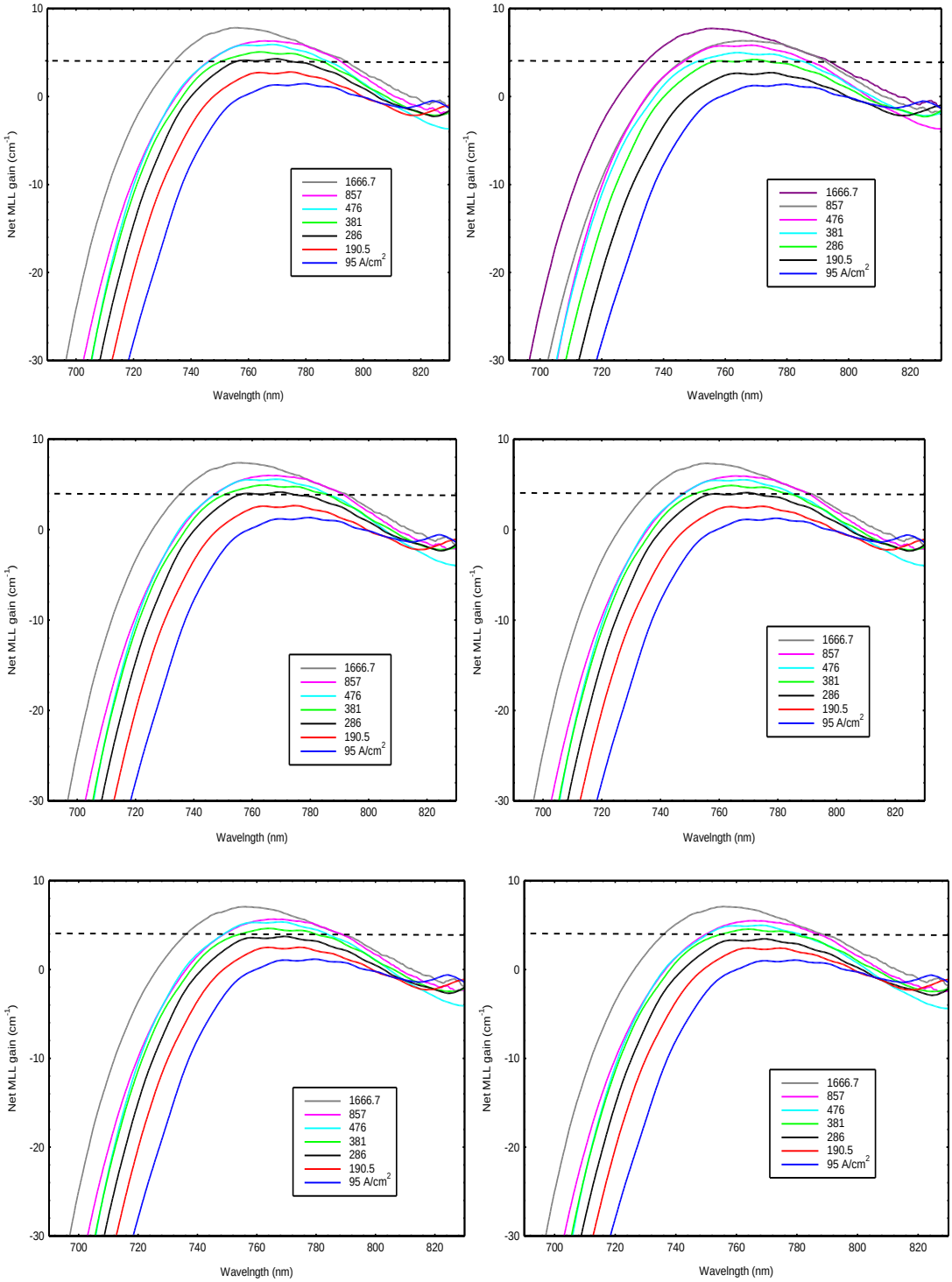


**Figure 6. 3: The net MLL modal gain of a device design with absorber-to-gain length ratio of (1: 9) at various fixed reverse bias (1 V, top left–6 V, bottom right) (The dashed line on the graphs represents the gain requirement).**

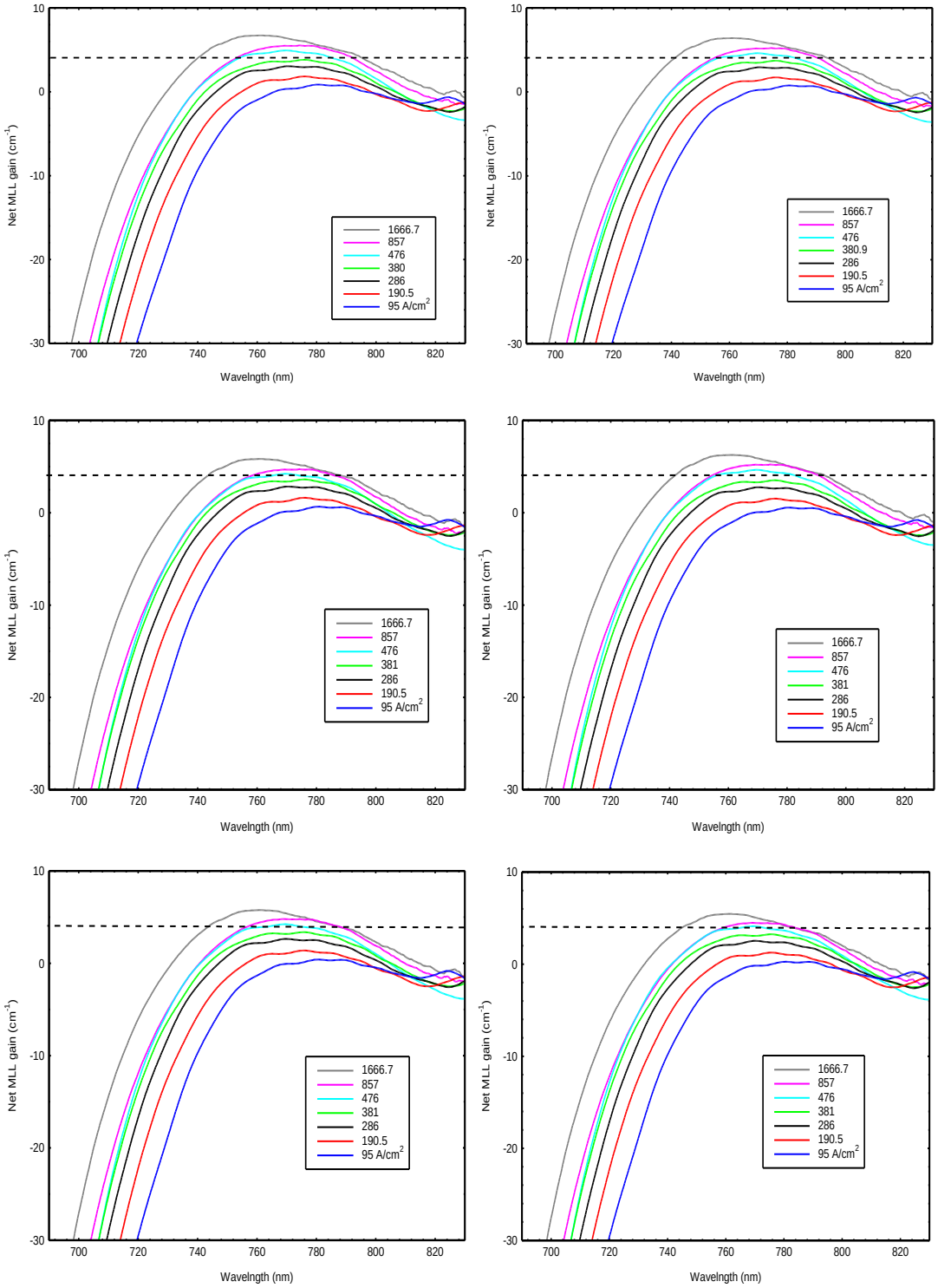


**Figure 6. 4: The net MLL modal gain of a device design with absorber-to-gain length ratio of (3:17) at various fixed reverse bias (1 V, top left–6 V, bottom right) (The dashed line on the graphs represents the gain requirement).**

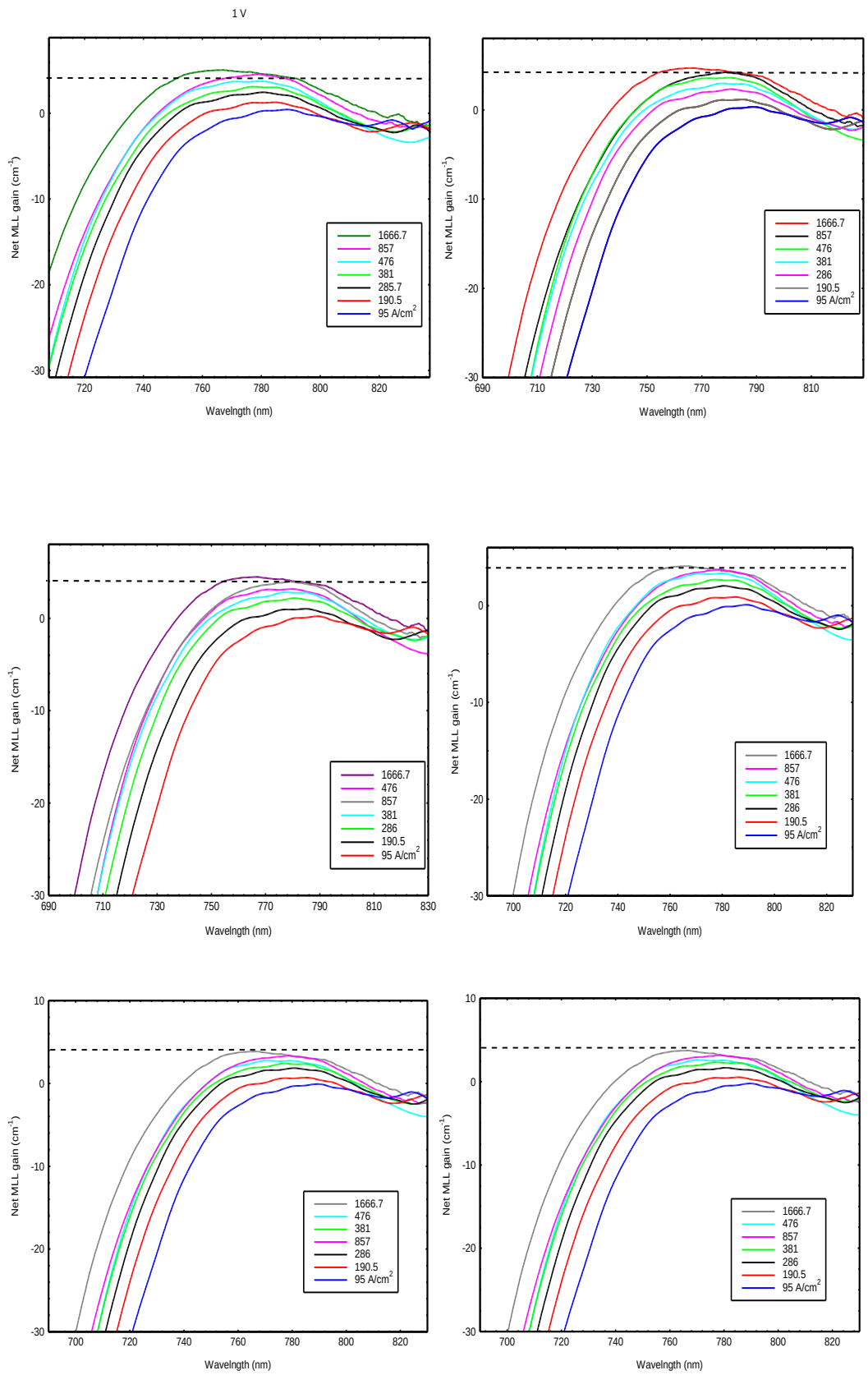


**Figure 6. 5: The net MLL modal gain of a device design with absorber-to-gain length ratio of (1:4) at various fixed reverse bias (1 V, top left–6 V, bottom right) (The dashed line on the graphs represents the gain requirement).**

Compared to the previously reported net modal gain characteristics of a laser device without a passive waveguide section mentioned in Chapter 4, Section 4.3, the gain amplitude is reduced by 4.5 $cm^{-1}$ at the highest gain-section current density for device design with a ratio of 1:19, and by 8 $cm^{-1}$ for the device design of the ratio with the longest SA length 1:4. Furthermore, the blue-shift rate decreases as the absorber length increases. However, this decrease in blue-shift rate is much lower than the decrease in those rates for InP QDs presented in Chapter 5, Section 5.3. The reason behind these differences is attributed to the differences in the shape of both materials' absorption.

## 6.4 Characteristic of gain-current relation

This section examines the effect of absorber section length and increasing reverse-bias voltages of SA on net differential MLL modal gain and, accordingly, on gain saturation and threshold current density. Figures 6.6, 6.7, 6.8 and 6.9 demonstrate the gain-current curves for different ML devices with different absorber-to-gain length ratios of 1:19, 1:9, 3:17 and 1:4, respectively. The device design with the shorter SA length 1:19 and 1:9 demonstrates a moderate effect on the net differential modal gain and, consequently, on the gain saturation and threshold current density. Interestingly, these parameters significantly impact the devices with longer SA-sections 3:17 and 1:4. The impact becomes more noticeable with the increase in the absorber section length and the increase in the reverse bias voltage. The net differential MLL modal gain is linked to the blue shift ranges listed in Table 6.1. It was apparent that the decrease in blue shift ranges coincided with the increase in the SA section length. This verifies the effect of absorber section length on the net differential MLL modal gain and, therefore, on the gain saturation and ML stability condition. Moreover, applying a reverse-bias to all device designs reduces the differential gain in the gain regime. however, the differential gain remains higher in the absorption regime, which offers faster gain saturation. Overall, all studied device designs fulfil the ML stability condition.

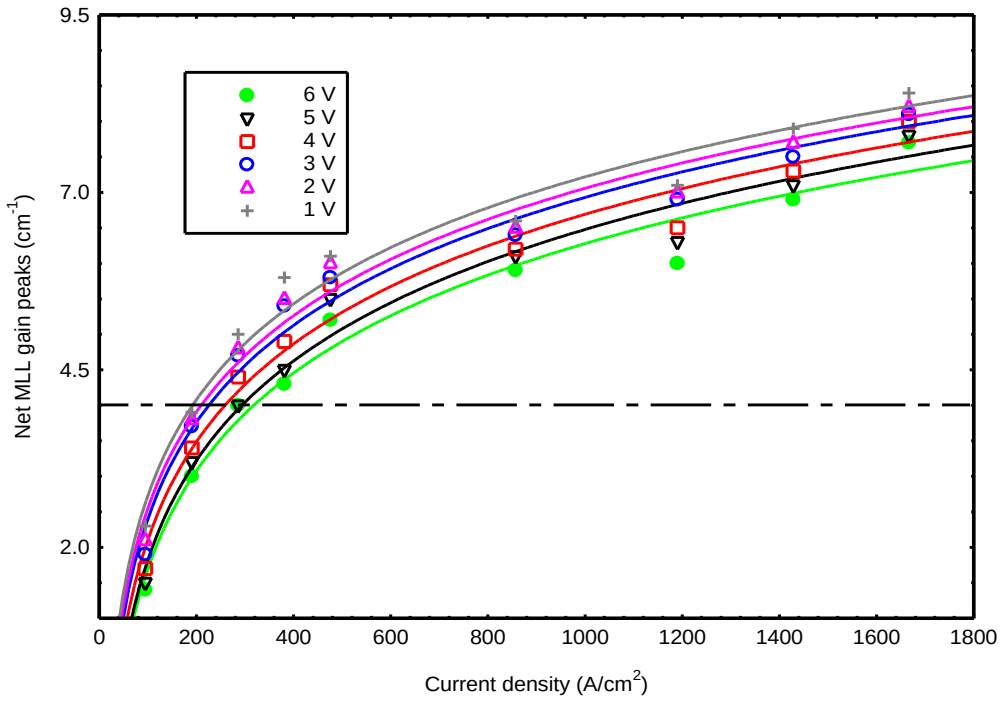


**Figure 6. 6: the gain-current curve of device design 1:19 as a function of current density and for various fixed reverse bias conditions (1 V–6 V) ) (Uncertainty values =gain peaks ± 1.3).**

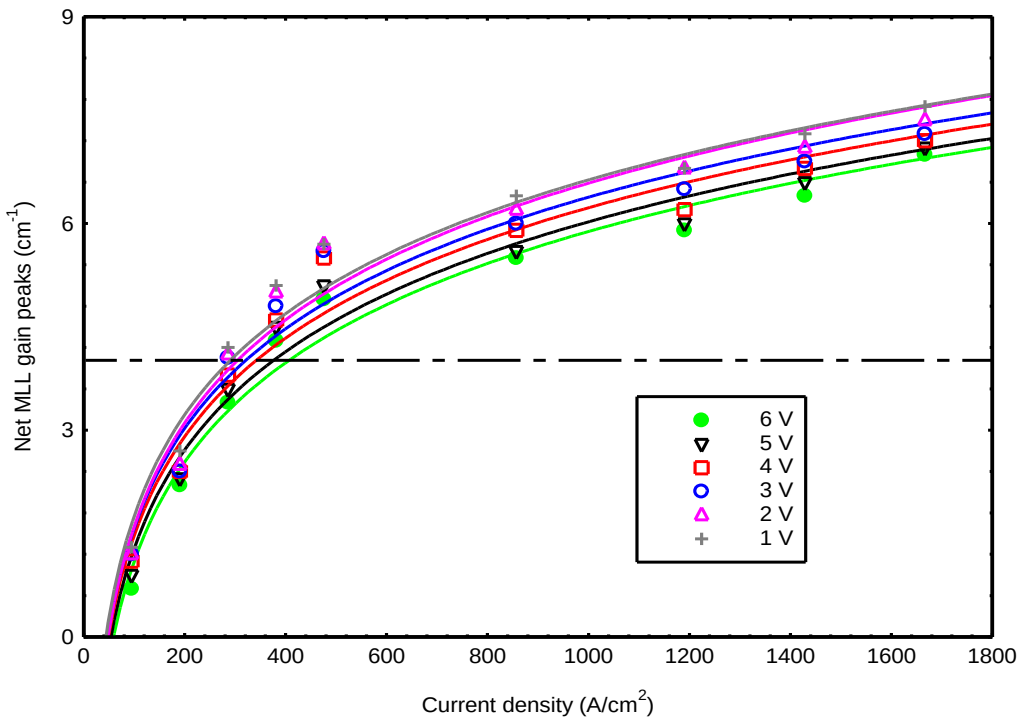


**Figure 6. 7: the gain-current curve of device design 1:9 and as a function of current density and for various fixed reverse bias conditions (1 V–6 V) (Uncertainty values =gain peaks ± 1.3).**

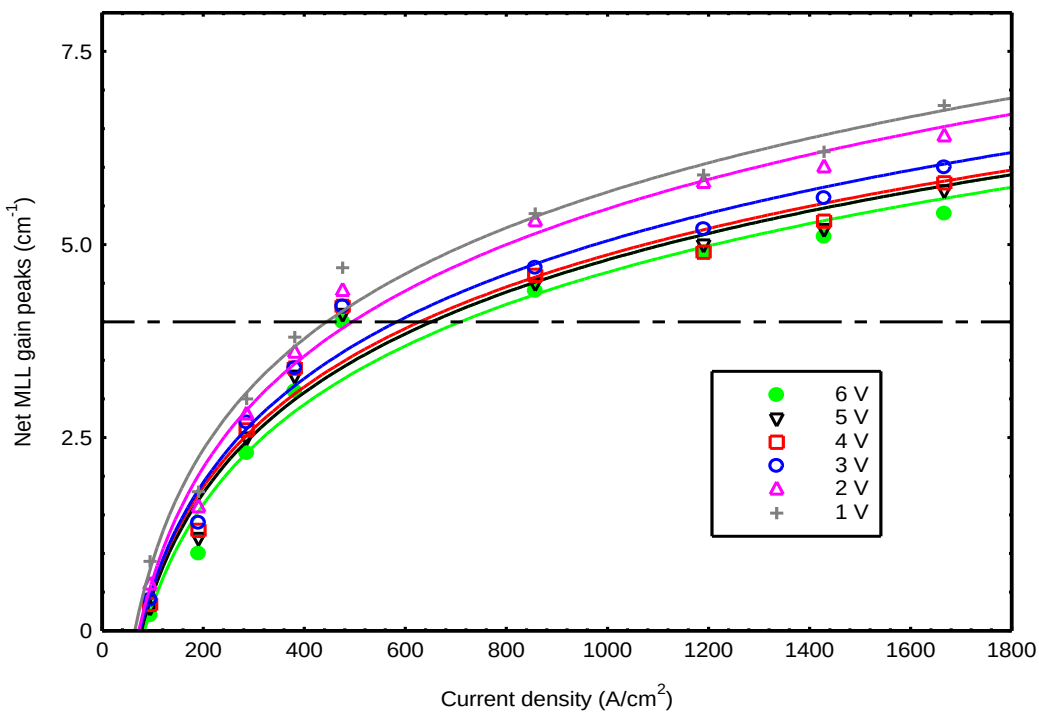


**Figure 6. 8: the gain-current curve of device design 3:17 as a function of current density and for various fixed reverse bias conditions (1 V–6 V) (Uncertainty values =gain peaks ± 1.3).**

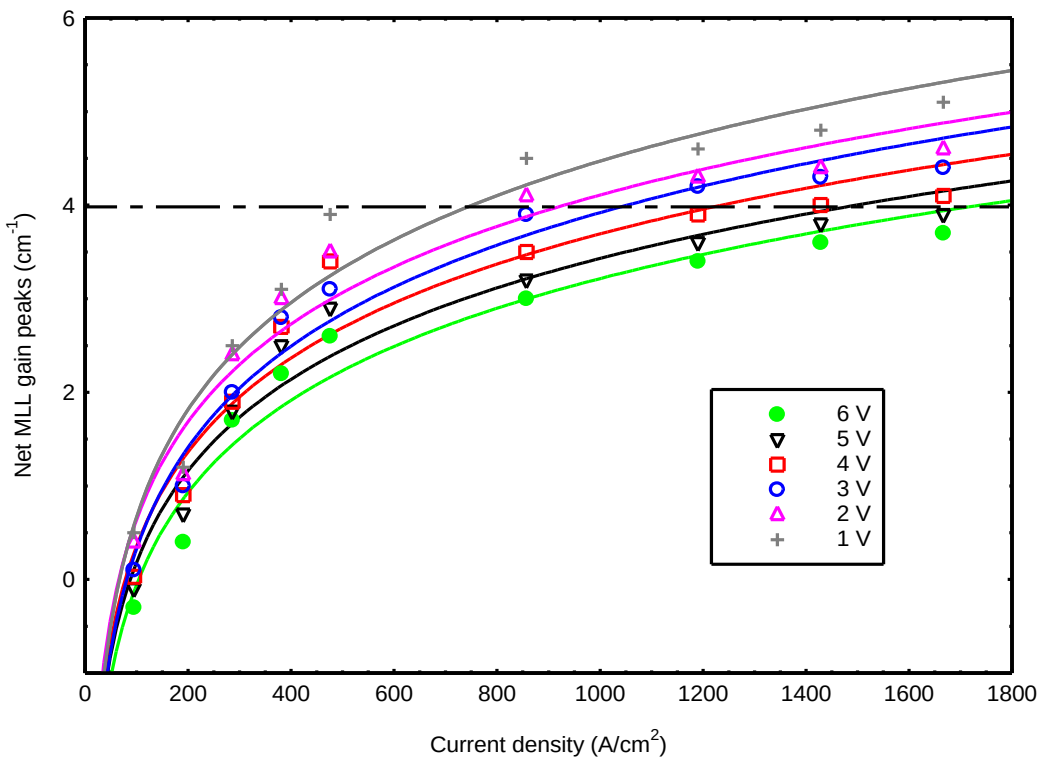


**Figure 6. 9: the gain-current curve of device design 1:4 as a function of current density and for various fixed reverse bias conditions (1 V–6 V) (Uncertainty values =gain peaks ± 1.3).**

Table 6.2. displays the threshold current density for all device designs and reverse-bias conditions (all devices are 3mm long). Compared to the InAsP QD laser device reported in Chapter 4, Section 4.4, the threshold current density of device design with ratio of 1:19 has been pushed towards much higher values of threshold current density.. The threshold current density increased to 194 A.cm$^{-2}$ at the lowest reverse-bias (1 V) for the shortest SA-section length (device design 1:19), and to a much higher value of 741.8 A.cm$^{-2}$ under the same reverse-bias condition for device designs with longer SA-section length. This is due to the increased absorption in the longer absorber section and due to the increase of non-radiative recombination.

**Table 6. 2: Threshold current density for all studied absorber-to-gain length ratios and at fixed reverse bias ranged between (1 V– 6 V) – all have 3mm total device length.**

| **Reverse-bias (V)** | **Threshold Current Density (A.cm$^{-2}$)** | | | |
|---|---|---|---|---|
| | 1:19 | 1:9 | 3:17 | 1:4 |
| **1** | 194 | 284 | 443 | 741.8 |
| **2** | 213 | 299 | 501 | 910 |
| **3** | 228 | 324 | 584 | 1038 |
| **4** | 252 | 342 | 619 | 1206 |
| **5** | 294 | 365 | 661 | - |
| **6** | 322 | 398 | 726 | - |

## 6.5 Influence of reverse-bias and SA-section length on threshold current density

The preceding sections' assessment of gain-section current density reveals a considerable correlation between the length of the SA-section and the extent to which reverse-bias voltage affects threshold current density. The reverse-bias voltages' effect becomes more significant with a longer absorber section. Figure 6.10 shows the effect of the SA length of a passive MLL on the threshold current density for different SA reverse bias voltages between 0 V and 6 V. The level of the threshold current density increases as the SA length increases because the longer SA-section would need higher gain-section current density for gain to compensate. Therefore, the length of the SA-section governs the effect of reverse bias SA voltage on threshold current density.

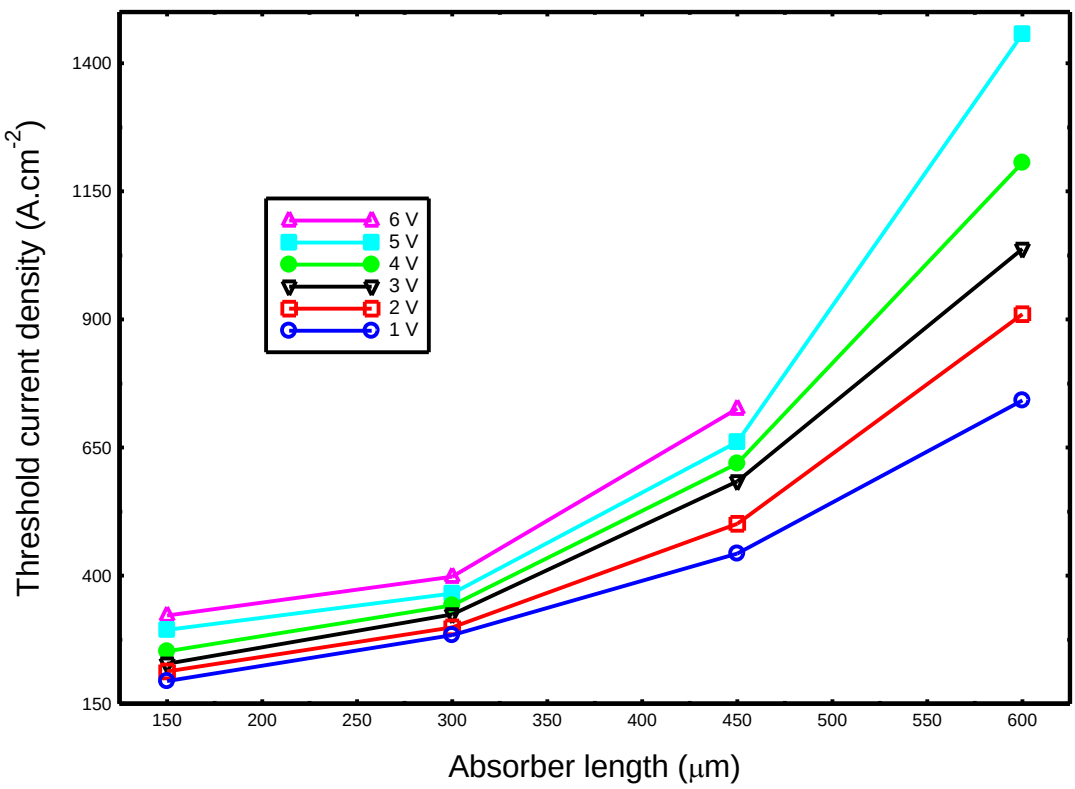


**Figure 6. 10: The threshold current density as a function of SA-section length for various reverse bias conditions (1 V– 6 V).**

Figure 6.11 demonstrates the threshold current density dependence on the reverse-bias voltage in the range of 1 V– 6 V for different investigated absorber-to-gain length

ratios of a passive MLL. The effect of reverse bias is relatively low for the shortest absorber lengths but becomes considerable as SA-section length increases. Mode-locking behaviour with SA-section lengths higher than 600 μm for a 3 mm total cavity length laser is shown to be challenging in this material.

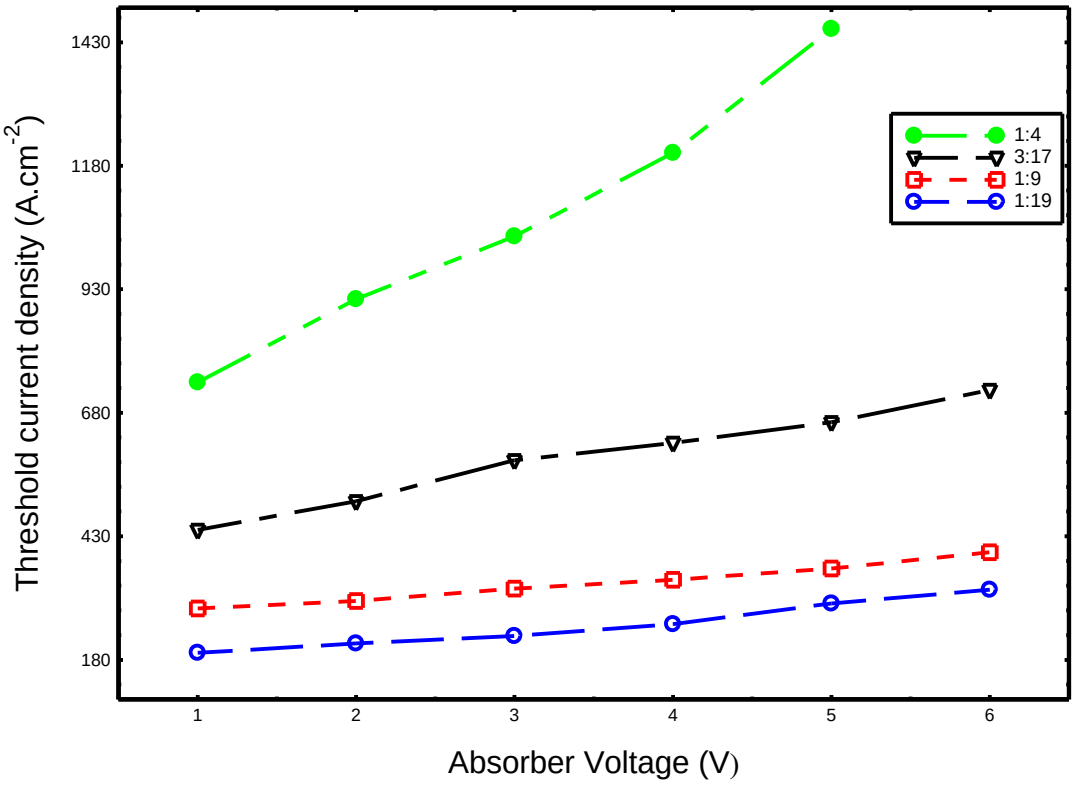


**Figure 6. 11: The threshold current density as a function of reverse biases for all investigated device length ratios designs.**

## 6.6 Mapping of the operational bias conditions

Figures 6.12 displays the operational maps of the bias conditions for all the device designs 1:19, 1:9, 3:17 and 1:4. It shows the ML, lasing and non-lasing region in terms of driving conditions such as gain-section current density and reverse-bias. In general, InAsP QDs are predicted to provide a broader ML range than those predicted for InP QDs in Chapter 5, Section 5.6. Devices with an absorber-to-gain length ratio of 1:19 and 1:9 are predicted to provide an ML regime under the same bias conditions at a gain-section current density between 286 A.cm$^{-2}$ and 857 A.cm$^{-2}$ over the entire studied

reverse bias absorber voltage range (1 V– 6 V). At a gain-section current density above 857 A.cm$^{-2}$, the device is predicted to only lase CW which is attributed to the insufficient absorption for pulse shortening due to the short SA-section length. The device design with a length ratio of 3:17 is predicted to obtain mode-locking behaviour within the gain-section current density range of (476 Acm$^{-2}$– 857 A.cm$^{-2}$) under reverse-bias SA voltage of 1 V and 2 V. Under the same reverse-bias condition and at a higher gain-section current density than 857 A.cm$^{-2}$, the device is expected to lase. The device is predicted to behave in mode-locking regime at a broader gain current density range of (476 A.cm$^{-2}$– 1667 A.cm$^{-2)}$, under the reverse bias range of 3 V– 6 V. For the device with a length ratio of 1:4, the ML regime is determined over a reverse-bias absorber voltage ranging between 1 V and 4 V and at high drive current density above 857 A.cm$^{-2}$. The increase of reverse-bias SA voltage reduces the accessible gain-section current density range that could produce ML regimes. The range of ML narrows with the increase of reverse-bias from 3 V to 4 V, and no ML regime is predicted for reverse bias above 4 V due to the absorption being greater than the gain. Thus, the shortening and broadening are out of balance.

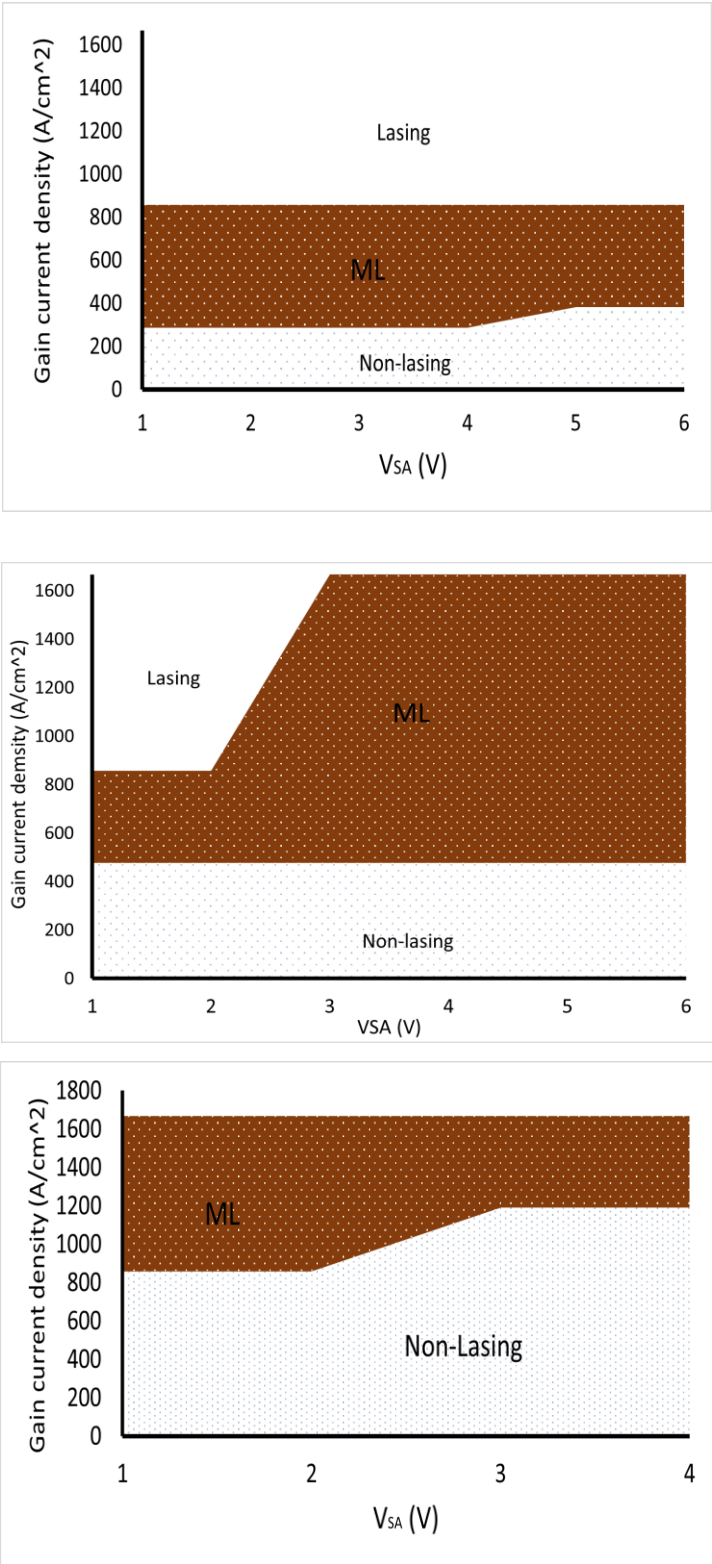


**Figure 6. 12: The ML operational maps of biases conditions for all the device length ratio designs: 1:9 and 1:19 (upper), 3:17 (middle) and 1:4 (bottom).**

## 6.7 Peak wavelength and spectral FWHM of Predicted ML pulses

This section explores the spectral performance of the predicted ML pulses for the range of bias conditions, such as peak wavelength and spectral FWHM, for all investigated device designs with absorber-to-gain length ratios of 1:4, 3:17, 1:9 and 1:19, which are plotted in Figure 6.13, 6.14, 6.15 and 6.16, respectively. The peak wavelengths of ML pulses at a fixed reverse bias shift slightly towards shorter wavelengths as the gain-section current density increases, and the spectral FWHM broadens as the broadening level rises. In contrast, with the increase of the reverse-bias voltage at a constant gain-section current density, the peak wavelengths shift at a higher rate and towards longer wavelengths. Additionally, the spectral FWHM narrows under the same bias conditions because of the QCSE (Mark Fox 2010). These findings are consistent across all investigated device designs. This behaviour agrees with the predictions of InP QDs performance (see Chapter 5, Section 5.7) and with the experimental work of different QD materials that have been carried out in literature(Thompson et al. 2009a).

The predicted peak wavelength of ML pulses for a device design ratio of 1:19 ranges from 760 nm to 768 nm, corresponding to the range of 10 nm to 40 nm of spectral FWHM (see Figure 6.13). The predicted range of peak wavelengths for a device design ratio of 1:9 is between 767 nm and 776 nm, with FWHM ranging from 8 nm and 29 nm (see Figure 6.14). The device design with a ratio of 3:17 has a wavelength range starting from 768 nm to 778 nm (see Figure 6.15). The wavelength range of a device design with a ratio 1:4 is between 770 nm and 780 nm with corresponding FWHM ranging from 10 nm to 26 nm (see Figure 6.16).

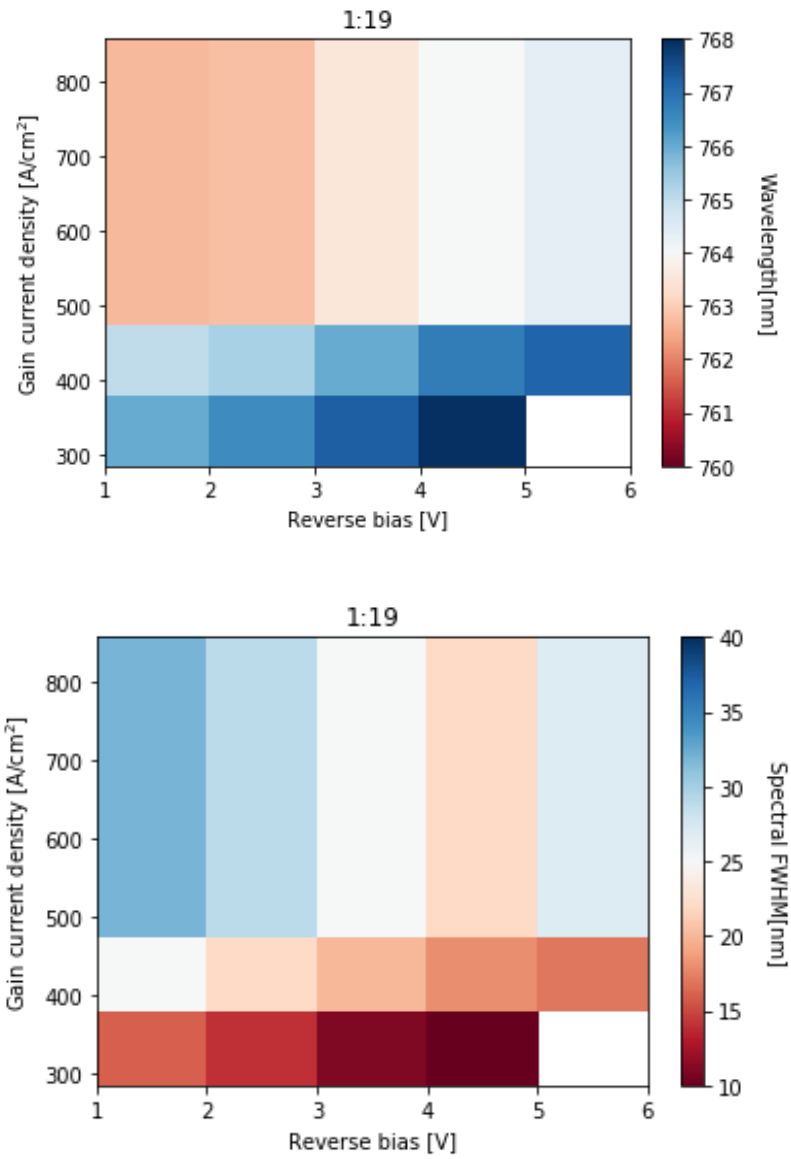


**Figure 6. 13: The peak wavelength and spectral FWHM of the predicted ML regimes for device length ratio design 1:19 as a function of operating biases conditions (The white area denotes no ML regime region).**

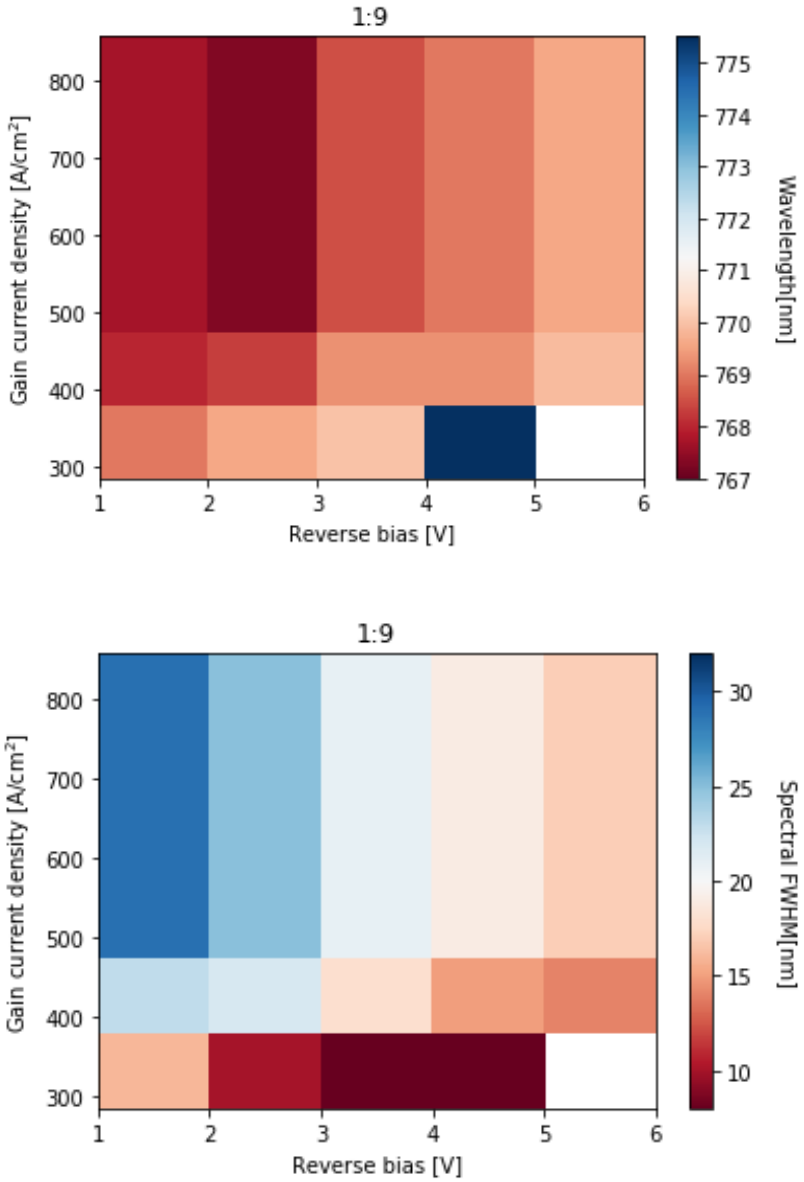


**Figure 6. 14: The peak wavelength and spectral FWHM of the predicted ML regimes for device length ratio design 1:9 as a function of operating biases conditions (The white area denotes no ML regime region).**

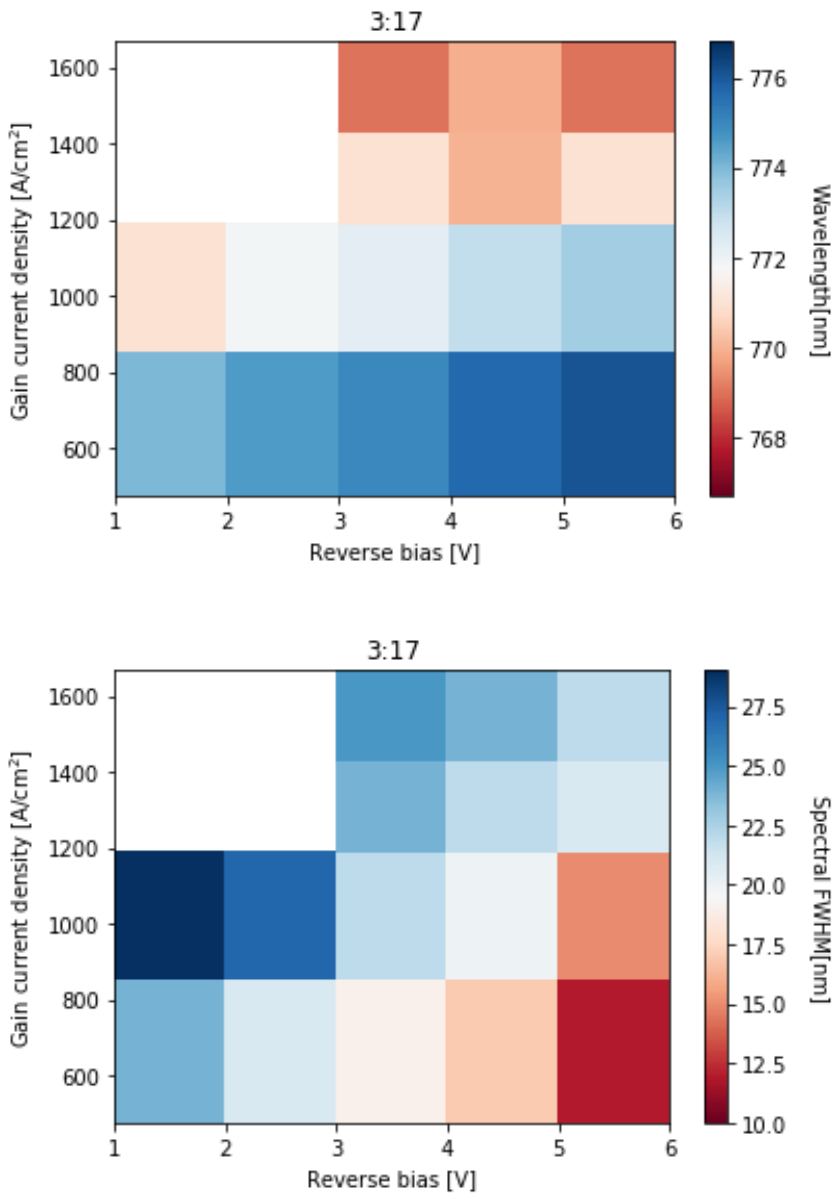


**Figure 6. 15: The peak wavelength and spectral FWHM of the predicted ML regimes for device length ratio design 3:17 as a function of operating biases conditions (The white area denotes no ML regime region).**

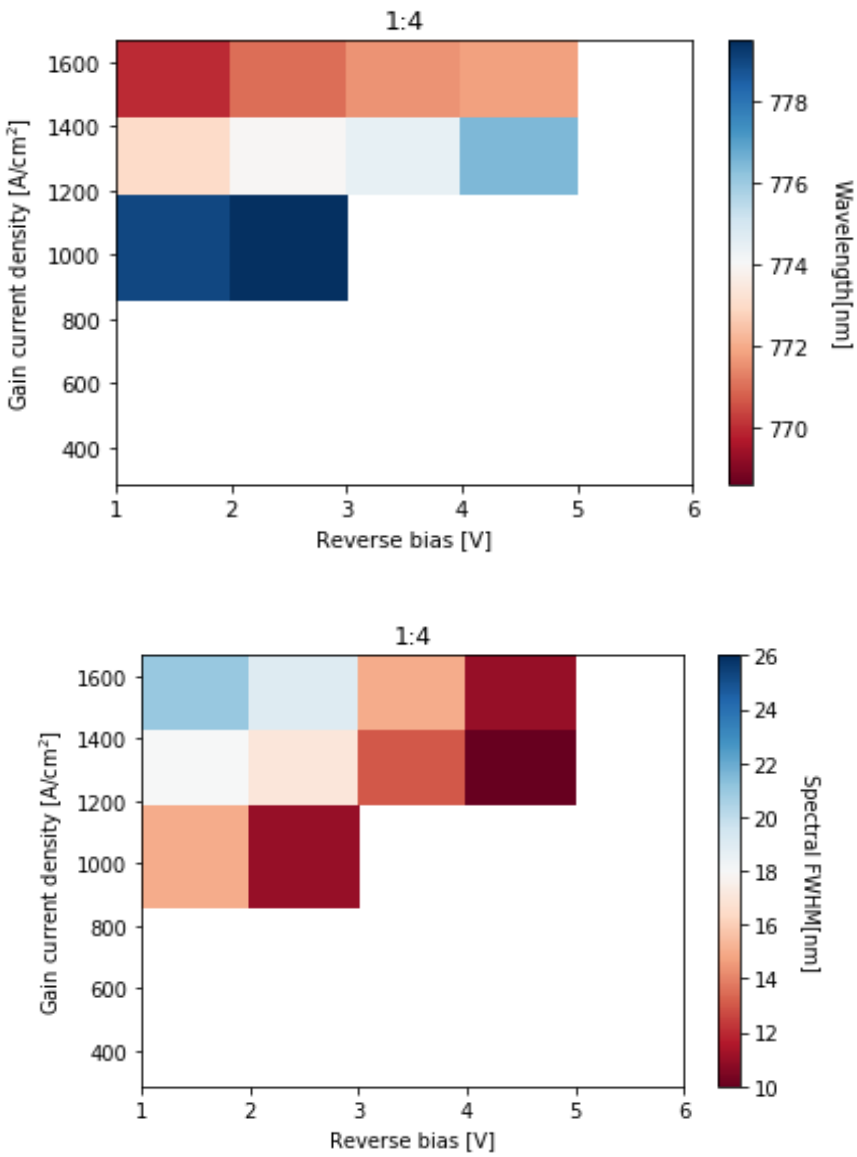


**Figure 6. 16: The peak wavelength and spectral FWHM of the predicted ML regimes for device length ratio design 1:4 as a function of operating biases conditions (The white area denotes no ML regime region).**

## 6.8 Mode-Locking Trends

This section presents some likely ML trends associated with changing parameters such as gain-section current density, reverse bias absorber voltage and absorber-to-gain length ratios. These trends have been investigated in Chapter 5, Section 5.8 for InP

QDs. Additionally, experimental studies in the literature have addressed these trends, but for different QD materials (Thompson et al. 2009a).

### 6.8.1 Current density of the gain-section

The influence of the gain current density on peak wavelength and the corresponding spectral FWHM at a fixed reverse bias of 6 V and fixed absorber-to-gain length ratio of 3:17 is plotted in Figure 6.17. When the gain-section current density increases, the spectral FWHM widens, and the peak wavelength shifts slightly towards shorter wavelengths. The filling of the lower energy states and the succeeding transition to the higher energy states are responsible for this blue shift. However, the shortening effect caused by the absorption slows this blue-shift rate. Gain amplitude and FWHM both grow in conjunction with higher gain-section current density. Consequently, more spectral broadening results in shorter pulses in the time domain. Based on these results, it might be concluded that increasing the gain-section current density would boost the device's performance in terms of output power.

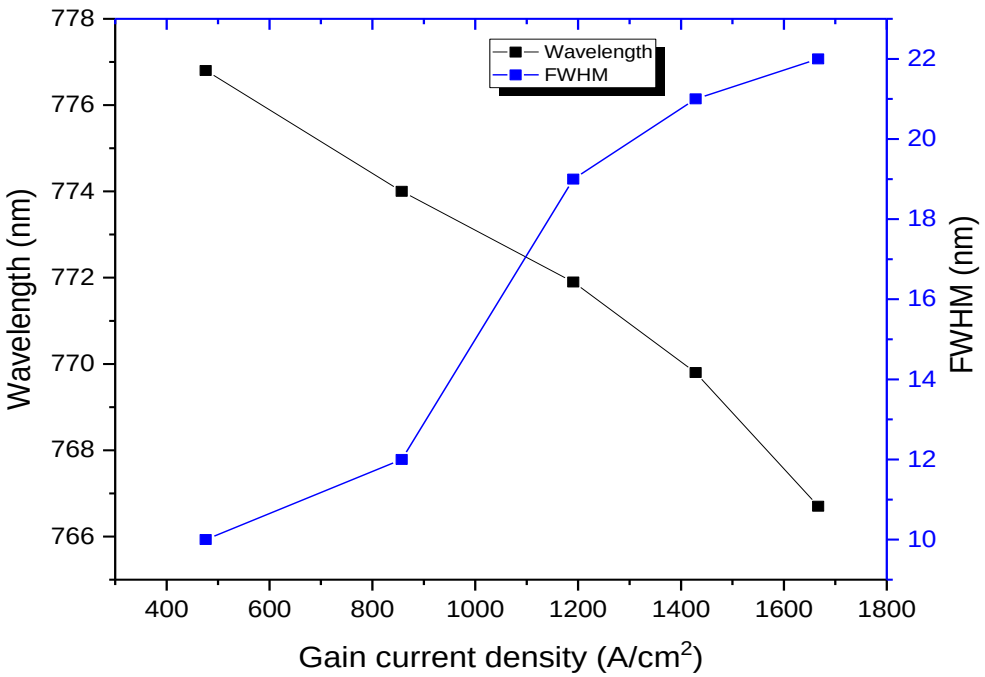


**Figure 6. 17**: **The peak wavelength and the spectral FWHM versus the gain-section current density for device length ratio 3:17 and at fixed reverse bias 6 V.**

### 6.8.2 Reverse-bias voltage of SA-section

The effect of the reverse-bias on operating wavelength and spectral FWHM of device design with ratio 1:4, and at a fixed gain-section current density 1190 A.cm$^{-2}$ is demonstrated in Figure 6.18. An increase in the reverse-bias voltage of the SA causes the band gap to drift due to QCSE (Mark Fox 2010), pushing the peak wavelength towards longer wavelengths (red-shift). The spectral FWHM corresponding to these wavelengths narrows with the application of reverse-bias voltage to the SA-section. Consequently, less spectral broadening results in broader (longer) pulses. Additionally, the reverse bias causes a reduction in gain amplitude and, consequently, the output power.

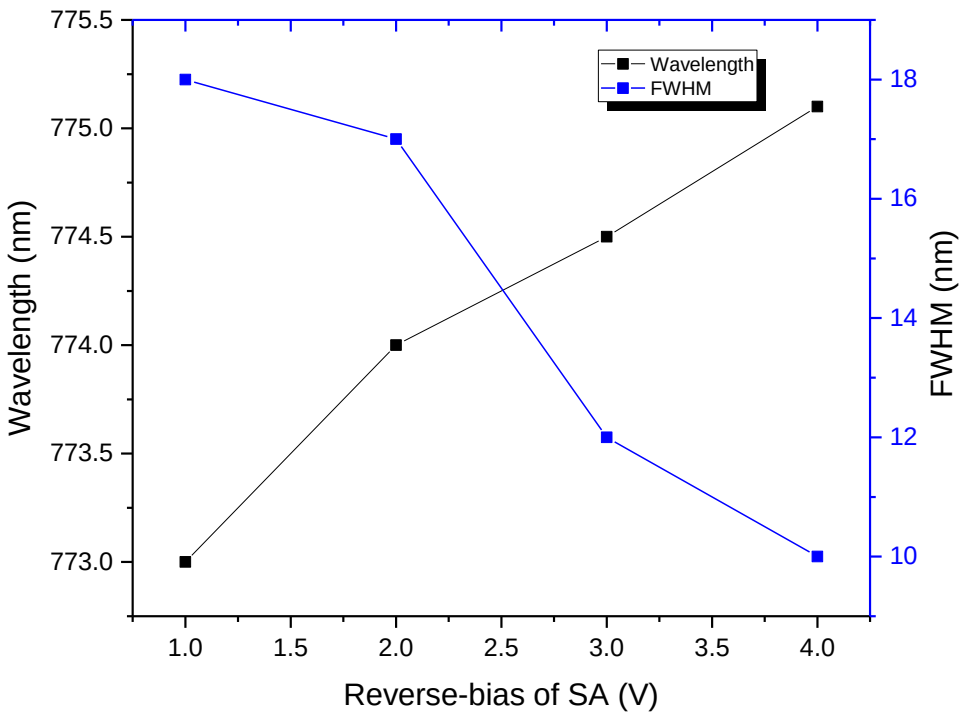


**Figure 6. 18: The peak wavelength and the spectral FWHM versus the reverse bias of SA-section for device length ratio 1:4 and at fixed gain-section current density 1190 A.cm$^{-2}$.**

### 6.8.3 Absorber-to-gain length ratios

The impact of absorber-to-gain length ratio plays an important role in shaping performance. Figure 6.19 shows this effect of absorber-to-gain length ratio on the operating wavelength and FWHM of spectral width at a fixed reverse bias of 2 V and a gain-section current density of 857 A.cm$^{-2}$. The increase of the SA-section length causes a narrowing in the FWHM, and the operating wavelength shifts towards longer wavelengths. Increasing the SA length will enhance the devices' performance in terms of chirping performance. As the pulse passes across the long SA section, it may be more attenuated by the growing absorption it encounters.

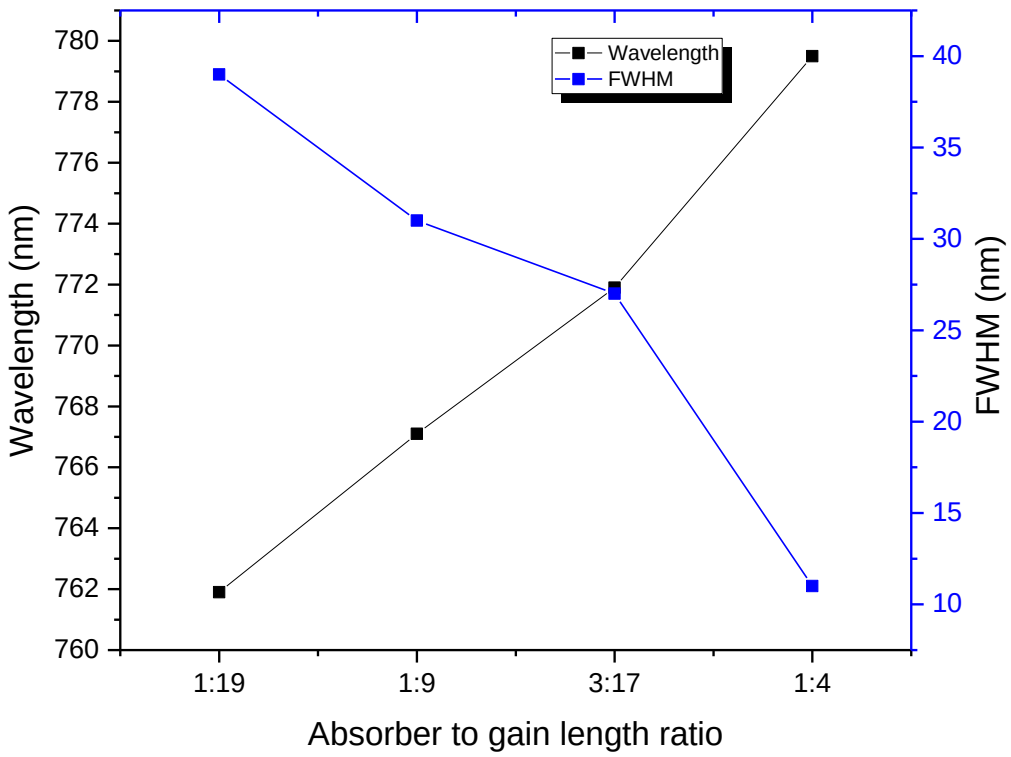


**Figure 6. 19: The peak wavelength and the FWHM versus the absorber-to-gain length ratios of SA-section at gain-section current density of 857 A.cm$^{-2}$ and at fixed gain reverse bias 2 V.**

## 6.9 Conclusion

A detailed review of the investigation of the performance of InAsP QDs MLLs has been provided in this chapter, using the novel semi-empirical approach. The review involved predicting net MLL modal gain and the threshold current density. These predictions were determined over three parameters: gain-section current density, the reverse bias voltage of SA and absorber-to-gain length ratios. Additionally, the predictions of the bias condition operational map, the operating wavelength and the FWHM of the spectral width for all device length ratio designs were also involved. Moreover, ML trends were provided for all the investigated parameters.

All studied device designs were predicted to obtain stable ML pulses in different bias conditions. Device designs with ratios 1:9 and 1:19 were predicted to achieve stable ML pulses at the same bias conditions at a gain-section current density between 286 $A.cm^{-2}$ and 857 $A.cm^{-2}$ over the entire studied reverse bias voltage range (1 V– 6 V). The devices are predicted to lase continuously at a gain-section current density above 857 $A.cm^{-2}$. The device design with a length ratio of 3:17 is predicted to obtain mode-locking behaviour within the gain-section current density range of (476 $A.cm^{-2}$– 857 $A.cm^{-2}$) under reverse-bias SA voltage of 1 V and 2 V. Under the same reverse-bias condition and at a higher gain-section current density than 857 $A.cm^{-2}$, the device is expected to lase continuously. The mode-locking region predictions of the device with a length ratio of 3:17 was a gain-section current density of between 476 $A.cm^{-2}$ and 857 $A.cm^{-2}$ when the reverse bias voltage was in the range of 1 V– 2 V and a gain-section current density of between 476 $A.cm^{-2}$ and 1667 $A.cm^{-2}$ when the reverse bias voltage was in the range of 3 V– 6 V. For the device with a length ratio of 1:4, the ML regime is determined over a reverse-bias absorber voltage range of between 1 V to 4 V and at high drive current density above 857 $A.cm^{-2}$. The range of ML narrows with the increase of reverse bias from 3 V to 4 V, and no ML regime is predicted for reverse bias above 4 V due to the absorption being greater than the gain; thus, the shortening and broadening are out of balance.

Wavelength blue-shifting occurs as the gain-section current density increases, while wavelength red-shifting occurs when the reverse-bias voltage increases. On average, ML pulses may be generated from InAsP QDs within the following wavelength range:

770 nm to 780 nm for a device design of length ratio 1:4, 768 nm to 778 nm for 3:17, from 767 nm and 776 nm for 1:9 and 760 nm to 768 nm for 1:19.

In comparison to the predicted InP QDs MLL performance, InAsP QD passive MLL showed much better-predicted performance, such as a broader stable ML region, a lower threshold current density, a shorter pulse width and a broader wavelength tuning range over all the investigated parameters (gain-section current density, reverse-bias of absorber and absorber-to-gain length ratios).

## References

Mark Fox 2010. *Optical Properties of Solids*. second edition. Fox. Mark ed. New York: Oxford University Press.

Peter Blood 2015. *quantum confined laser devices*. First edition. Blood, P. ed. New York: Oxford University press.

Rafailov, E.U. and Avrutin, E. 2013. Ultrafast pulse generation by semiconductor lasers. In: *Semiconductor Lasers: Fundamentals and Applications*. Elsevier Ltd, pp. 149–217. doi: 10.1533/9780857096401.1.149.

Thompson, M.G., Rae, A.R., Xia, M., Penty, R. v. and White, I.H. 2009. InGaAs quantum-dot mode-locked laser diodes. *IEEE Journal on Selected Topics in Quantum Electronics* 15(3), pp. 661–672. doi: 10.1109/JSTQE.2008.2012265.

# Chapter 7: InP QD passively monolithic MLLs: Experimental results

## 7.1 Introduction

In this chapter, we review the results of experimental MLLs that we have published in Li et al. 2020. Our semi-empirical approachs' validity has been tested by comparing it to the experimental data. We have shown the L-I characteristics, the spectral performances, the temporal performances, and the radio frequency (RF) results. Most importantly, we have discussed the similarities and the differences between the predicted and the experimental performance. We also highlight the limitation of shallow ridge device.

## 7.2 Experimental Results

It is important to note that the contact geometry of devices used in the semi-empirical approach differs from the contact geometry of devices used for practical InP QD MLLs. The oxide-stripe is used for the semi-empirical approach whereas the ridge used for practical InP QD MLLs. The two devices are illustrated in Chapter 3, Sections 3.2 and 3.3. Therefore, a current calibration is needed for an accurate comparison, since the current flow is restricted by the device's width.

### 7.2.1 Light-Current (L-I) Performance

The L-I characteristic of the device design of absorber-to-gain length ratio (1:4) has been measured by constant current (CW) forward bias of the gain-section. Simultaneously, the SA section was either driven by a forward current injection, a floating (unbiased condition) or a reverse bias (1V to 3V). The measurement was taken at a device heatsink temperature of 10℃ (283.15 K). The power of the single-facet

laser emission was measured using an integrating sphere. Figure 7.1 illustrates the L-I characteristics of 3 mm InP MLLs. When the SA section is under forward bias, the measured power performance was consistent with a typical laser with a threshold current of 14 mA and power as high as 10 mW at a driven current of 90 mA. The power dropped/reduced to 7 mW, and the threshold current increased to 30 mA when the SA section was unbiased (floating). When the reverse bias was applied to the SA section, the power was further reduced to lower values, and the threshold current increased. As the reverse bias increased, the power reduced and the threshold current increased due to the increase of the absorption and the presence of the shortening effect. The high reduction in power when SA is reverse-biased could be attributed to the effect of strong spatial hole burning as a result of concentrating the SA in a single area of a laser (Rafailov and Avrutin 2013).

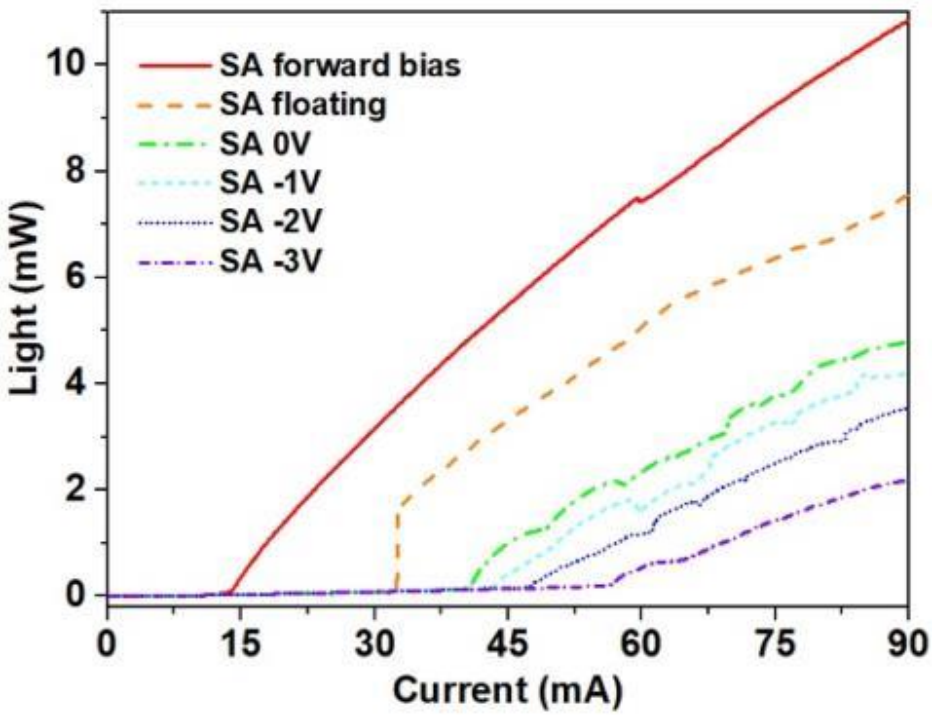


**Figure 7. 1: The L-I characteristics of device design of absorber-to-gain length ratio (1:4) for different bias conditions: forward, floating, and reverse-bias (1 V-3 V).**

The trends in L-I characteristics are consistent with the predicted performance presented in Chapter 5, Section 5.4 in two behaviours. Firstly, the reduction in power and the increase of threshold current with the increase of reverse bias of SA. Secondly,

no lasing occurred above 3 V, which nearly matches the predictions of no lasing above 4 V presented in Chapter 5, Section 5.5. However, there are slight variations in values when we compare the predicted threshold current density and the measured threshold current density. It is unclear if these changes result from the differences between the two contact configurations: oxide stripe and shallow ridge (gain-guided and index-guided). Additionally, the differences in the exact values may be explained by the uncertainty of current calibration. We don't know the exact effective mode area width of the shallow ridge MLLs due to the unavailability of near-field measurements for the shallow ridge MLL. We have used the actual ridge-width of the device (before pumping), which is 2 μm, but due to the current spreading, the effective width is assumed to be slightly wider than the real one. Therefore, comparing the exact numbers of threshold currents between the predicted and the measured results will be unrealistic.

It has been observed that differences in the threshold current density values between the deep ridge and the shallow ridge lasers are due to the effect of anti-guiding of the lateral confinement (Redaelli et al. 2013). The carrier-induced index shift may compensate for the built-in refractive index step of ridge lasers, leading to high losses and an increase in the threshold current if the ridge is not deep enough, as in shallow ridges (Redaelli et al. 2013). This might be one reason for the differences in the threshold current density due to the differences in the contact geometry of the device used for characterisation and the practical MLLs.

### 7.2.2 Spectral and Temporal Performance

Figure 7.2 shows autocorrelation traces and optical spectra measured under 75 mA, 80 mA, and 85 mA gain currents and under fixed reverse-bias – 1.85 V. The pulse width decreased from 20 ps to 8 ps when the gain current was increased, whereas the wavelength blue-shifted from 735.6 nm to 733.2 nm. We relate this blue shift in lasing wavelength to the increment of the larger injection currents causing an increase in the broadening level due to the state-filing. Thus, the optical gain peak moves to shorter wavelengths. This result reveals that the gain is not completely clamped throughout the QD ensemble at these lasing conditions as in a Fabry-Perot laser.

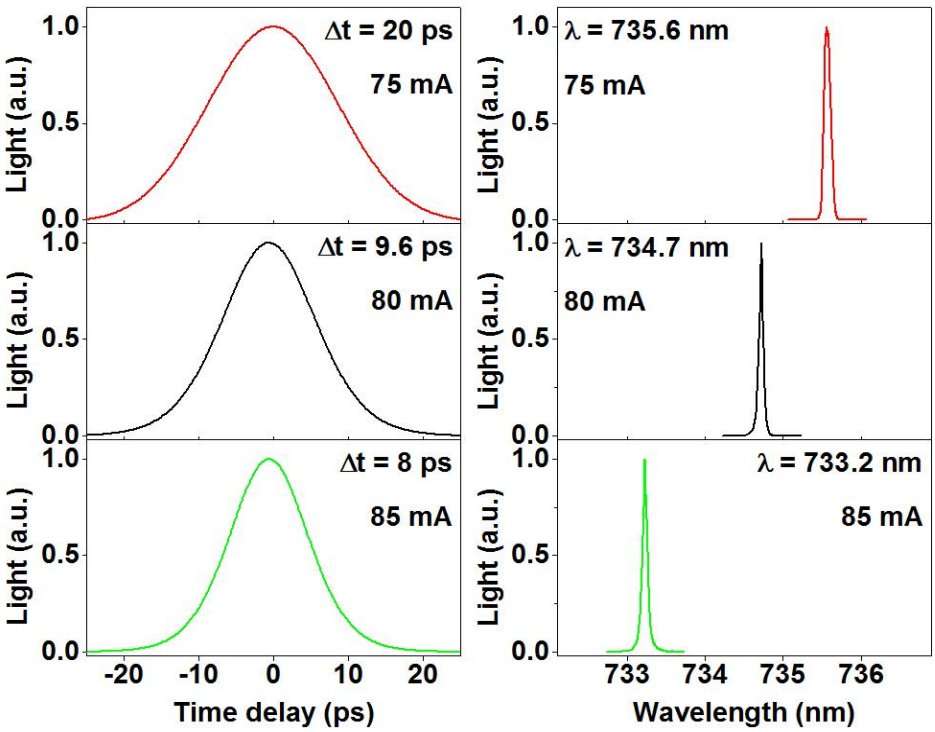


**Figure 7. 2: Pulse width and optical spectrum at a fixed reverse bias (1.85 V) measured at a gain current of 75 mA, 80 mA, and 85 mA.**

To compare these experimental results with the predicted performance using the semi-empirical approach in Chapter 5, the gain current was calibrated to encounter the cross-section area of the segment of non-lasing structure that is used to measure the modal gain and absorption for predictions made by our semi-empirical approach. Figure 7.3 illustrates the experimental results of predicted net MLL gain under the same conditions. The trend of the wavelength's blue shift is consistent with the predicted performance. These results confirm the criterion we used where the ML occurs at the gain saturation near or above the threshold, thus, validating the semi-empirical approach we have established in Chapter 5. Additionally, bias conditions of these ML pulses are within the predicted ML range of device design with absorber-to-gain length ratio (1:4). However, the peak wavelengths are shorter than the predicted wavelengths (see Table 7.1). The differences in the predicted and experimental wavelength might be related to minor variations, such as variations in shallow ridge depth, SA length, gain length, width, temperature, etc. However, the blue-shift behaviour agrees with the predicted behaviour trend findings shown in Chapter 5.

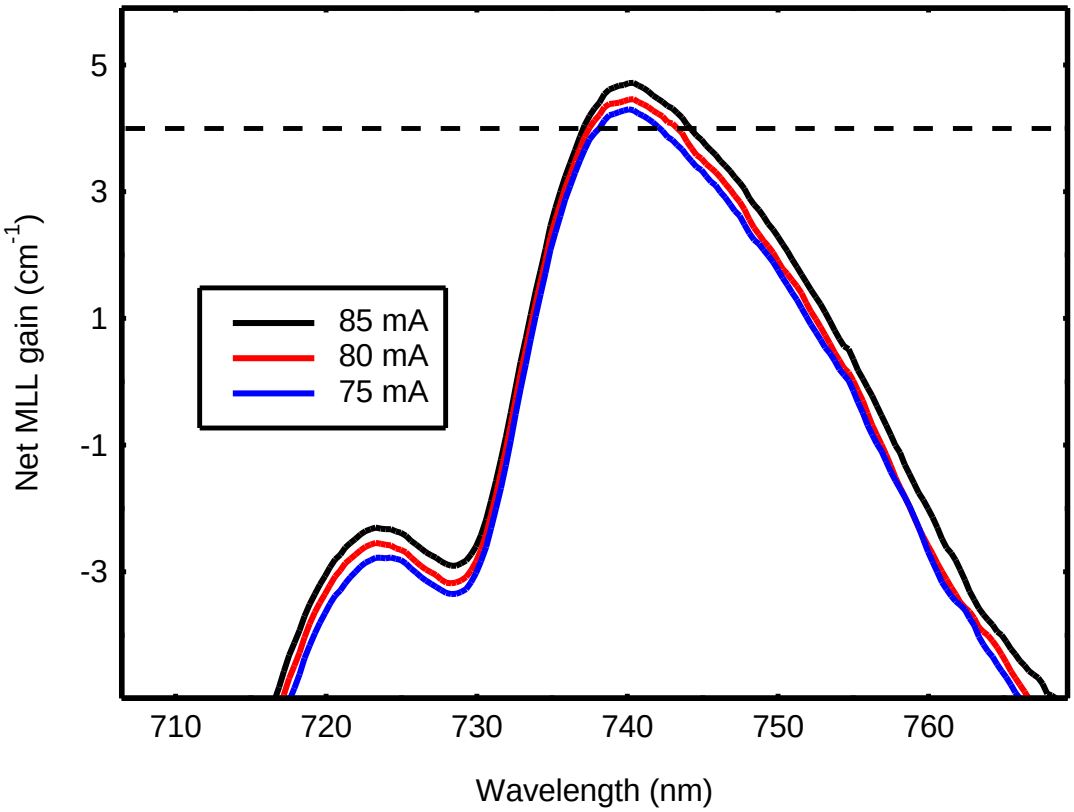


**Figure 7. 3: The predicted net MLL gain of the device with length ratio (1:4) at gain current 75mA, 80mA, and 85mA and fixed reverse-bias 1.85V.**

**Table 7. 4: Comparison of the experimental and predicted performance.**

| $J_{gain}$ (A.cm$^2$) | ($I_{gain}$) mA | $V_{SA}$ (V) | $\lambda_{Pred.}$ (nm) | $\lambda_{Exp.}$ (nm) |
|---|---|---|---|---|
| **1352** | 75 | 1.85 | 740.3 | 735.6 |
| **1563** | 80 | 1.85 | 739.8 | 734.7 |
| **1665** | 85 | 1.85 | 739.4 | 733.2 |

### 7.2.3 Radio Frequency (RF) Measurements

As mentioned in Chapter 2, Section 2.4.2, there is an inverse relation between the repetition frequency and the cavity length. Figure 7.6 demonstrates the RF electrical spectra for MLL of different total cavity length of 2 mm, 2.5 mm, 3 mm and 3.5 mm, and under different operating bias conditions. The MLL with total cavity length of 2 mm, under gain-section current of 110 mA and SA-reverse bias of 2 V, generated pulses with repetition rate of 18.89 GHz. Device with total cavity length of 2.5 mm, under gain-section current of 97 mA and SA-reverse bias of 2.2 V, generated pulses with repetition rate of 14.98 GHz. MLL with total cavity length of 3 mm, under gain-section current of 110 mA and SA-reverse bias of 2 V, generated pulses with repetition rate of 12.55 GHz. MLL with total cavity length of 3.5 mm, under gain-section current of 69 mA and SA-reverse bias of 1.6 V, generated pulses with repetition rate of 10.74 GHz. MLLs with the short cavity length demonstrate better performance in term of repetition frequency.

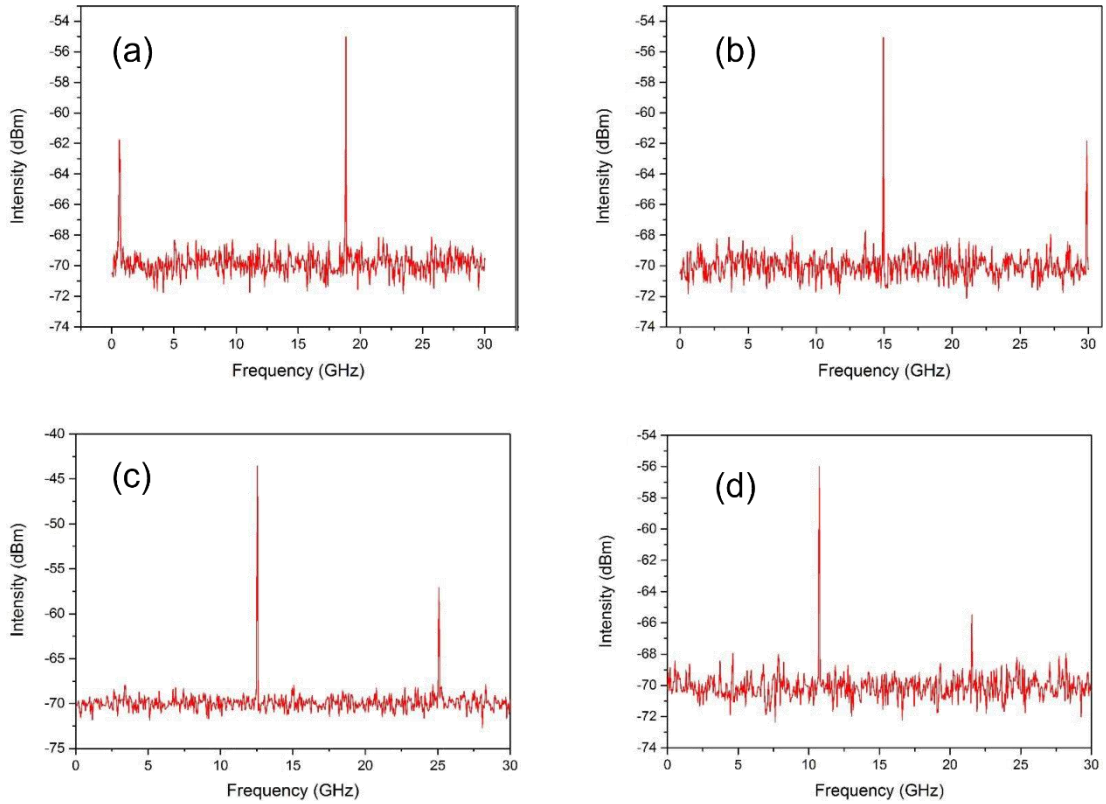


**Figure 7. 5: RF spectra as a function of intensity in dBm demonstrate the repetition frequency of four MLLs with different total cavity length (a) 2 mm, (b) 2.5 mm, (c) 3mm and (d) 3.5 mm.**

## 7.3 Validation of the Semi-Empirical Approach

The differences between the predicted and the experimental performances might be explained by the differences in the devices' contact geometries, gain-guided used in the non-lasing devices for predicting the performance and index-guided used in the fabricated MLLs. In gain-guided lasers, the spontaneous emission coupling factor (β) is greater than in lasers with an equivalent active layer volume and an index-guided waveguide. This results in a significantly broader spectral width. Therefore, if the full bandwidth is effectively engaged, broad spectra of gain-guided lasers might provide short pulses compared to index-guided lasers (Nikitichev et al. 2011).

It has been experimentally demonstrated using the InAs/InGaAs QD materials (Nikitichev et al. 2011) that the two devices' contact geometry, Oxide-confined and

Shallow ridge, perform differentially, particularly their spectral and temporal performance. For example, the spectral width of oxide-confined lasers is considerably broader compared to the shallow ridge lasers.

Furthermore, several research groups have noticed that the range of driving conditions for stable mode-locked pulses is greater than that of comparable lasers (Nikitichev et al. 2011) ;(Thompson et al. 2006). The effective cross-section area of the gain section must be much bigger than the area of the absorber section to maximise the stable ML range. This is done by tapering the gain section, due to which the SA section becomes much narrower than the gain section. This strategy enhances the performance of InGaAs and InAs QDs MLL by providing a wider stable ML range and the shortest pulse obtained from this material (Nikitichev et al. 2011) ;(Thompson et al. 2006). With tapered structures, the saturation inside the absorber section is increased compared to non-tapered structures because the effective modal area of the gain section is larger than that of the absorber section. It has been noted that an un-tapered waveguide, including the shallow ridge and oxide stripe, produces much worse ML performance than tapered waveguide. Tapered waveguides generate ML pulses with short pulse width and high output power due to the larger area of the gain section and narrow SA section (Nikitichev et al. 2011; Rafailov & Avrutin 2013).

The agreements between the predicted performance and the experimental results could be summarised with the following points:

- The experimental performance of L-I characteristics of InP QDs agrees with the predictions regarding power reduction and the increase of threshold current density with the reverse bias of SA.
- The ML pulses of the device with absorber-to-gain length ratio of (1:4) have been obtained experimentally under biased conditions within the range of the predicted operational map.
- The blue-shift trend was validated against experimental results; the wavelength blue-shifted with the increase of gain-current at a fixed reverse bias of SA.

## 7.4 Conclusion

L-I characteristics, spectral performance, temporal performance, and RF electrical spectra of InP QDs MLLs published in (Li et al. 2020) were provided here to validate the results obtained from our semi-empirical approach in Chapter 5. Experimental results reveal that our semi-empirical approach offers fair predictions of performance. The agreement of the trends between the predicted and experimental performances indicates that our semi-empirical approach is a good approximation. However, the experimental results obtained, particularly the exact numbers of threshold current density and wavelength, are slightly shifted from the predicted performance. We have attributed this to the differences in the cavity area of the ridge and the oxide laser.

## References

Li, Z. et al. 2020. Monolithic InP Quantum Dot Mode-Locked Lasers Emitting at 730 nm. *IEEE Photonics Technology Letters* 32(17), pp. 1073–1076. doi: 10.1109/LPT.2020.3012568.

Nikitichev, D.I. et al. 2011. High-power passively mode-locked tapered InAs/GaAs quantum-dot lasers. *Applied Physics B: Lasers and Optics* 103(3), pp. 609–613. doi: 10.1007/s00340-010-4290-5.

Rafailov, E.U. and Avrutin, E. 2013. Ultrafast pulse generation by semiconductor lasers. In: *Semiconductor Lasers: Fundamentals and Applications*. Elsevier Ltd, pp. 149–217. doi: 10.1533/9780857096401.1.149.

Redaelli, L., Wenzel, H., Martens, M., Einfeldt, S., Kneissl, M. and Tränkle, G. 2013. Index antiguiding in narrow ridge-waveguide (In,Al)GaN-based laser diodes. *Journal of Applied Physics* 114(11). doi: 10.1063/1.4821064.

Thompson, M.G. et al. 2006. Subpicosecond high-power mode locking using flared waveguide monolithic quantum-dot lasers. *Applied Physics Letters* 88(13). doi: 10.1063/1.2186110.

# Chapter 8:

# Conclusion and Future Work

## 8.1 Summary

InP and InAsP self-assembled QDs passively monolithic MLLs are a promising alternative MLL source to Ti:Sapphire solid-state lasers in the range (690–780nm) for applications with size, weight and power restrictions. The overall conclusions of this thesis are summarised in this section.

This thesis described the efforts that have been carried out to investigate the feasibility of using InP and InAsP QD materials for passive mode-locking. This was achieved through a complete investigation of the modal gain and modal absorption under forward and reverse bias conditions by using the segmented contact method (SCM). The gain and absorption experimental data enabled the establishment of a novel semi-empirical approach based on the combination of modal gain and modal absorption with particular attention paid to the absorber-to-gain length ratio. This led to the predictions of the performance of InP and InAsP QD passively monolithic MLLs. Thus, reducing the time to realise the best performing InP and InAsP QD passively monolithic MLLs.

Chapter 4 described the experimental work carried out to establish a complete understanding of the characteristics of the forward-biased gain-section and the characteristics of the reverse-biased SA-section of InP and InAsP QDs at room temperature. The gain bandwidth of both QD materials was relatively broad due to the inhomogeneous broadening due to the distributions of dots' sizes, with FWHM approximately 24 nm for InP QDs and 36 nm for InAsP QDs with peak wavelengths of 728 nm and 773 nm, respectively. The peak wavelength blue-shifts for InP QDs starting from 729 nm at a gain-section current density of 300 $A.cm^{-2}$ to 709 nm at a gain-section current density of 1803 $A.cm^{-2}$. The blue-shift for InAsP QDs started from a wavelength of 773 nm at a gain-section current density of 95 $A.cm^{-2}$ to 745 nm

at a gain-section current density of 1666.7 A.cm$^{-2}$. The gain peaks saturated, due to the Pauli blocking effect at the highest injected current density, for InP QDs and InAsP QDs at 17cm$^{-1}$ and 13cm$^{-1}$, respectively. The gain peak of InAsP QDs saturated at a lower gain peak compared to InP QDs due to the high degree of dot size distribution of this structure.

The characteristics of the reverse-biased SA-sections demonstrated red-shift with the application of reverse bias between (0 – 6 V) with an absorption tuning wavelength range of (728 nm– 735 nm) and (773 nm– 781.8 nm) for InP and InAsP QDs, respectively. The red shift of the wavelength was attributed to the QCSE theory. The rate of change of InP QDs was 1.17 nm/V with a total shift of 7 nm, whereas the rate of InAsP QDs was 2 nm/V with a total shift of 9 nm. However, the red shift of InAsP absorption was suppressed at a high reverse bias (4 V– 6 V) and the shift rate changed to approximately 1 nm/V. This red-shift suppression was attributed to the escape of the newly added carriers to the wetting layer due to the small height of InAsP dots.

The investigations of the gain-current relation for both materials showed that they both fulfilled the ML condition, which was represented by the s-factor. Both met the requirements for generating stable ML pulses; both materials exhibited faster gain energy saturation than absorption saturation. Additionally, both materials exhibited low threshold current density, thus, low levels of ASE, which resulted in low jitter. Interestingly, InAsP QDs had faster and stronger gain saturation, broader gain FWHM and lower threshold current density compared to InP QDs which are all desirable properties for the excellent performance of passive MLLs. However, the gain peak amplitude of InAsP QDs is lower than those of InP QDs, which might be the reason of low-power MLLs. In short, InAsP QDs are more broadband and InP QDs have higher gain, leading to predictions of the possibility of achieving Mode-locking pulses from InP QDs at lower pumping rates but broader temporal pulse widths compared to InAsP QDs.

Chapters 5 and 6 provided a comprehensive review of the predicted performances of InP and InAsP QDs passively monolithic MLLs using the novel semi-empirical approach established in this work. The review involved the predicted net modal gain of MLLs for different gain-section current density, reverse bias voltage and various absorber-to-gain length ratios. The investigated absorber-to-gain length ratios were

1:19, 1:9, 3.17 and 1:4. Additionally, the estimation of threshold current density for the studied device designs and the entire set of reverse bias voltages were provided. Moreover, the perational map of the bias conditions , the operating wavelength and the FWHM of the spectral width were predicted for all device absorber-to-gain length ratio designs. ML trends at gain-section current density, reverse bias voltage and absorber-to-gain length ratios were studied intensively.

InP QDs passively monolithic MLLs were predicted to perform the best with device designs of absorber-to-gain length ratio of 1:4, 3.17 and 1:9 in different forward and reverse bias conditions. Stable ML pulses could be achieved at high injected current density above 1200 $A.cm^{-2}$ of 1:4 at a range of reverse bias voltages from 1 V– 4 V. ML regimes were not predicted to occur at very high reverse bias, between 5 V and 6V. Device designs with ratio 3.17 were predicted to achieve stable ML pulses at high injected current density above 902 $A.cm^{-2}$ for reverse bias voltage between 1 V to 5 V. No ML behaviour was predicted at a high reverse bias of 6 V.

The device design with ratio 1:9 was expected to produce ML pulses with lower gain current density between 600 $A.cm^{-2}$ and 1050 $A.cm^{-2}$ at the full range of the investigated reverse bias voltages (1 V– 6 V). The device was predicted to only lase at higher current density than 1050 $A.cm^{-2}$. However, the most interesting finding is that the device with design absorber-to-gain length ratio 1:9 could generate two ML pulses in the GS and ES. Furthermore, it was predicted that the device with the longest SA section 1:3 would not provide ML or lasing, while the device with the shortest SA section 1:9 would not provide ML performance but would have lasing benefits.

It has been found that there is a significant association between the length of the absorber section and the extent of the impact of the reverse bias voltage of SA on threshold current density. This extent increases with the increase of the absorber section length. The threshold current density increases as the SA length increases because the longer absorber section would require more current density to allow the gain to build up. The influence of reverse bias absorber voltage on threshold current density is restricted by the length of the SA section. The impact of the reverse bias is not significant in the shortest absorber lengths; however, it becomes significant as the absorber length is increased. It is difficult to obtain mode-locking behaviour with

absorber section lengths greater than 600 µm for a 3 mm total cavity length laser of InP QDs passively monolithic MLLs.

Blue-shifts of the wavelength arose when the gain-section current density was increased, whereas red-shifts occurred when reverse bias voltages were decreased. The ranges of the operating wavelength of ML pulses were as follows: 738.7 nm to 742.5 nm for device design 1:4, 737.6 nm to 742.6 nm for 3:17 and two ranges for 1:9; GS range from 736.9 nm to 741.9 nm and ES range from 724.3 nm to 728.3 nm. The studied device designs are expected to provide the shortest pulse width at different reverse bias voltages. The shortest pulse widths predicted for device designs (1:4), 3:17 and 1:9 were at reverse bias conditions 1 V, 1 V and 6 V with FWHM 10.8 nm, 9.5 nm and 11.1 nm, respectively.

InAsP QDs passively monolithic MLLs performance was predicted to produce the best result with device designs of absorber-to-gain length ratio of 1:4, 3.17, 1:9 and 1:19 in different forward and reverse bias conditions. Stable ML pulses could be achieved at high injected gain current density above 857 A.cm$^{-2}$ of 1:4 at reverse bias voltages of 1 V and 2 V and above 1190 A.cm$^{-2}$ at reverse bias voltages of 3 V and 4 V. No mode-locking behaviour was predicted for high reverse bias 5 V and 6 V. Stable ML pulses of device design 3.17 were predicted to be achieved at a gain current density between 476 A.cm$^{-2}$ and 857 A.cm$^{-2}$ when the SA was reversed-bias with 1 V and 2 V. At a gain current density higher than 857 A.cm$^{-2}$ and under the same reverse-bias conditions, the MLL will only lase. At higher reverse bias between 3 V and 6 V, ML regime was predicted to occur at a gain current density ranging from 476 A.cm$^{-2}$ to 1667 A.cm$^{-2}$. Device designs of 1:9 and 1:19 were predicted to generate ML pulses under the same forward and reverse bias conditions at a gain current density ranging from 286 A.cm$^{-2}$ to 857 A.cm$^{-2}$ for the entire reverse-bias voltage range (1 V– 6 V). A lasing regime is predicted to occur at a higher gain current density above 857 A.cm$^{-2}$.

Unlike findings from InP QDs, the extent of the impact of the reverse bias voltage of SA on the threshold current density of InAsP QDs was obvious even in the devices with shorter SA lengths. This extent increased gradually with the increase of the absorber section length, particularly for devices of 3:17 and 1:4. Similar to findings from InP QDs, the threshold current density increased as the SA length increased because the longer absorber section would need a higher current density for gain to

accumulate. Additionally, the influence of reverse bias absorber voltage on threshold current density is restricted by the length of the SA section. The impact of the reverse bias is not less significant in the shortest absorber lengths; however, it becomes more significant as the absorber length is increased. It is difficult to obtain mode-locking with absorber section lengths longer than 600 µm for a 3 mm total cavity length laser of InAsP QDs passively monolithic MLLs.

Similar to InP QDs, it has been found that the blue shift of wavelength arose with the increase of the gain-section current density, whereas a red shift occurred with the increase of reverse bias voltages. ML pulses are predicted to occur with operating wavelength ranges as follows: 770 nm to 778 nm for device design 1:4, 768 nm to 776 nm for 3:17, 767 nm to 775 nm for 1:9, and 760 nm to 768 nm for 1:19. The studied device designs are expected to provide the shortest pulse width at different reverse bias voltages. The shortest pulse widths predicted for device designs 1:4, 3:17, 1:9 and 1:19 were at reverse bias conditions 1 V with FWHM of 25 nm, 29 nm, 32 nm and 40 nm, respectively. These findings support the conclusion in Chapter 4 that InAsP QDs could provide shorter pulse width compared to InP QDs.

Chapter 7 demonstrated the examination of the reliability of the semi-empirical approach that has been established in this thesis. This approach provides reasonable agreement with the experimental data. Additionally, the mode-locking trends of both predicted performance and experimental results are in good agreement with the trends determined by other groups on different QD MLL. However, the slight difference in the exact numbers of the threshold current of the experimental and predicted performance might be attributed to the uncertainty of the mirror loss, or differences in device geometry, since we are comparing two different contact geometry oxides and ridges. In reality, minor variations in shallow ridge depth, SA length, gain length, width, etc., would result in differences in wavelength and threshold currents. Additionally, incorrect current calibrations are due to the fact that the real effective width may be larger or smaller than the actual width of the shallow ridge laser. However, the optimum ML pulse generated from InP QD MLLs for a drive current of 75 mA, 80 mA, 85 mA and a fixed reverse-bias of 1.85 V, and results in 20 ps, 9.6 ps and 8 ps pulses width. InP QD MLLs generate ML pulse with RF of 12 GHz measured at a gain current of 80 mA and reverse bias of 2.74 V.

Table 8.1 shows the performance of all current Quantum Dot passive mode-locked lasers in the literature including the operating conditions, the length of the gain and SA sections, the emitted wavelength under these conditions, the peak power, the pulse width and the reptetion frequency.

**Table 8. 1: The performance of all current QDs passively MLLs .**

| QD material | substrate | Device geometry | $L_g$ (mm) | $L_{SA}$ (mm) | I (mA) | $V_{abs}$ (V) | λ (nm) | P (mW) | T (ps) | F (GHz) | Reference |
|---|---|---|---|---|---|---|---|---|---|---|---|
| InAs/InGaAs | GaAs | Oxide-confined | 4.73 | 0.85 | 34.7 | -4 | 1287 | | 17 | 7.4 | (Huang et al. 2001) |
| InAs/InGaAs | GaAs | Shallow ridge | 7.8 | 1 | 60 | -7.3 | 1264 | 290 | 5.7 | 5.17 | (Zhang et al. 2005) |
| InGaAs | GaAs | Ridge tapered | 1.46 | 0.94 | 250 | -7.5 | 1280 | 500 | 0.78 | 24 | (Thompson et al. 2006) |
| 5-layers InAs/GaAs | GaAs | Gain-guided tapered | 2.37 | 0.4 | 950 | -5.1 | 1252.1 | 890 | 3.2 | 14.65 | (Nikitichev et al. 2011) |
| 10-layers InAs/GaAs | GaAs | Gain-guided tapered | 2.38 | 0.4 | 1044 | -4.9 | 1260.4 | 820 | 3.3 | 14.57 | (Nikitichev et al. 2011) |
| 5-layers InGaAs/AlGaAs | GaAs | | | | | | 1300 | | | | (Rafailov et al. 2007) |
| InAs/InGaAs | Si | Ridge MLL | 3.5 | 1 | 146 | -2.6 | o-band | | 1.3 | 9 | (Liu et al. 2018) |
| InAs/GaInAsP | InP | Ridge MLL | 0.71 | 0.09 | 70 | -1.2 | 1550 | | 2.5 | 48 | (Rosales et al. 2011) |
| InP/GaInP | GaAs | Shallow Ridge MLL | 2.4 | 0.6 | 80 | 2.74 | 734 | | 6 | 12.5 | (Li et al. 2020) |

## 8.2 Future work

The results of this work have been substantial in evaluating the feasibility of the employment of InP and InAsP QDs in passive mode-locking. The established semi-empirical approach, in this work, provided a direct method to study the passive MLLs' performance and to predict the best-performing device design in terms of absorber-to-gain length ratio for the purpose of providing the shortest mode-locking pulses. Additionally, the approach can capture some of the key trends associated with the bias conditions, particularly LI trends, blue shift and red shift. Experimental results reveal that our semi-empirical approach offers fair predictions of performance. However, there are areas of this work that might be addressed in the future to enhance the device's performance and functionality.

It was difficult to achieve ML pulses from shallow ridge MLLs, particularly from InAsP shallow ridge MLLs due to losses caused by side wall recombination and the low gain of the material. Therefore, the tapered gain section should be considered in future fabrication to enhance the performance, particularly the output power. The idea of using a tapered gain section is to ensure the light is more firmly confined on the SA section than on the gain section, so that the modal area of SA is smaller than the modal area of the gain section. Hence, one could improve the output power while maintaining a shorter ML pulse.

The gain amplitude is a significant area for future improvement. It could be increased by refining the design of the layers in the structure. The achievable gain could be improved by either increasing the number of dots layers or by the increase of the barrier thickness. However, the trade-off between the barrier thickness and the number of QD layers must be considered to fit the width of the optical mode. This also could expand the wavelength tuning range that was limited by the dots’ size and height. Therefore, the improvement of the QD growth is critical to optimise them for mode-locking devices for expanding the wavelength tuneability ranges at different driving bias conditions, and to increase the achievable gain.

## References

Huang, X., Stintz, A., Li, H., Lester, L.F., Cheng, J. and Malloy, K.J. 2001. Passive mode-locking in 1.3 μm two-section InAs quantum dot lasers. *Applied Physics Letters* 78(19), pp. 2825–2827. Doi: 10.1063/1.1371244.

Zhang, L. et al. 2005. Low timing jitter, 5 GHz optical pulses from monolithic two-section passively mode-locked 1250/1310 nm quantum dot lasers for high speed optical interconnects. In: *Conference on Optical Fiber Communication, Technical Digest Series*. pp. 281–283. doi: 10.1109/ofc.2005.192775.

Thompson, M.G. et al. 2006. Subpicosecond high-power mode locking using flared waveguide monolithic quantum-dot lasers. *Applied Physics Letters* 88(13). doi: 10.1063/1.2186110

Nikitichev, D.I. et al. 2011. High-power passively mode-locked tapered InAs/GaAs quantum-dot lasers. *Applied Physics B: Lasers and Optics* 103(3), pp. 609–613. doi: 10.1007/s00340-010-4290-5.

Rafailov, E.U., Cataluna, M.A. and Sibbett, W. 2007. Mode-locked quantum-dot lasers. *Nature Photonics* 1(7), pp. 395–401. doi: 10.1038/nphoton.2007.120.

Liu, S., Norman, J.C., Jung, D., Kennedy, M.J., Gossard, A.C. and Bowers, J.E. 2018. Monolithic 9 GHz passively mode locked quantum dot lasers directly grown on on-axis (001) Si. *Applied Physics Letters* 113(4). doi: 10.1063/1.5043200.

Rosales, R. et al. 2011. InAs/InP quantum-dot passively mode-locked lasers for 1.55-μm applications. *IEEE Journal on Selected Topics in Quantum Electronics* 17(5), pp. 1292–1301. doi: 10.1109/JSTQE.2011.2116772.

Li, Z. et al. 2020. Monolithic InP Quantum Dot Mode-Locked Lasers Emitting at 730 nm. *IEEE Photonics Technology Letters* 32(17), pp. 1073–1076. doi: 10.1109/LPT.2020.3012568.